

Adhesion Modulation in Bio-inspired Micropatterned Adhesives by Electrical Fields

Dissertation

zur Erlangung des Grades
des Doktors der Ingenieurwissenschaften
der Naturwissenschaftlich-Technischen Fakultät

der Universität des Saarlandes



**UNIVERSITÄT
DES
SAARLANDES**



von

Vaishali Chopra

Saarbrücken, 2020

Tag des Kolloquiums: 10. September 2020

Dekan: Prof. Dr. Gregor Jung

Berichterstatter: Prof. Dr. Eduard Arzt
Prof. Dr. Stefan Seelecke

Vorsitz: Prof. Dr. Tobias Kraus

Akad. Mitarbeiter: Dr. Frank Aubertin

Annex 1

Declaration of original authorship

I hereby declare that this dissertation is my own original work except where otherwise indicated. All data or concepts drawn directly or indirectly from other sources have been correctly acknowledged. This dissertation has not been submitted in its present or similar form to any other academic institution either in Germany or abroad for the award of any other degree.

Saarbrücken, 02.06.2020

Abstract

With steps towards Industry 4.0, it becomes imperative to the development of next-generation industrial assembly lines, to be able to modulate adhesion dynamically for handling complex and diverse substrates. The inspiration for the design and functionality of such adhesive pads comes from gecko's remarkable ability to traverse rough and smooth topographies with great ease and agility. The emphasis in this thesis was to equip artificial micropatterned adhesives with such functionalities of tunability and devise an on-demand release mechanism. The project evaluates the potential of electric fields in this direction. The first part of this work focusses on integrating electric fields with polymeric micropatterns and studying the synergistic effect of Van der Waals and electrostatic forces. An in-house electroadhesion set up was built to measure the pull-off forces with and without electric fields. As a function of the applied voltage, adhesion forces can be tuned. The second part of the work demonstrates a novel route that exploits the in-plane actuation of the dielectric elastomeric actuators integrated with microstructure to induce peeling in them. Voltage-dependent actuation has been harnessed to generate the requisite peel force to detach the micropatterns. Overall, the findings of this thesis combine disciplines of electroadhesion, electroactuation, and reversible dry adhesives to gain dynamic control over adhesion.

Kurzzusammenfassung

Im Einklang mit dem Fortschreiten in Richtung Industrie 4.0, wird es auch für die Entwicklung von industriellen Montagelinien der nächsten Generation unerlässlich sein, die Handhabung komplexer und unterschiedlicher Objekte zu flexibilisieren. Bioinspirierte Haftpads nach dem Vorbild des Gecko könnten zukünftig hierzu wesentlich beitragen. Der Schwerpunkt dieser Arbeit bestand darin, künstliche mikrostrukturierte Haftpads mit einem elektrisch schaltbaren Adhäsions- und Ablösemechanismus zu funktionalisieren, um die Grundlage für einen schnell schaltbaren, intelligenten Greifer zu schaffen. Der erste Teil dieser Arbeit konzentriert sich auf die Kombination elektrischer Felder mit elastomeren Mikrostrukturen und die Untersuchung der synergistischen Wirkung von Van der Waals- und elektrostatischen Kräften. Zur Messung der Adhäsion wurde ein individueller Aufbau realisiert und mit diesem die Feldstärkeabhängigkeit der Haftkräfte nachgewiesen. Der zweite Teil der Arbeit demonstriert einen neuartigen Ablösemechanismus unter Ausnutzung der lateralen Bewegung dielektrischer elastomerer Aktuatoren, um so ein Abschälen der Haftpads vom Substrat zu induzieren. Durch Variation der elektrischen Spannung wurde untersucht, wie sich diese auf die Ablösegeschwindigkeit der Haftpads auswirkt. Insgesamt kombinieren die Ergebnisse dieser Arbeit die Disziplinen Elektroadhäsion, Elektroaktuation und reversible trockene Klebstoffe, um so eine dynamische Kontrolle über die Adhäsion zu erhalten.

“I may not have gone where I intended to go, but I think I have ended up where I needed to be”

- Douglas Adams

Acknowledgement

As scientists, we develop frameworks to explain subjective experiences by dissecting evidence. We run control experiments to look at the evidence with novel perspectives and a quantitative approach. Social scientists follow a similar approach to retrace the ingredients of success. It's at the core of scientific endeavour to quantify things that are intuitive and subjective. As a researcher, I've to learn to look at things as they are and not what they seem. Similar to what a painter does, every time she picks a pencil and draws construction lines, I've to learn to keep my perspective stationary while allowing scope for a better vantage point to lay it as perfectly as I could on the canvas of Science. I've had to learn to persevere and redraw until I was convinced to stand by my work.

Quite early in my academic journey, I realized, success for me translated to success in Science. Apart from internal choices, the most dominant factor for scientific success is the presence of a supportive and collaborative Workplace. It's our soundboard to bounce theories, a culture to have debates, and a space for ideas to collide and mature. I feel fortunate to be at one such fountainhead for fresh ideas during my years at INM, Leibniz Institute for New Materials, Saarbrücken. This journey was filled with arduous peaks and valleys of self-discovery. As I hitchhiked this path with my backpack of hope, the unwavering support of strangers turned colleagues has humbled me beyond words.

I want to start by thanking Prof. Dr. Eduard Arzt for being my mentor and guardian in this journey. Your commitment to Science, passion for music, and wit and humour that lightens up the room is a constant reminder that when pursued with heart, every opportunity is full of learning. Thank you for your trust in me and for encouraging me by providing opportunities to perform at the highest level. Thank you for making the dissertation writing process mindful and rewarding. It is a privilege to be your student.

I extend my gratitude to Prof. Dr. Stefan Seelecke. As my academic supervisor, your guidance and support positively propelled the research into interesting directions. Thank you for introducing me to the field of mechatronics by the successful collaboration under your kind supervision.

Next, I want to thank Dr. René Hensel. Your guidance helped take the electroadhesion project to fruition. Your scientific expertise has been instrumental in the successful completion of projects on electroadhesion and dewetting. Thank you for the opportunity to run lab courses for undergraduate students, enabling me to improve my knowledge transfer skills.

I feel fortunate to also being supervised by Dr. Karsten Moh. You have always been generous with your time and patiently guided me at every stage. Your experience with both academia and industry translated into discussions and holistically shaped the understanding of the projects during my time here.

Thank you all for shaping me as a researcher. I hope to have your continued support in future.

Next, I would like to thank, Prof. Dr. Anton Darhuber, and his student Maciej Chudak for their active support in collaborating on two projects within the Biosmart ITN network which materialised as two joint manuscripts in preparation. Thank you for hosting me during my secondment at TU Eindhoven on the dewetting project using 2-photon lithographically patterned structures fabricated at INM. The numerical and theoretical part in Chapter 3 has been co-authored by them. It has been a pleasure to successfully collaborate with you.

At INM, I met several colleagues who extended help and support. I would like to thank members of the functional microstructure group. Thanks to Mr. Joachim Blau for his support with the construction of the adhesion setup. I enjoyed working alongside members from the group particularly Dr. Yue Wang, Manar Samri, Jennifer Dollman, Angela Rutz, Andreas Weyand and Dr. Gisela Heppel who stepped up to help and had good discussions. I had the pleasure of working with Bruno Schäfer, Dr. Peter König and Dr. Kira Fries on industrial projects and thankful for their cooperation and support. I thank Dr. Marcus Koch and Tabea Trampert who always happily extended their support with the ESEM characterisations. Members of the mechanical workshop particularly, Mr. Werner Schneider, Mr. Martin Schmidt supported with technical support for electrical and mechanical stuff. I would like to thank Mesut Aslan and Dr. Sener Albayrak and Dr. Samantha Hussman for their support while investigating the conductive inks.

I would also like to thank Ms. Sylvia de Graff and Ms. Loeb for their support with meeting the administrative requisites of the doctoral programme. The library staff Ms. Elke Bubel always helped with access to the literature. The support from the IT department and particularly from Mr. Ralf Muth ensured smooth writing of thesis. I had an enjoyable time with colleagues Dr. Essak Khan, Mr. Stefan Bruck, Dr. Malgorzata Beigun and Dr. Liz Prieto.

I would like to extend a special thanks to my Facebook family - colleagues and managers who encouraged me throughout my internship and provided me with innovative projects.

This thesis began as part of an Innovative Training Network (ITN) under the Marie Skłodowska- Curie Grant. I am thankful to the funding agency European Union Horizon 2020 programme. The platform offered the opportunity to train under a leading network of experts in the field of Adhesion. I would like to mention my friends many of whom are already doctors Maciej Chudak, Maria Villoui, Dr. Mehdi Vehdati, Dr. Francisco Cedano, Victor Kang, Ugo Sidoli, Dr. Justine Tavera, Dr. Aurelie Feat, Dimitris Mintis and Dr. Marco Dompe for such a wonderful time and a long lasting bond. It's been incredible to share our journeys together. A big thanks to the mentors and project coordinators for always encouraging me.

As this journey approaches the final lap, paving way for newer beginnings, I would like to thank my family – my parents and my brother Jai for being the common denominator for success throughout, for their love and support and for constantly reminding me of why I set out for this endeavour. Lastly, I would like to thank my best friend Ashish for being there and always celebrating small moments and making them count. As a Buddhist saying goes “When the student is ready, the teacher appears”. I thank all of you and others who encouraged the student in me and kept the dream alive.

List of Symbols

$w(\mathbf{r})$	Van der Waals interaction energy potential
Φ	Potential distribution
E	Electric potential
σ_{ij}	Maxwell stress tensor
δ_{ij}	Kronecker delta
ϵ_0	Permittivity of free space
Q	Electric charge
σ_{ad}	Electroadhesive stress
P	Effective pressure
Y	Young's modulus
μ_m	Mechanical efficiency of the actuator
G	Storage modulus
G''	Loss modulus
A_p	Projected area
ϵ_r	Relative permittivity of material
σ_0	Zero-field air conductivity

D_i	Electric displacement field
S_i	Mechanical force density
$2a$	Electrode width
F_{es}	Electroadhesive force
σ_n	Normal stress
σ_p	Peel stress
F_T	Applied tensile force
D_P	Deformation of the fibril
D_{DEA}	Deformation of the DEA membrane
D_{BL}	Deformation of the backing layer
Δl	Strain in the fibril

List of Abbreviations

ST	Setae
SP	Spatulae
DC	Direct current
DEA	Dielectric elastomeric actuator
PDMS	Polydimethylsiloxane
VdW	Van der Waals
LJ	Lennard Jones
ESC	Electrostatic chuck
PPC	Parallel plate configuration
IDE	Interdigitated electrodes
DEP	Mechanical efficiency of the actuator
MAV	Micro aerial vehicle
Cu-Pc	Copper (II) pthalocyanine
MDF	Medium density fibre board
DMTA	Dynamic mechanical thermal analysis
MBD	Molecular beam deposition
SNE	Soft nanocomposite electroadhesive

CNT	Carbon nanotubes
LED	Light emitting device
RH	Mechanical force density
JKR	Johnson-Kendall-Roberts
FEA	Finite element analysis

List of Publications

Published Chapter

Chapter 3

Chopra, Vaishali, Maciej Chudak, René Hensel, Anton A. Darhuber, and Eduard Arzt. "Enhancing dry adhesion of polymeric micropatterns by electric fields." *ACS Applied Materials & Interfaces* (2020).

The article is available under: <https://pubs.acs.org/doi/abs/10.1021/acsami.0c05077>

Enquiries about the permissions related to the content of the publications should be directed to ACS.

Section on theoretical models and numerical results has been co-authored by Prof. Darhuber and Maciej Chudak at TU Eindhoven.

Table of Contents

Annex 1.....	III
Abstract.....	IV
Kurzzusammenfassung.....	V
Acknowledgement.....	VII
List of Symbols.....	X
List of Abbreviations.....	XII
List of Publications.....	XV
Table of Contents.....	1
Chapter 1: Introduction.....	4
Chapter 2: Literature Review.....	7
2.1. Electrostatic Forces.....	8
2.1.1. Comparison with Van der Waals Forces.....	8
2.1.2. Electroadhesion: Historical Perspective.....	9
2.1.3. Electroadhesion: Maxwell Tensor.....	11
2.1.4. Electroadhesion in Dielectrics: Polarization.....	12
2.1.5. Electroadhesion in Conductors: Charge Separation.....	14
2.2. Engineering Electroadhesive Forces.....	16
2.2.1. Electrodes.....	18
2.2.2. Dielectric Layer.....	20
2.2.3. Roughness of the target Object.....	21
2.2.4. Environmental Parameters.....	22
2.2.5. Dielectric Constant.....	23
2.3. Early attempts to combine electroadhesion & micropatterned adhesives.....	27
2.4. Switchable Adhesion.....	29
2.5. Electroactuation.....	31
2.5.1. Dielectric Elastomeric Actuators.....	32
2.5.2. DEA Fundamentals.....	33
I. Conformal Electrodes.....	33
II. Dielectric Material.....	36
III. Mechanical Pre-stretch.....	38

2.5.3. Actuator Configurations.....	39
I. Stack Actuators.....	40
II. Membrane Actuators	41
2.6. DEA Applications: Pick and Place.....	42
2.7. Challenges: Electroadhesion and Electrostriction Devices.....	46
2.7.1. High operating Voltages.....	46
2.7.2. Residual Charges	48
2.8. Objective of the thesis	49
Chapter 3: Enhancing dry adhesion of polymeric micropatterns by electric fields*	50
3.1. Abstract.....	50
3.2. Introduction	51
3.3. Materials and Methods.....	52
3.3.1. Device Fabrication.....	52
3.3. Electroadhesion Setup	53
3.4. Experimental Methods.....	54
3.5. Theoretical Models.....	57
3.5.1. Electrostatic Interaction – Insulating Materials.....	57
3.5.2. Bulk-Conductive Materials	58
3.5.3. Surface-conductivity of Glass-Air Interfaces.....	59
3.5.4. Variable Air Conductivity.....	59
3.5.5. Electroadhesion force	60
3.5.6. Computational domain, boundary conditions and material properties	61
3.6. Numerical results	64
3.7. Discussion	68
3.8. Conclusions	69
3.8. Supporting Information	69
Chapter 4: Shear induced Peeling of Polymeric Micropillars using Dielectric Elastomeric Actuators.....	70
4.1. Abstract.....	70
4.2. Introduction	70
4.3. Materials and Methods.....	71
4.4. Dielectric Elastomeric Actuator	72

4.5. Experimental Setup	74
4.6. Adhesion Measurements	76
4.7. Results and Discussions	78
4.7.1. Effect of varying hold time.....	78
4.7.2. Effect of varying bias on crack growth	81
4.7.3. Time Dependence of Crack Growth	82
4.7.4. Detachment under tensile loads.....	86
4.7.5. Micropatterned Arrays.....	89
4.8. Conclusion.....	90
Chapter 5: Summary and Outlook.....	92
5.1. Summary.....	92
5.2. Outlook.....	93
Appendix	95
A. Additional Information: Chapter 3	95
I. Dependence of the electroadhesion force on the a/b ratio.....	95
II. Model validation for flat surfaces	95
III. Validation of the effective medium approximation	97
IV. Comparison between idealized and realistic geometries of the electrode array	98
V. Scaling of Maxwell traction for purely dielectric materials	100
B. Additional Information: Chapter 4	100
I. Deformation of the Pillar	104
II. Deformation of the DEA-membrane.....	104
III. Deformation of the Backing Layer.....	107
IV. Peel Angle Under Tensile Loads.....	108
List of Figures	112
References.....	120
Curriculum Vitae	140

Chapter 1: Introduction

Nature's toolkit continues to inspire mankind and offer sustainable solutions for different applications. For centuries [1], the remarkable load bearing capacity of geckoes, while treading different surfaces with agility, intrigued human curiosity [2]. A closer microscopic look at the toe pads of the *Gecko gecko* revealed intricate hierarchical architecture as shown in Figure 1. Each toe pad consists of thousands of setae with each individual seta having a length of (ST) 30- 130 μm , branched into sub- μm spatulae (SP). A gecko makes intimate contact through a myriad of these structures [3].

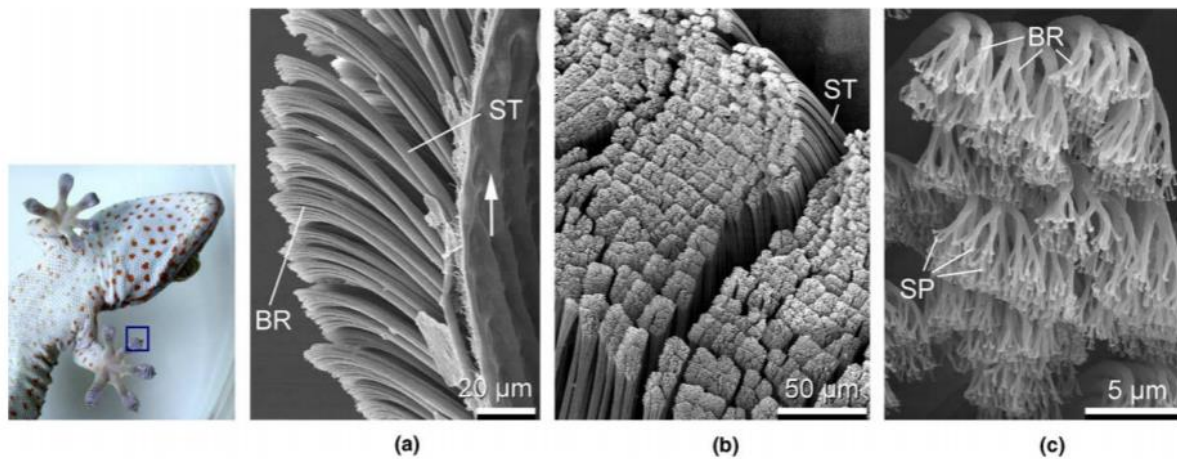


Figure 1 Scanning electron micrographs of the toe pads of *Gecko gecko* (a) (b) Toe pads consist of hundreds of setae (ST represents a single seta) (c) Each seta is branched further in to sub micrometre spatula (SP). BR denotes the branches. Reproduced from [2]

While adhesion strength motivates the abstraction of these design principles into artificial adhesives [4] [5], the aspect of reversibility is uniquely distinguishing. To emulate the ability of geckoes to optimise and regulate adhesion depending on the counter surfaces, coupled with the ease to detach and make new contacts, has been the long-term goal of the scientific community [6].

The present thesis evaluates the potential of electric fields to modulate the adhesion of micropatterned adhesives. There are several advantages offered by electrical fields that establish its uniqueness when compared to other external triggers such as magnetic fields,

thermal stimuli and compressive mechanical forces (preload). One of the major advantages stems from the fact that every material is inherently responsive to electric field. In the presence of an applied field, dielectrics undergo polarisation. It is different in case of conductors, where free charges get separated in presence of an electric field. At the atomic level, distortion of electron clouds with respect to nuclei (electronic polarization) and, at the molecular level, asymmetric charge distributions (orientation polarization) occur [7]. Additionally, in heterogeneous materials charge accumulates at structural interfaces. Thus, a macroscopic field distortion results from an applied electric field in this case leading to interfacial or space charge polarisation. These interfacial polarizations are held responsible for electroadhesive forces [8] [9]. Depending on the degree of polarizability, there is a strong or a weak response. This intrinsic property opens a multitude of options for the counter surfaces such as conductors and insulators that can be manipulated using an electroadhesive.

On the other hand, application of magnetically switchable adhesives is restricted to class of materials that selectively respond to magnetic fields [10]. The same holds true for thermal or photo regulatable mechanisms wherein there is a need to engineer a unit that undergoes change in response to these stimuli and ultimately lead to change in adhesive forces [11]

Furthermore, within this framework of external triggers most of the stimuli influence adhesion in a binary way by switching between the adhesive and non-adhesive states, rather than dynamically regulating it, as is the case with a live gecko. Varying the electrical fields offers controllability on the magnitude of adhesive forces which can be regulated as per the need. The practical implications are that a single end-effector robot could be employed, and the same assembly line could be used for automated handling of different devices by controlling the electric fields. Electroadhesion has been studied in the first part of this thesis for dynamic regulation of the measured pull-off strengths in dry adhesives by superimposing DC electric fields.

Similarly, a dielectric material undergoes mechanical deformation in presence of an applied electric field. When the strain is unchanged on reversing the sign of the electric field i.e. the effect is quadratic, this electro-mechanical coupling is referred to as electrostriction and is exhibited predominantly in case of piezo and ferroelectric crystals. [12] [13]. In the second part of the thesis, electroactuation due to Maxwell stress is employed using dielectric elastomeric

actuators (DEA) for facilitating release of dry adhesives from counter surfaces by initiating shear detachment.

Although electroadhesion, electroactuation and Van der Waals adhesion in micropatterned adhesives are stand-alone mature technologies, their combination is relatively new. This thesis is an attempt to closely understand the interactions as a result of superimposing long range electrostatic forces on short range Van der Waals forces. On one hand, the thesis helps to fundamentally understand the afore-mentioned superposition by analysing the force displacement and force time measurements in a custom made electroadhesion measurement setup and on the other, demonstrates that electrical forces can be engineered to enable attachment (via electroadhesion) and detachment (via DEA) of patterned adhesives.

This research domain is incessant with interesting applications ranging from pick and place systems to self-cleaning adhesives [14]. All the microstructures discussed within the scope of this thesis were fabricated using polydimethylsiloxane (PDMS) with glass as the target object for measuring adhesion.

The thesis is organised into 5 sections. Chapter 2 titled Literature review provides a detailed discussion on the mechanism of electroadhesion and electroactuation processes and their emerging cognizance for designing smart adhesives in combination with bioinspired adhesives. With this understanding, Chapter 3 experimentally demonstrates superposition of electric fields on dry micropatterned adhesives for achieving dynamic tunability of adhesion strengths by designing a custom electroadhesion setup. In collaboration with Prof. Anton Darhuber and his student Maciej Chudak from TU Eindhoven (Netherlands), a theoretical model and its numerical implementation was developed using Comsol 5.2. The theoretical part of the chapter has been co-authored by TU Eindhoven. The experimental work focussed on DEA induced shear detachment is presented in Chapter 4. The dielectric actuator used in the study was provided by Prof. Stefan Seelecke from ZeMa (Zentrum für Mechatronik und Automatisierungstechnik gemeinnützige GmbH), Saarland. The thesis concludes with the Chapter 5 titled Discussions cumulatively summarising the key findings from this work and an outlook on further developments.

Chapter 2: Literature Review

Nature has equipped each organism with capabilities optimised in accordance to their respective habitats. From an opposable thumb in humans giving them the prehensile grip [15], to the anatomy of the fin bones [16][17] in fish that help them locomote, there is a rich reservoir of detail and precision in the naturally occurring designs [18][19]. Similarly, one of the fascinating features that captured interest of the scientific community, was the ability of geckos to stick and unstick to almost all surfaces with equal ease.

Van der Waals (VdW) forces were confirmed as the dominant source of this adhesion thereby discounting the contribution from suction forces. [20][21]. Soon after, capillary forces were also established to play a role in gecko adhesion [22]. It is remarkable that not only does the gecko exhibit strong adhesion but is also able to modulate it as needed. While biologists continued investigating the detachment mechanism in geckos [23][24], mimicking these strategies has been instrumental in guiding the development of smart adhesives [25][26] and robotic systems [27][28][29]. Furthermore, replication of these blueprints as artificial adhesives has pushed the need for tuning the mechanical architecture and materials for adaptability across diverse target surfaces. Adhesion in micropatterned adhesives is controlled by the contact shape [30][31] and modifying the tip geometries offers a route for regulating adhesion on rough surfaces [31][32]. In addition to the shape of contacts, these reversible adhesives are also sensitive to misalignment [33][34] and surface contamination[35]. Thus, with a tolerance to complexity of target substrates (based on shape and texture), degree of misalignment and performance in contaminated environments, researchers must constantly tailor dry reversible adhesives to meet these challenges.

On all the above-mentioned yardsticks, adhesion modulation (tuning and switching) via superimposed electrical fields has hardly been researched and this thesis taps into this unexplored domain. This chapter is organised in following sections. Section 2.1 discusses the electrical forces and the behaviour of materials in a uniform and non-uniform electric field. It elaborates on the historical perspective when electrical fields were initially explored for handling materials. This is followed by section 2.2 which provides an insight into engineering

electroadhesive forces and concludes by discussing applications where dry adhesives have been integrated with electroadhesion. Section 2.3 summarises the early attempts in this direction of integrating dry adhesives with electric fields. Section 2.4 discusses the need for switchable adhesion followed by Section 2.5 which focusses on the mechanism of electroactuation and its application on leveraging actuation in dielectric elastomeric actuators (DEA) for enabling easy detachment of objects. Key parameters governing the performance of DEAs have been presented. The final section concludes with a discussion on the challenges limiting the application of electroadhesion and electrostriction technologies.

2.1. Electrostatic Forces

With the development of quantum theory in the 1920s, it was understood that all intermolecular forces are inherently electrostatic in nature [36] (Hellman- Feynman theorem). Electrostatic forces include the interactions between charges, ions, permanent dipoles and polarization interactions as a result of induced dipoles in molecules in the vicinity of an electric field.

Charles Augustin Coulomb's two memoirs, presented to the Paris Academie Royale des Sciences in 1785, formed the basis of the Coulomb's law [37]. The law states that the force between two fixed point charges is directly proportional to the product of the charges and inversely proportional to the square of the distance between them.

$$F = \frac{kq_1q_2}{r^2}$$

2. 1

where q_1 , q_2 are point charges, k is the Coulomb constant and r is the distance of separation between the charges.

2.1.1. Comparison with Van der Waals Forces

Van der Waals forces on the other hand are short range (< 1 nm) intermolecular interactions. Lennard jones potential (LJ) is a pair potential that models van der Waals bonds between noble gases. The negative term in the Lennard Jones potential [38] represents the Van Der Waals interaction and is given by:

$$w(r) = -\frac{A}{r^6} + \frac{B}{r^{12}}$$

2. 2

where $w(r)$ is the van der Waals interaction energy function and A and B are constants defined as $A = 4\epsilon\sigma^6$ and $B = 4\epsilon\sigma^{12}$. ϵ denotes the bond energy of the molecule and σ denotes the bond length. r is the separation between two atoms Figure 2 represents the Lennard Jones potential.

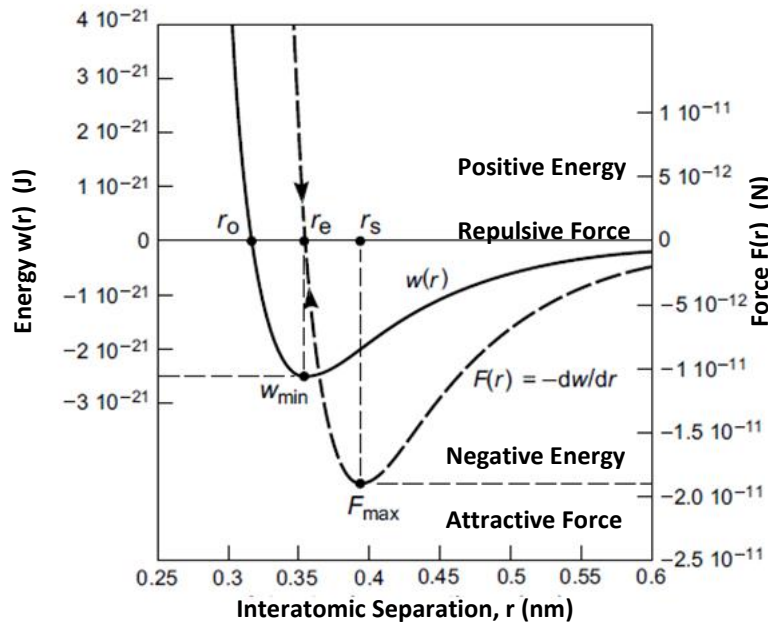


Figure 2 Graph – Lennard Jones potential with interaction potentials $A = 10^{-77} \text{ J m}^6$ and $B = 10^{-134} \text{ J m}^{12}$. r_e is the equilibrium separation, where the force is zero and the energy is minimum. r_s is the point at which the two atoms separate spontaneously when pulled apart by the pull-off force, F_{max} . Reproduced from [36].

2.1.2. Electroadhesion: Historical Perspective

The earliest application when electrical forces were realised with the potential to adhere to different materials can be traced back to 1923, when Alfred Johnsen and Knud Rahbek applied a voltage of 440 V across a metal disc and observed that it could cling to a lithographically

polished stone [39]. They observed that a considerable shear and normal force existed between the two bodies. This property was later utilised in the semiconductor industry for designing electrostatic chucks for handling Si wafers in the early 1970s [40].

For patterning the wafers, it is critical to align them to their reticles prior to exposure. When the exposure was carried out optically, wafers were handled by vacuum chucking. However, with the developments in electron-beam lithography, which is carried out in vacuum conditions, this method of handling wafers soon became invalid. Thus, electrostatic chucking was introduced, wherein the back of the semiconductor wafer acted as one of the electrodes and the other electrode was used in a capacitor configuration separated by an insulating layer. Figure 3 shows a non-flat wafer adhering to an electrostatic chuck. The semiconductor wafer is grounded and acts as one of the electrodes in this capacitor configuration.

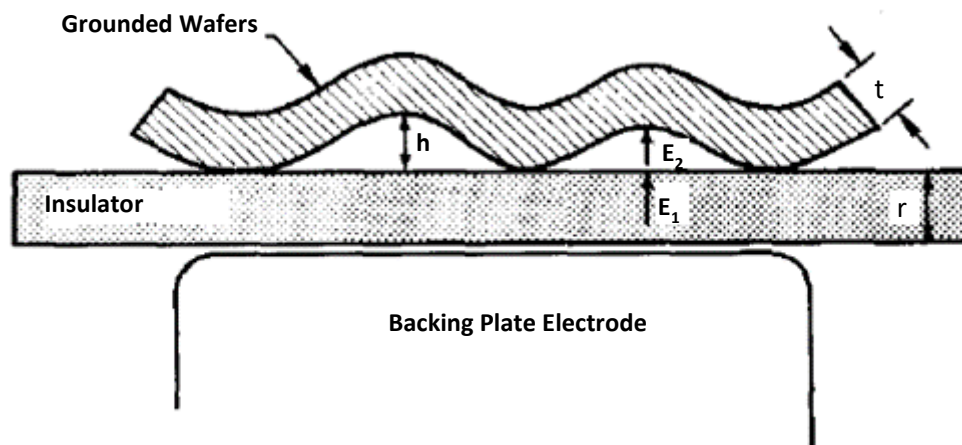


Figure 3 Parallel plate capacitor clamp configuration- Schematic representing an electrostatic chuck with the insulating layer of thickness r separating the backing electrode and the imperfectly flat wafer with a height h as a function of position. E_1 and E_2 represent the Electric fields in the insulator and wafer, respectively. This is a coulombic capacitive clamp. Reproduced from [40].

This configuration of the electrostatic chucks (ESC) was regarded as the parallel plate configuration (PPC) [41], also referred to as the coulombic capacitive clamp. One of the advantages of this configuration is fast clamping and declamping because the charges reside on the electrode surfaces. However, the presence of a leakage current is a disadvantage here [42].

Yet another arrangement studied was the interdigitated electrodes (IDE) embedded inside a dielectric as shown in Figure 4 [42]. This is known as the Johnson Rahbek capacitive clamp. The charges here are diffused across the dielectric. Since there is no direct contact with the target material, it simplifies the handling process.

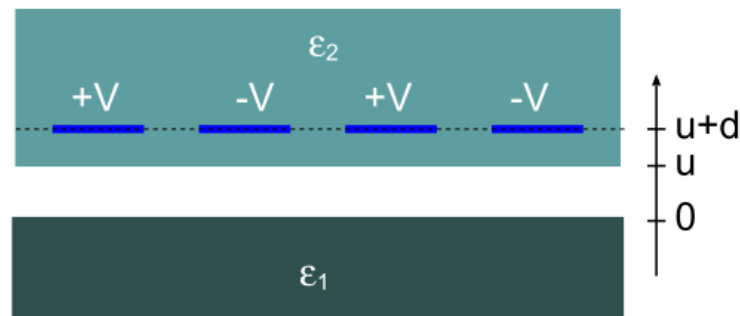


Figure 4 Johnson Rahbek capacitive clamp configuration- Cross sectional view of the electroadhesion setup. Electrodes (blue) are embedded in a dielectric layer with thickness d and dielectric constant ϵ_1 . The target material has a dielectric constant ϵ_2 . A uniform air gap of width u separates the pad from the target. Reproduced from [43].

The electrostatic chucks were initially limited to handling of flat and polished surfaces [40][42][44]. Adapting the technology to cater to handling of objects with complex curved shapes and textures (varying in roughness) necessitates a soft adhesive pad with the electrodes. This increased need to handle complex objects requires the compliance to handle objects as a human hand does. Since the IDE configuration does not involve direct contact with the target substrate, it has been increasingly studied for applications in designing electroadhesive pads [45][46].

2.1.3. Electroadhesion: Maxwell Tensor

Studies by Persson et. al. [43][47], Cao et. al. [48] and Guo et. al.[49], have been directed to calculate the electroadhesive force acting in such a configuration. The first step is to calculate the potential distribution (ϕ) between and around the electrodes embedded in the dielectric. This is obtained by solving the Laplace equation given by:

$$\nabla^2 \phi = 0$$

The electric field can then be calculated from the potential (ϕ) gradient, as:

$$E = -\nabla\phi$$

2. 4

Once the electric field has been obtained, the integration of the Maxwell stress tensor over the enclosed surfaces of the dielectric medium gives the net electroadhesive force. The Maxwell tensor for the specified electric field E can be described in component form as given in [50]

$$\sigma_{ij} = \epsilon_0 \left(E_i E_j - \frac{1}{2} E^2 \delta_{ij} \right)$$

2. 5

where σ_{ij} is the Maxwell stress, E_i and E_j are the electric field components along the x and y directions in the region enclosed by the dielectric, $\epsilon_0 = 8.85 \times 10^{-12}$ F/m is the permittivity of free space, and δ_{ij} is the Kronecker delta.

2.1.4. Electroadhesion in Dielectrics: Polarization

The Maxwell stress tensor method described above allows us to compute the electroadhesive forces. These forces arise from the fringe fields between the charges in the dielectric and the induced charges in the target object (when it is a dielectric).

A dielectric undergoes polarisation in the presence of an external electric field. The total polarizability can be divided into four categories, (i) electronic polarisation, (ii) ionic polarisation, (iii) dipolar polarisation and (iv) interfacial or space charge polarisation. Figure 5 shows the electric field time-period (1/frequency) dependence of different types of polarizations. At optical frequencies ($\sim 10^{15}$ Hz), the dielectric constant arises solely from the electronic polarisation.

Electronic polarisation arises from the displacement of the electron clouds relative to a nucleus. The ionic or atomic contribution comes from the displacement of a charged ion with respect to

other ions. The dipolar polarizability arises from molecules with a permanent electric dipole moment that can change orientation towards the direction of the applied electric field. These three types of polarisation effects are caused by the displacement or orientation of bound charge carriers. The fourth type called the interfacial or space charge polarisation occurs due to surface charges at the interfaces of the dielectrics, at frequencies below 10 Hz. In order to conclusively calculate the forces, one needs a comprehensive knowledge about the distribution of these polarizabilities. These interfacial polarisations are responsible for electroadhesion [49][8].

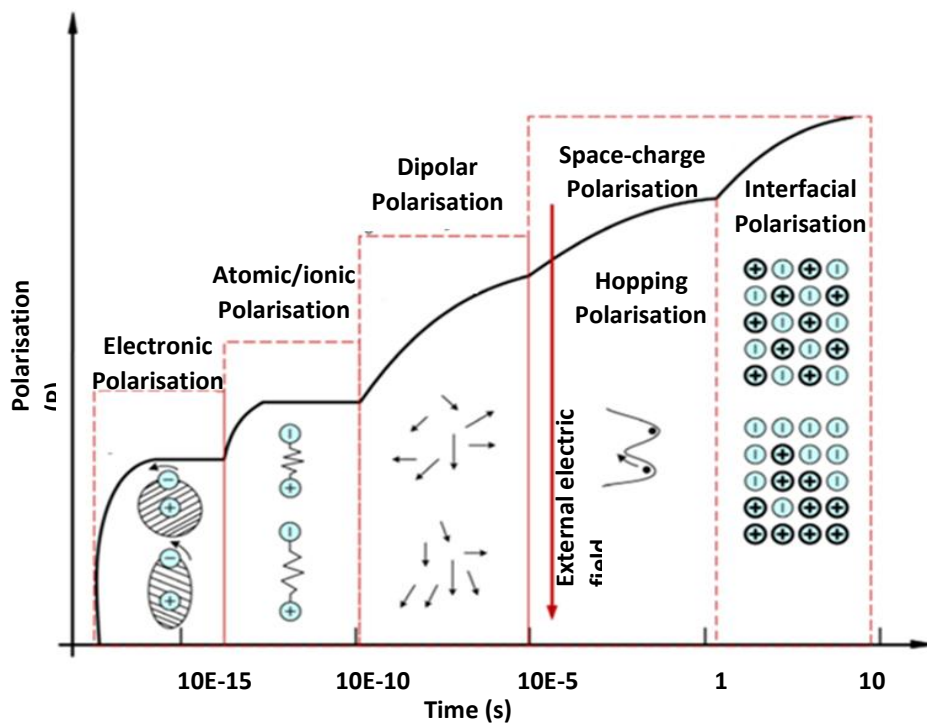


Figure 5 Polarisation types in a linear dielectric material under a time-varying electric field Reproduced from [49]

Polarisation of dielectrics has also been used for particle separation and fractionation. The process termed as dielectrophoresis (DEP) refers to the force exerted on the induced dipole moment of an uncharged dielectric and/or conductive particle in an inhomogeneous electric field. The term was coined by H. A. Pohl (1951) [51], who performed early experiments with small plastic particles suspended in insulating dielectric liquids and found that the particles would move in response to the application of a nonuniform AC or DC electric field.

The DEP force is represented as [52]

$$F_e = 2\pi r_p^3 \epsilon_m \epsilon_o \left(\frac{\epsilon_p - \epsilon_m}{\epsilon_p + 2\epsilon_m} \right) \nabla (E_e)^2$$

2. 6

where ϵ_m and ϵ_p are absolute dielectric constants of the medium and the particle, respectively. ϵ_o is the permittivity of the space, E_e is the electric field strength and r_p is the radius of the particle. As shown in Figure 6, when the dielectric constant of the particle is larger than that of the medium, the particle moves towards the pin electrode of greatest electric field strength. When the dielectric constant of particle is smaller than that of medium, the particle moves in the opposite direction. This forms the basis of particle separation and fractionation [53].

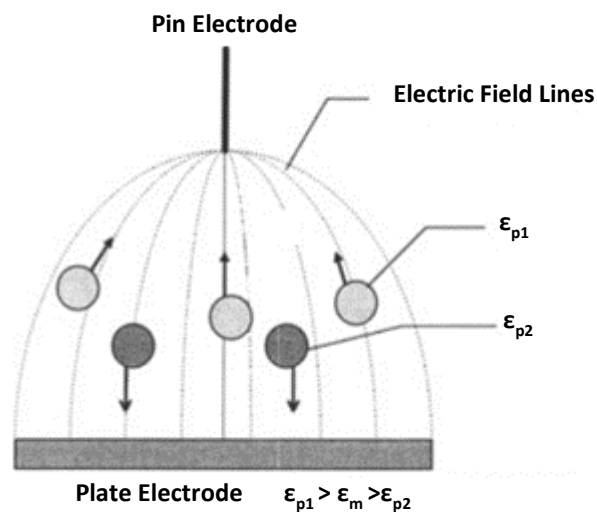


Figure 6 Principle of Dielectrophoresis -Dielectric particles experience different forces in a non-uniform electric field due to different dielectric constants. Dielectrophoresis is the process used for particle separation. Reproduced from [54].

2.1.5. Electroadhesion in Conductors: Charge Separation

For conductive substrates, when subjected to an external electric field, due to presence of free charge carriers, the charges separate. Yatsuzuka et al while studying the electrostatic chucks for handling Si wafers, calculated the electroadhesive force in an IDE setup [44] (Figure 7). The dielectric layer of thickness d was smaller than the electrode spacing g and a potential of

$\frac{V_a}{2}$ was applied between the object and the IDE. As the conductivity of the Si wafer was higher than of the dielectric material, it was assumed as a conductor for calculating forces on a conductor [44].

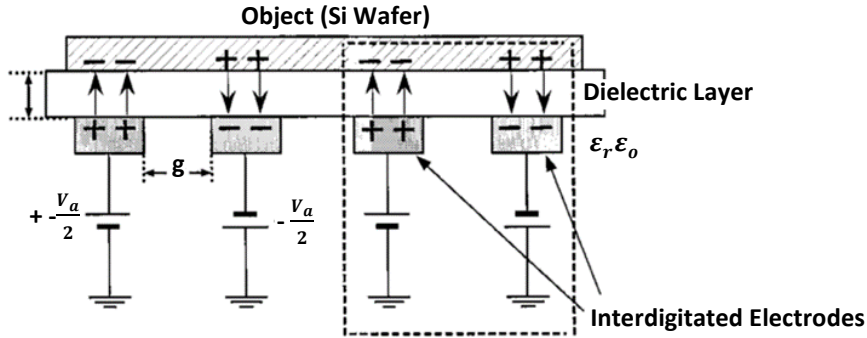


Figure 7 Schematic representing electroadhesion mechanism in an electrostatic chuck. Reproduced from [44].

The attractive force was calculated as

$$F_a = -\frac{\epsilon_r \epsilon_0 S_w}{4} \left(\frac{V_a}{2d} \right)^2$$

2.7

where $\frac{V_a}{2}$ is the potential difference between the two surfaces, S_w is the pad area, d is the dielectric thickness, ϵ_0 is the permittivity of free space and ϵ_r is the permittivity of the dielectric layer. Thus, that the attractive force is proportional to the square power of the applied voltage and inversely proportional to the square of the thickness of the dielectric layer.

This expression is derived by calculating the electric field produced between the 2 plates of the capacitor with area A and distance d between them

When a potential V is applied across the capacitor, each of the plates have a charge of $\pm Q$. The total electric field between the plates would be

$$E_{net} = \frac{Q}{A\epsilon_0}$$

2. 8

and

The potential can be expressed as

$$V = E_{net}d = d \frac{Q}{A\epsilon_0}$$

2. 9

The charge Q can be now be rewritten as

$$Q = \frac{AV\epsilon_0}{d}$$

2. 10

The plates are oppositely charged and therefore, the attractive force between them is equal to electric field produced by one of the plates times the charge on the other:

$$F_{att} = Q \frac{Q}{2A\epsilon_0} = \frac{\epsilon_0 AV^2}{2d^2}$$

2. 11

2.2. Engineering Electroadhesive Forces

Electroadhesion as a technology offers opportunities to be integrated with different soft robots. Some of the early applications where electroadhesive forces were maximised and optimised are the robot bee aerial vehicle designed by Graule, M. A., et al. [27] and the wall climbing electroadhesive robot by Prahlad, Harsha, et al. [55]. Figure 8a depicts the trajectory of the micro aerial vehicle. Electroadhesion was used as a mechanism to adhere the device to a target substrate. With the designed algorithm, the device flies closer to the target substrate. The polyurethane foam mount helps it align and stabilise near the target.

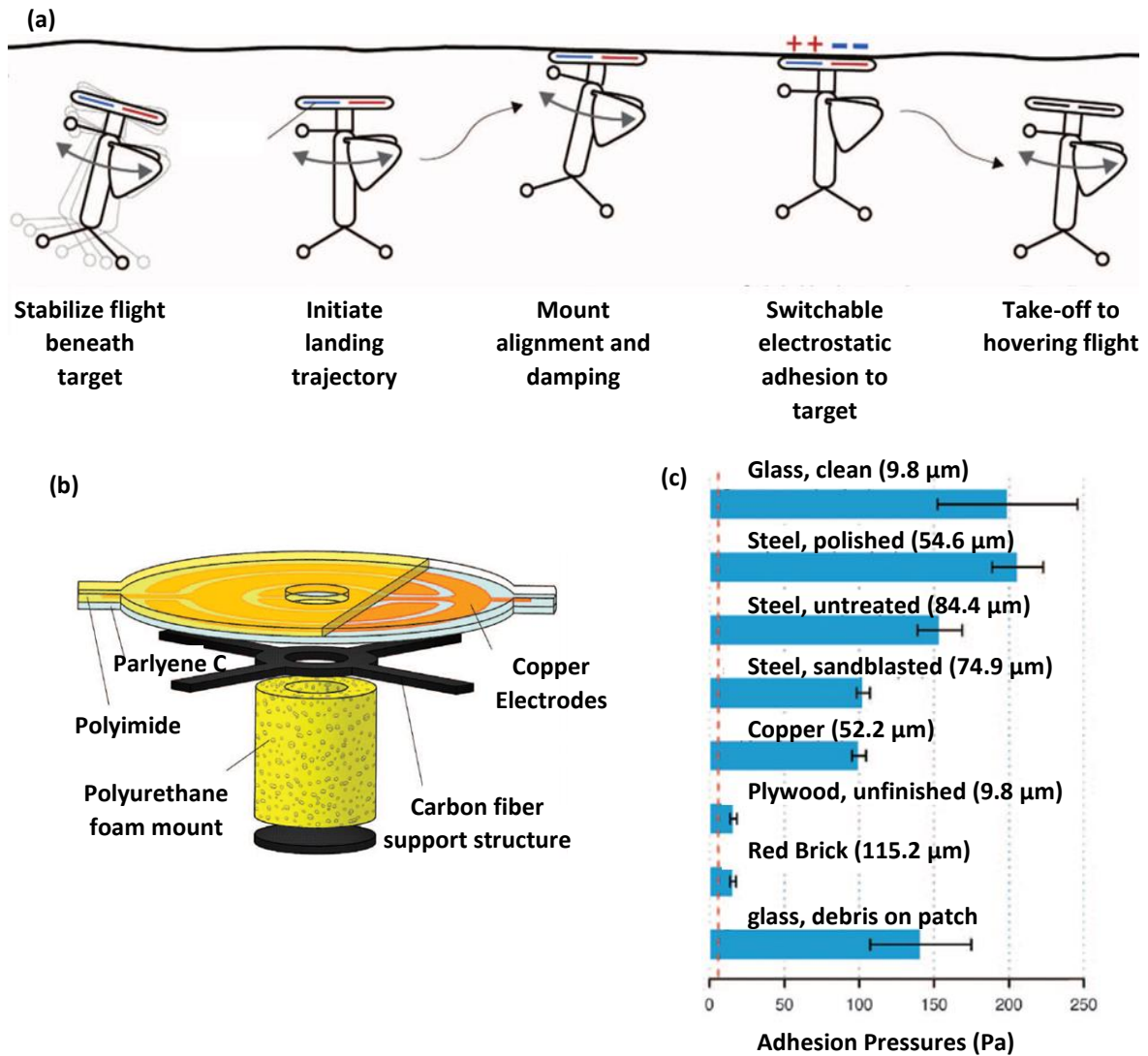


Figure 8 Micro aerial vehicle (MAV) design and operation (a) Schematic depicting the trajectory of the micro-aerial vehicle engaging with the target surface by means of electroadhesion (b) The aerial device consists of compliant copper electrodes coated on a polyimide film and covered by Parylene C. The entire structure is supported by a carbon fibre attached to a polyurethane foam mount that acts a damper in case of high velocity collisions and stabilises the device (c) An electroadhesive patch was designed using interdigitated electrodes and normal adhesion pressures were measured across different substrates with absolute values of surface asperities mentioned in the parenthesis. Reproduced from [27].

At this point, applying the potential between the electrodes results in setting up of surface charges between the device and the target material. The electroadhesive forces are set and they enable the device to stay attached to the target while suspended in air. As the applied potential are switched off, the residual charges remain and vary depending on the target material. The

weight of the device is also leveraged while programming the control logic and is used to facilitate the disengagement of the device.

The adhesive design consisted of 200 nm thick IDE Cu electrodes that were sputter-coated on a polyimide film. Finally, the electrodes were covered by a Parylene C film ($\sim 10 \mu\text{m}$) thickness using chemical vapor deposition. Figure 8c reports the normal adhesion pressures that were measured on different substrates using the similar electroadhesive pad at 1000 V [27]. The measurements were performed without cleaning the surfaces in between subsequent measurements. The variance in the measurements has been attributed to changes in humidity, surface contamination with air borne dust particles and alignment. Similar clamping pressures were also reported in wall climbing robots [55]. From the perspective of maximising the electroadhesive forces, there are four major categories of an electroadhesive system: electrodes, dielectric material, target roughness and environmental parameters.

2.2.1. Electrodes

Electrode geometry and thickness has been widely studied by different groups [49][41][56]. Cao et al modelled [48] the dependence of the electroadhesive force based on the Maxwell stress tensor method. Figure 9a shows a periodic section of a four-layer (I, II, III and IV) model consisting of interdigitated electrodes embedded in a dielectric medium and separated by an air gap from the target substrate labelled as the wall. The electroadhesive stress σ_{ad} as a function of a dimensionless parameter ‘C’ and geometrical and material properties for such a system is given as:

$$\sigma_{ad} = \frac{1}{2} \varepsilon_o \left[\left(\frac{\varepsilon_w}{\varepsilon_o} \right)^2 - 1 \right] C \left(\frac{a}{b}, \frac{h_1}{b}, \frac{t}{b}, \frac{\varepsilon_c}{\varepsilon_w} \right) \left(\frac{\Phi}{2b} \right)^2 \quad 2.12$$

where $L = 2b$ is the pitch (centre to centre distance between two adjacent electrodes) and $2a$ is the electrode width, ε_o denotes the dielectric permittivity of free space, ε_w is the permittivity of the wall (target substrate) and ε_c is the dielectric permittivity of the cover (dielectric layer). h_1 is the thickness of the dielectric layer and $h_2 - h$ marks the gap between the electroadhesive pad and the target material. The parameter C is a function of the geometrical parameters, a/b is the electrode width/pitch ratio, h_1/b is the normalised dielectric layer thickness and t/b is the

normalised air gap thickness. (ϵ_c/ϵ_w) represents the material parameters, Φ is the applied electric potential. Figure 9b shows that with increasing a/b ratio the electroadhesive force increases as a function of ratio of dielectric constants of the dielectric layer to that of the target substrate.

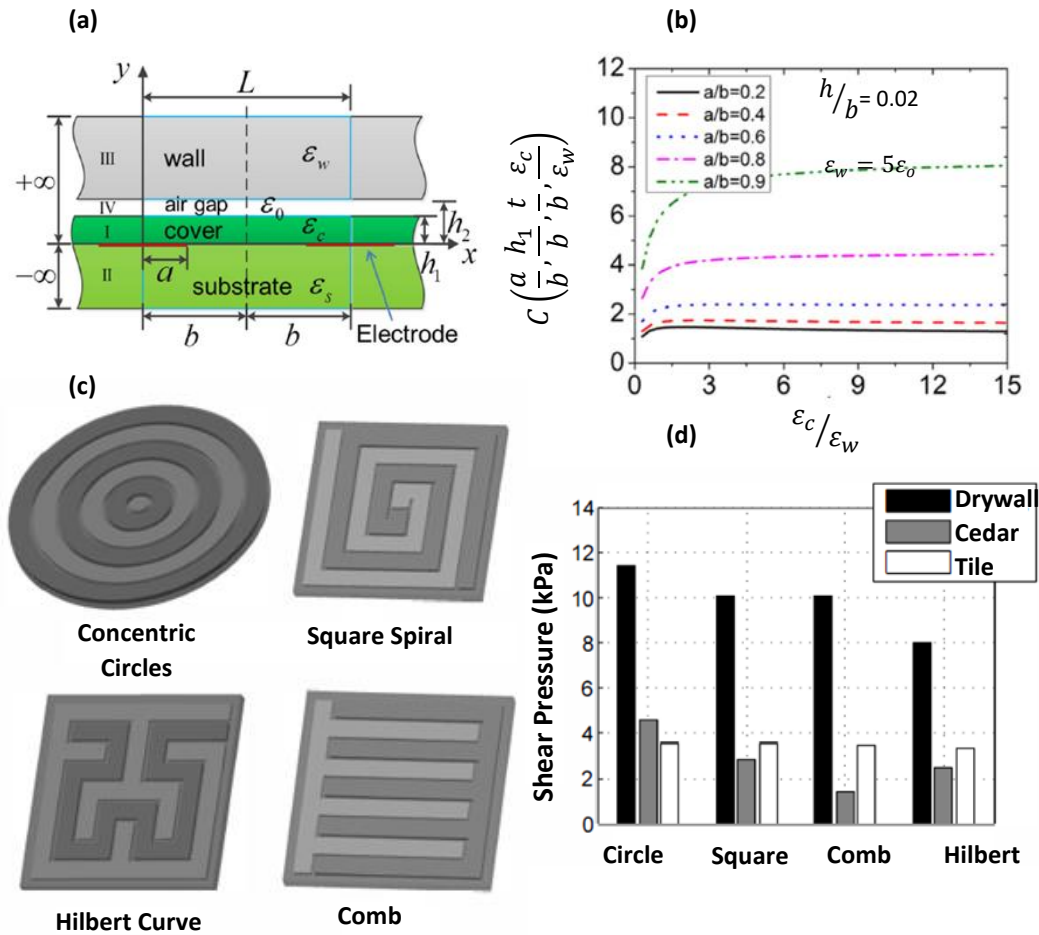


Figure 9 Theoretical and experimental results discussing the effect of electrode geometry on electroadhesion- (a) Four layer model of the electroadhesive pad consisting of interdigitated electrodes embedded in a dielectric layer [48] (b) Variation of parameter C for different normalised electrode width a/b when $h_1/b = 0.02$ and $\epsilon_w = 5\epsilon_0$ (c) Simulation models of different electrode patterns [57] (d) Experimental results showing shear pressures measured for different electrode patterns on drywall, cedar and tile substrates [57].

Electrode spacing was also varied and studied experimentally by Guo et al. [49] on glass and aluminium surfaces. For smaller electrode spacing, higher forces are measured as shown in Figure 10.

Furthermore, electrode geometries such as circular, Hilbert, spiral and comb shape were experimentally and theoretically studied to find the optimised values for achieving higher electroadhesive forces [57]. The circular pattern performed better than the others when adhesion was measured across different substrates as shown in Figure 8d. These studies highlight the influence of electrode spacing and electrode geometry on electroadhesive forces. For maximising the electroadhesive forces, these adhesives must conform to the target objects and ideally there should be no air gap between them. For making compliant adhesive pads, electrodes must also be capable of adapting to the topography of the target. In this respect, the thickness of electrodes is also critical in obtaining better adaptability without effecting the stiffness of the actuator [27][58].

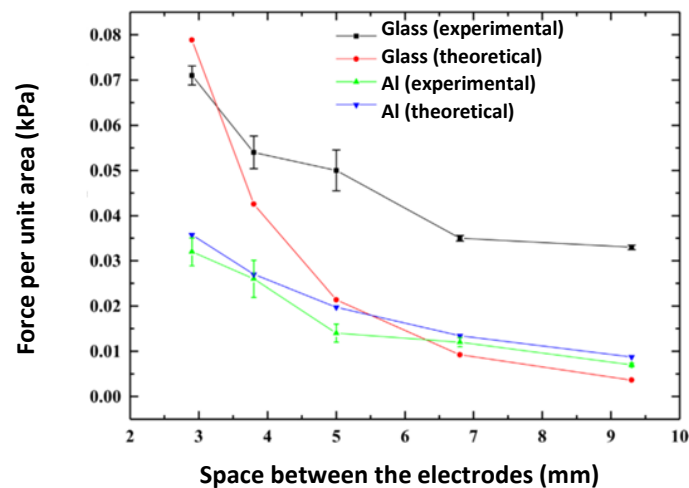


Figure 10 Experimental validation of the relationship between the electroadhesive forces obtainable and spaces between the electrodes and its comparison with the theoretical results. Reproduced from [49].

2.2.2. Dielectric Layer

The electroadhesive force is inversely proportional to the square of the dielectric thickness (equation 2. 7). Hence, efforts are directed to manufacture thinner dielectric membranes. On application of the electric fields, the polarisation of the dielectric induces charge distribution

in the target substrate. The fringe fields which form between the target substrate and the electroadhesive pad are a measure of the strength of electroadhesion [46][59]. With thinner dielectric layers, fringe fields will be stronger leading to higher adhesion. This in turn will limit the operating voltages to lower values. Methods such as CVD [27], Langmuir-Blodgett films [28] have been investigated to fabricate thinner dielectric layers.

The dielectric constant is the relative permittivity of the dielectric material and depends on the degree of polarizability of the material: the higher the dielectric constant, the higher is the degree of polarizability of material in the presence of an electric field. According to equation 2.7, the dielectric constant of the material is also crucial. Different fillers such as BaTiO₃, TiO₂ are doped in elastomeric matrices to achieve high dielectric materials. Filler concentration and size are critical for achieving high dielectric constants without trading off adhesion [60][45].

2.2.3. Roughness of the target Object

Real surfaces are not flat. Hence it is critical to address target substrates with varying levels of roughness. Ideally a zero-air gap is desired between the target and the adhesive pads to achieve higher forces [61][48][43]. Spenko et al [61] combined directional adhesives (silicone microwedges) with an electroadhesive pad and measured shear forces on different tiles with roughness varying from 10 to 100 μm . Figure 11a shows a hybrid micropatterned electroadhesive device with circularly patterned electrodes with microwedges (base width 20 μm and height 80 μm) [62]. Figure 11b shows the shear stresses in? of the hybrid pad in comparison to the microwedges, unpatterned dry adhesive (PDMS) and the electroadhesive pad without any microstructures. The hybrid device had better adhesion at roughness higher than 50 μm . This was because the directional adhesives conformed better to the roughness and this brought the electroadhesive closer to the surface, in turn engaging more of the microwedges. Therefore, a positive feedback loop is attributed to the better performance of hybrid device. The term shear pressure has been used by the authors [60] [61] . Shear pressure is a misnomer, they are simply measuring shear stresses.

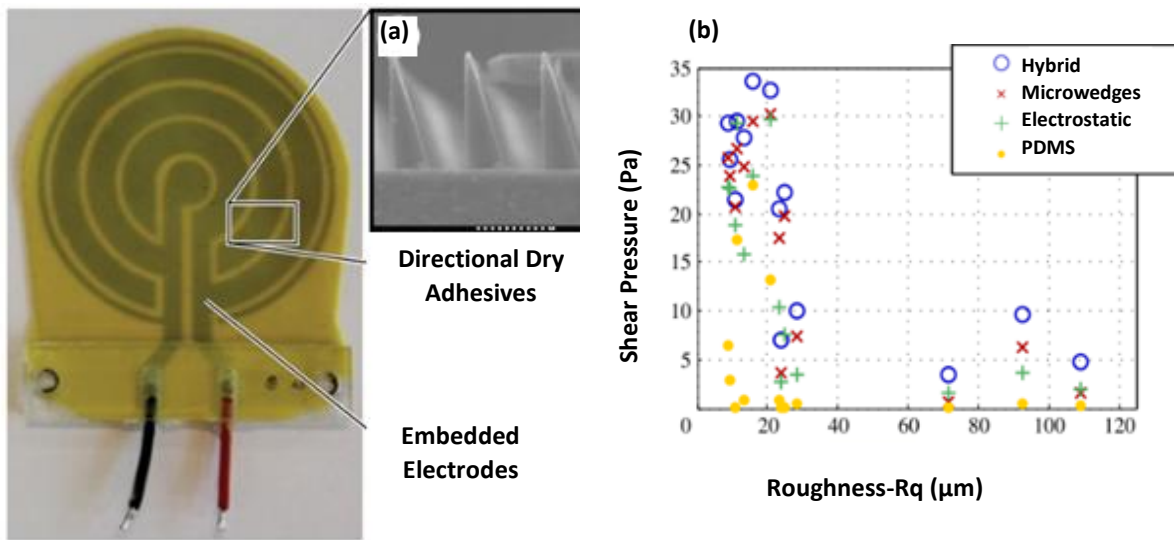


Figure 11 Directional microwedges integrated with interdigitated electrodes -(a) Hybrid electroadhesive device with microwedges (b) Shear stress as a function of surface roughness. On roughness below 10 μm , all adhesive technologies perform closely. For surface roughness > 50 μm , hybrid device has highest adhesive pressures. Reproduced from [61].

2.2.4. Environmental Parameters

The aforementioned parameters allow precise controllability and optimisation of electroadhesive forces. At the same time, environmental conditions such as changes in humidity and temperature also play a role and have been known to account for variability in measured electroadhesion forces reported in different measurements.

Graule, M. A., et al [27] discussed several mechanisms behind the influence of humidity on measured forces. For flat and polished metal surfaces, a layer of moisture on the surface can interact with the adhesive patch via surface tension forces. The authors Graule, M. A., et al [27] observed an increase in adhesion measured on plywood over a factor of 2 when the humidity changed from 10 to 70 % as shown in Figure 12a. On porous surfaces such as wood, an absorbed layer of moisture, causing an increase in surface conductivity, was cited responsible for enhanced forces. Contrarily, flat, non-porous and hydrophilic surfaces may experience the formation of a seal on the perimeter leading to additional role of suction forces.

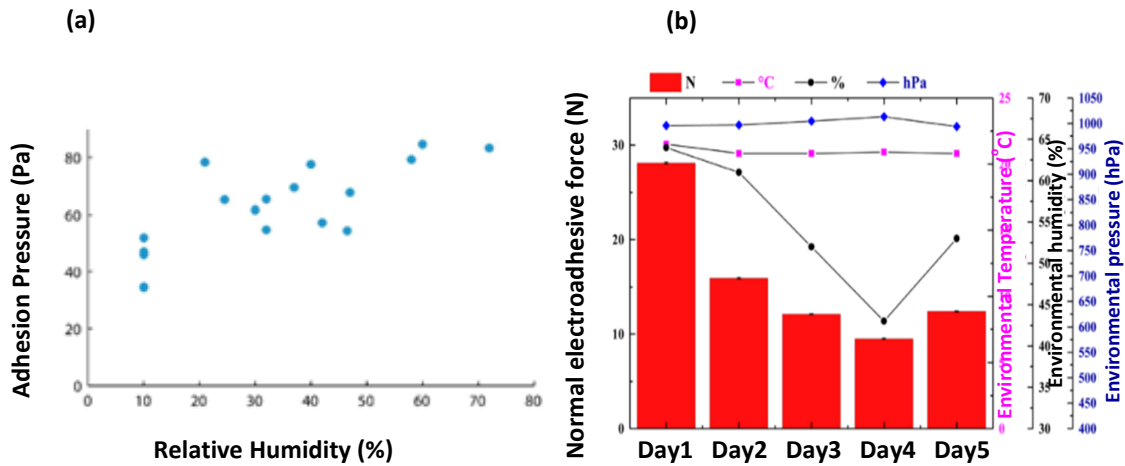


Figure 12 Effect of Humidity on adhesion (a) The effect of relative humidity on electrostatic adhesion on wood. The adhesion pressure on plywood was found to increase with increasing relative humidity. Reproduced from [27] (b) Electroadhesive forces measured on the glass surface over a 5 day period corresponding to the fluctuations in relative humidity and temperature. Reproduced from [49].

In another study, Guo et al observed the recorded forces to drop by more than 60 % when the humidity changed from 64 to 43 % over the course of 5 days as shown in Figure 12b. Thus, electroadhesive forces increase with increasing humidity. The effect of environmental parameters has been accounted as one of the major reasons for the deviation in measured forces and hence a controlled environment is preferred to measure consistent performance.

2.2.5. Dielectric Constant

Most of the studies integrating dry adhesives with electroadhesives have been focussed on studying shear forces. Authors Akherat, et al. , et al. investigated the hybrid (microwedge + electrodes) device by doping the dielectric layer with copper phthalocyanine to ramp up the relative permittivity [60]. Figure 13a shows the bilayer design used in this study. The ground electrode was separated from the high voltage electrodes with a 25 μm Kapton sheet. Insulation rendered this design more robust as it provided resistance to dielectric breakdown. The particle size of the filler ranged from 90 to several 100 nm. Different dopant concentrations of CuPy were tested. Increasing dopant concentration increased the roughness from 3.7 nm (0 % dopant) to 39 nm at 6 % filler concentration. Figure 13b shows the AFM topography for doped elastomeric samples.

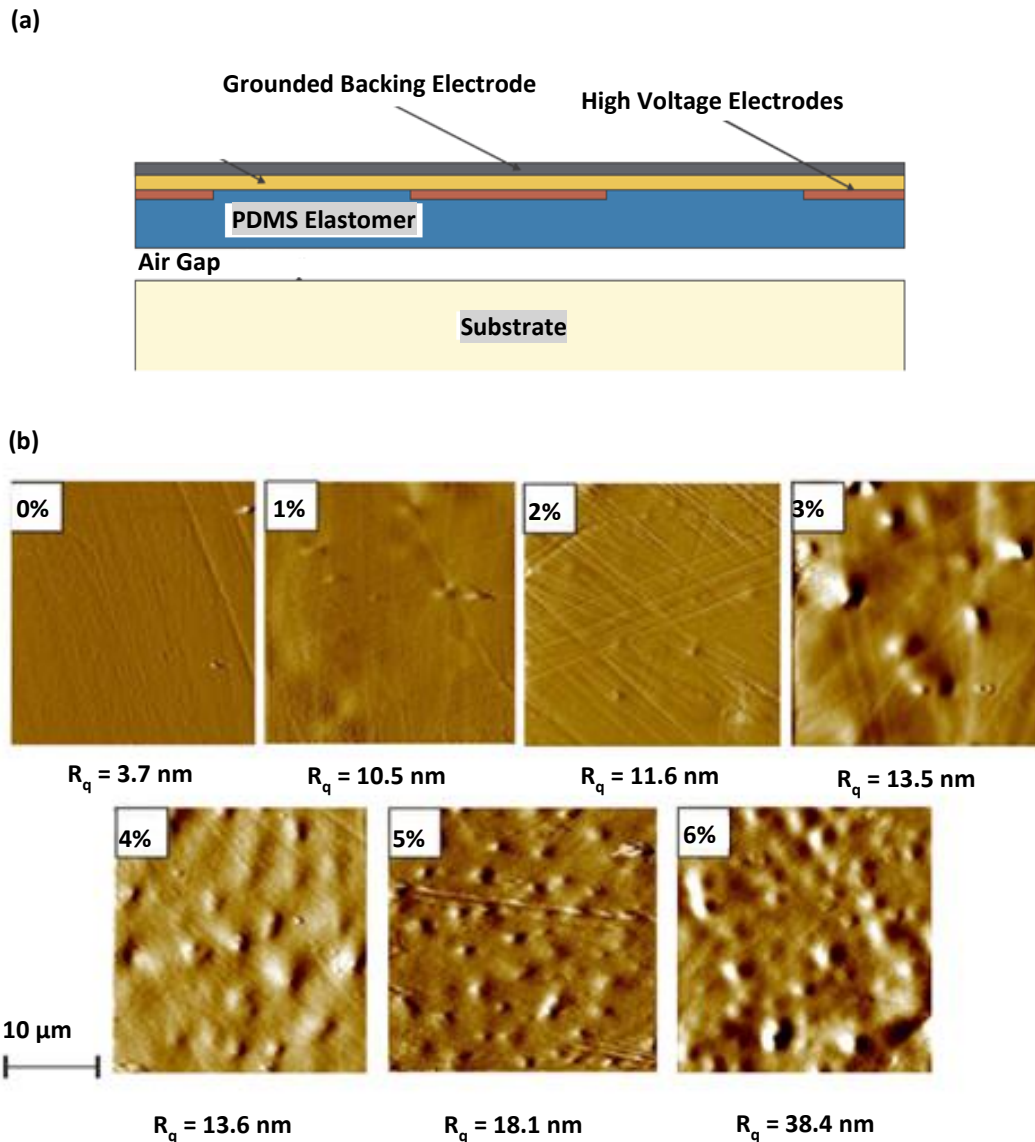


Figure 13 Bi-layer electroadhesive design and effect of filler on roughness (a) The electroadhesive device had a bi-layer design where the high voltage electrodes were separated from the ground electrodes with a Kapton sheet. (b) AFM images of the Cu-Pc (Copper Phthalocyanine) doped elastomeric samples for different weight concentration ratios. The surface roughness RMS varies directly with the dopant's concentration. Reproduced from [60]

The authors [60] selectively doped the backing layer and then the directional microwedges with Copper (II) Phthalocyanine Cu-Pc. Figure 14 shows the shear stress of doped dielectric layer in the electroadhesive as a function of dopant concentration measured on a medium density fibre board (MDF). At an optimum filler weight concentration of 4 %, the relative permittivity was double ($\epsilon_r = 4.5$) as compared to no filler ($\epsilon_r = 2.7$). Further rise in the filler concentration

resulted in loss of adhesion. This drop in the shear stress values has been explained due to the increased surface roughness when filler concentration is increased beyond 4 %.

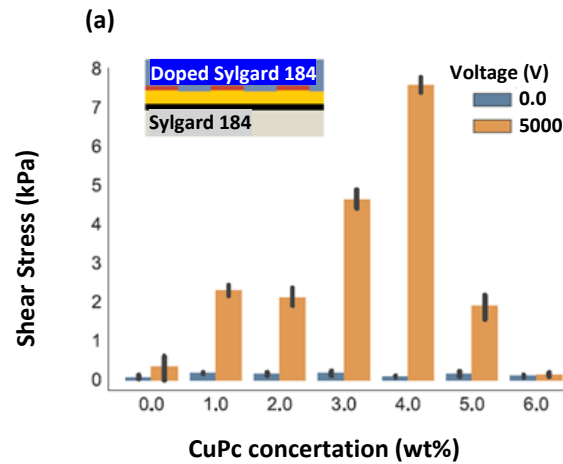


Figure 14 Shear stress measurements for a flat doped dielectric layer. Shear stresses measured on a medium density fibreboard (MDF) for an unstructured bi-layer electroadhesive structure with increasing weight concentration of Copper (II) Pthalocyanine Cu-Pc particles. Reproduced from [60].

Figure 15a shows the shear stress measured on dry wall and medium density fireboard (MDF). All the measurements were performed at a potential bias of 5 kV. R1 is the undoped reference sample with micropatterned structures. C1 is the doped sample with 4 % filler weight concentration. Adhesion enhanced by 1.4 times on the drywall and 3.9 times on MDF. Figure 15b compares the undoped and doped samples where the elastomer used for micropatterning was replaced from Sylgard 184 to Sylgard 170. The latter has a higher dielectric constant and therefore, for a dopant concentration of 4 %, an increment in adhesion by 1.9 times was measured on the dry wall and 2.4 times on MDF. Without the electroadhesive element, the shear stress is higher for Sylgard 184.

The addition of filler particles not only leads to an increased roughness but also changes the mechanical properties of the doped elastomer. As shown in Figure 15c, the microwedges were also doped with a 4 % filler concentration. The shear stress increased by 2.4 times on dry wall and by 1.5 times on MDF. The mechanical properties were not analysed in case of doped microstructures, and therefore could not be compared with doped dielectric layers discussed in Figure 15(a-b).

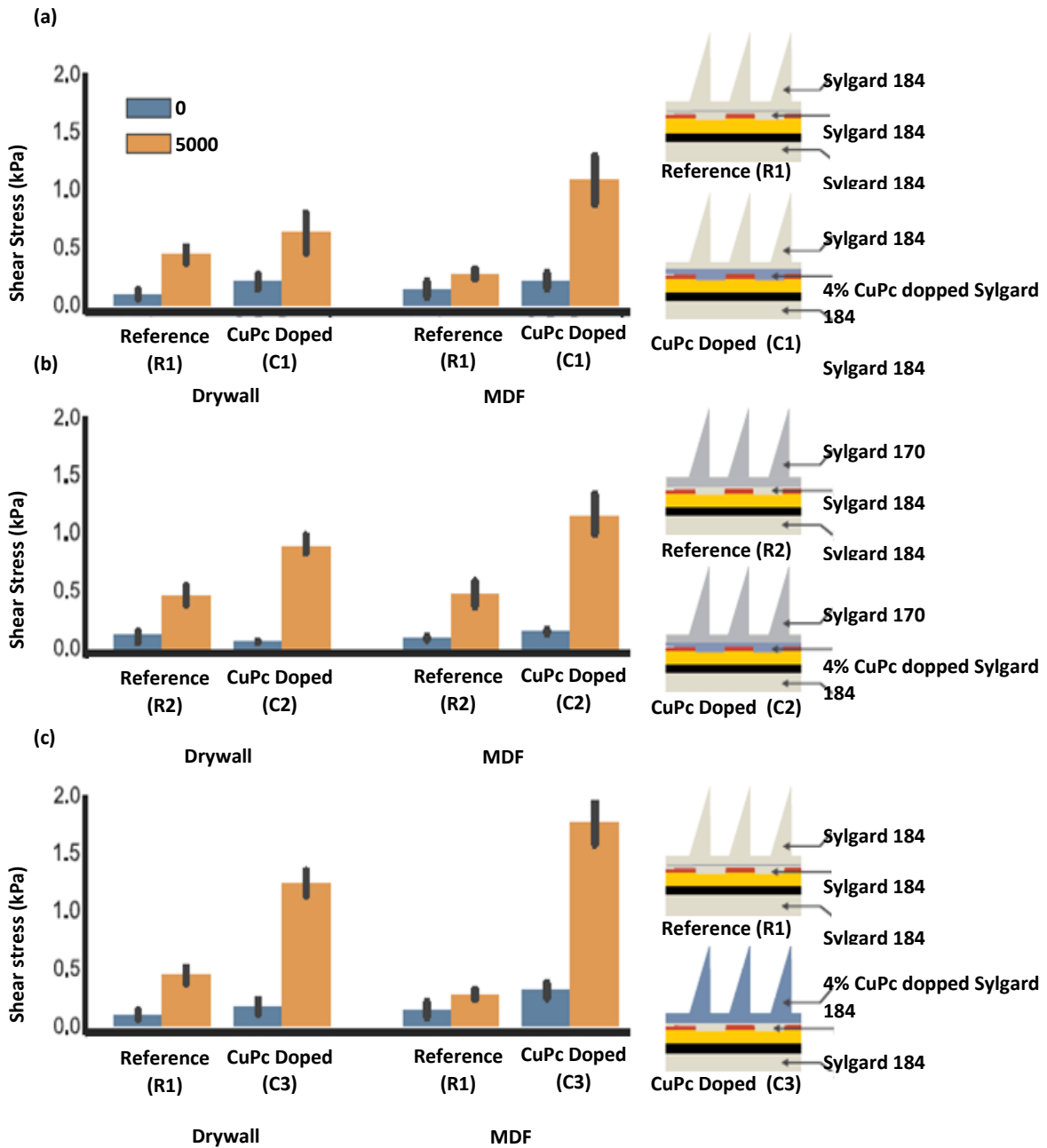


Figure 15 Shear stress measurements of doped and undoped bi-layer electroadhesives- Shear stress measurements on medium density fibre board and drywall substrates (a)R1 is the reference undoped micropatterned sample with Sylgard 184 and C1 is the doped micropatterned sample (b) Sylgard 170 microstructured undoped sample is the reference R2 and C2 is the doped Sylgard 170 sample (c) Reference undoped Sylgard 184 sample is compared to doped microwedges sample R3. Reproduced from [60].

All these theoretical and experimental studies were directed at studying shear forces for applications like wall climbing robots and aerial micro vehicles. Within the scope of this thesis, the focus is laid on studying normal adhesion forces with a micropatterned dielectric.

2.3. Early attempts to combine electroadhesion & micropatterned adhesives

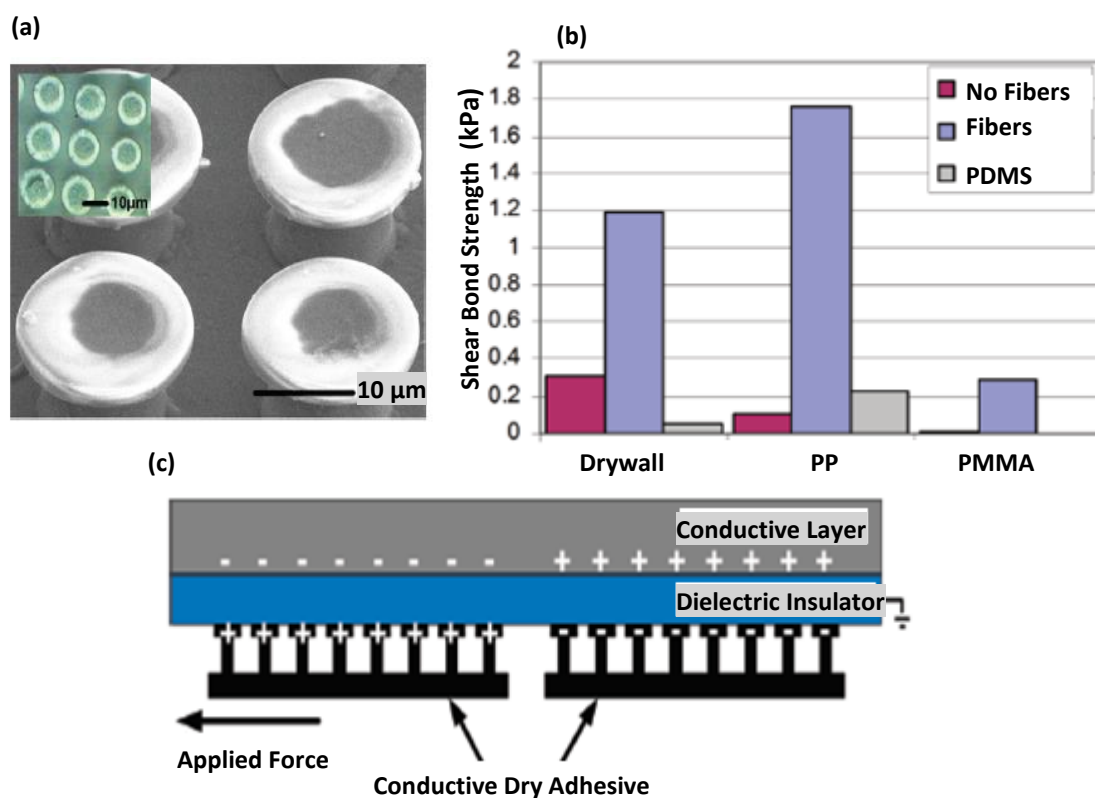


Figure 16 Shear stress measurements for conductive micropatterned adhesives (a) Scanning electron microscope image of conductive carbon black filled PDMS microstructures (b) The increase in shear strength on drywall, polypropylene and polymethacrylate substrates at an electrical potential of 2 kV (c) Concept for using microstructures as electrodes in an electroadhesive device. Reproduced from [45]

There have been few attempts [45] to leverage the advantages offered by electroadhesion and combine it with micropatterned adhesives to design an adhesive pad compliant to smooth and rough surfaces. Both directional [60] and non-directional micropatterns [45] have been tested. Krahn et al. [45] fabricated conductive dry adhesives made from carbon black and

polydimethylsiloxane (PDMS) composites as shown in Figure 16a. They measured shear forces on a steel substrate separated by a polypropylene dielectric layer. These measurements were made at an applied bias of 2 kV. Figure 16b shows that electroadhesives with conductive gecko structures (labelled Fibers) performed better in comparison to the non-conductive adhesives (No Fibres) which were in comparison showing higher adhesion than flat unstructured samples (PDMS). In this study the conductive micropatterns were used as electrodes separated by a dielectric layer from the target object as shown in Figure 16c

In another study, Spenko et. Al designed a bi-layer electroadhesive integrated with non-directional (Figure 17a) and directional (Figure 17b) adhesive structures. In order to ramp up the net adhesive forces, they increased the dielectric permittivity by doping PDMS with copper (II) phthalocyanine. The shear stress measured has been discussed in Figure 15. Both these studies measured the shear forces with and without an applied electric field.

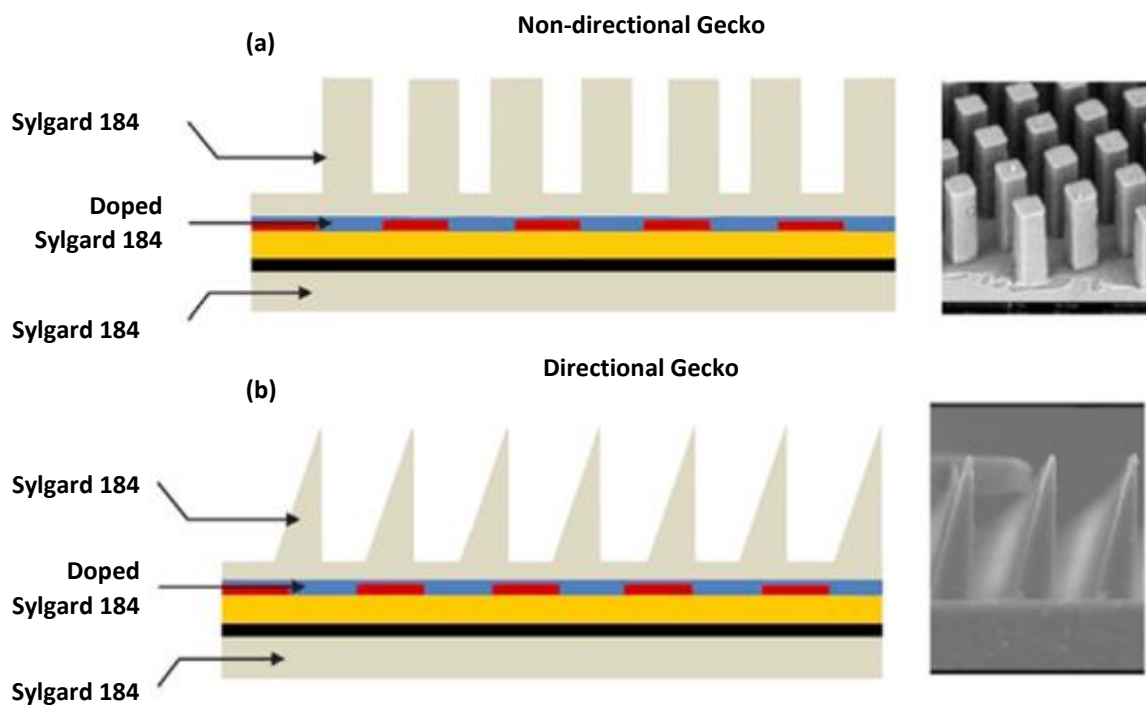


Figure 17 Bi- layer structure of micropatterned electroadhesive using(a) Non- directional structures (b) Directional microwedges. Reproduced from [60]

CaO et al. investigated the effect of different geometrical and material parameters as is further discussed in Section 2.2.1 . Furthermore, they modelled the design for integrating gecko structures with interdigitated electrodes as shown in Figure 18. The experimental work in the thesis advances the understanding of the subject of combining dry adhesives and electroadhesives on normal adhesion.

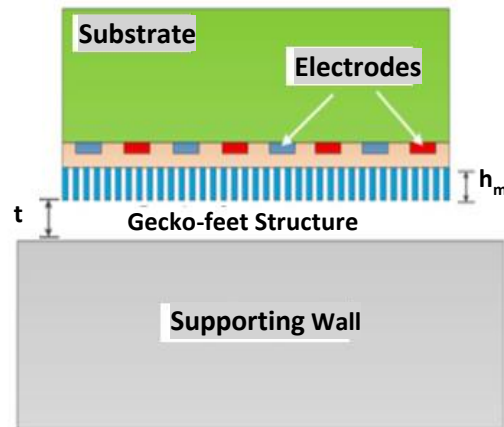


Figure 18 Model design for a micropatterned electroadhesive pad(a) Schematic representation of an electroadhesive pad with artificial hairs mimicking gecko structures (shown in blue). Reproduced from [48]

2.4. Switchable Adhesion

While electroadhesion enables dynamic regulation of the adhesive forces, release mechanisms are equally critical for detaching the adhesives for handling and micromanipulation of objects. In this context, electroactuation is discussed in the subsequent sections. Depending on the type of target object, different technologies are being adopted for handling them [63]. These can be summarised in Figure 19. The ability to switch between adhesive and non-adhesive states allows greater control in an adhesive system.

. Thermal [64], magnetic [65], pneumatic [66][67][68], light [11] and mechanical stimuli [69] have so far been reported for regulating the adhesion in micropatterned dry adhesives. In order to respond to these external triggers, the adhesives must be modified in either their material or design properties. Kizilkan, E. et al designed a bioinspired photo-controllable device composed

of liquid crystalline polymers with an azo benzene unit. The device had a micropatterned PDMS adhesive layer on the top surface.



Figure 19 Different gripping technologies depending on the object types. Reproduced from [63].

UV illumination led to photoisomerization of the azo-benzene units, leading to change in shape [11] consequently leading to loss of contact between the glass microsphere and the device. As shown in Figure 20a, switching off the UV light allowed the adhesive device to restore the original shape and return to the adhesive state. Figure 20b shows force time curve of the process where the device was in contact with a glass microsphere and then subjected to UV illumination. At a distance of 50 μm , UV illumination leads to bending of the structure establishing contact with the glass microsphere. Among other routes, pneumatic approaches are among the most common. Sitti et al. designed a pneumatic gripper integrated with a micropatterned layer of mushroom tip polyurethane pillars[67]. When the device is deflated, most of the pillars are in contact with the target material (in this case a steel ball) as shown in Figure 20c. On inflating the device, the pillars start to peel and lose contact. In the end only few pillars at the centre are still in contact until complete detachment occurs. By controlling the air pressure, they demonstrated handling of different curved and flat surfaces. Figure 20d shows the peeling process (i-vi) and corresponding detachment of pillars with increasing air pressure.

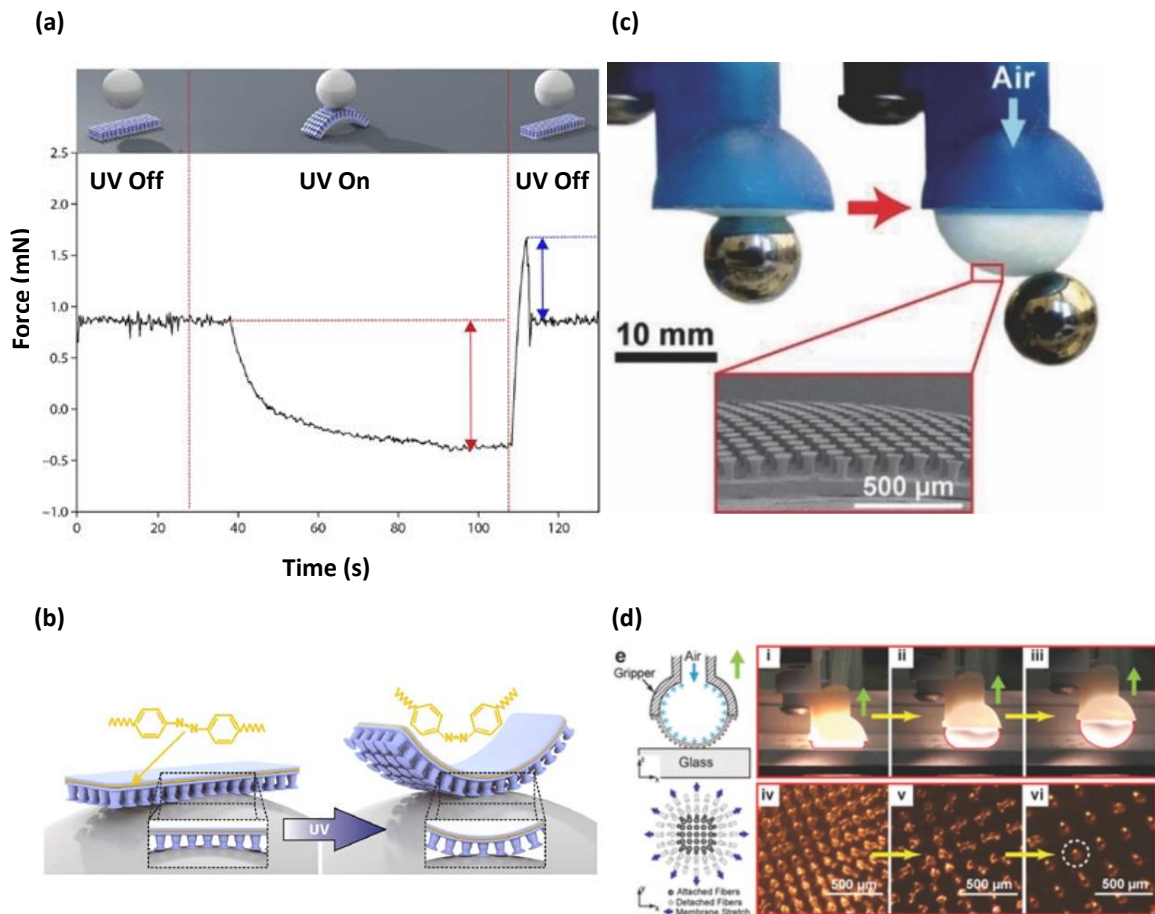


Figure 20 Fabrication and working of a photo-controllable and a pneumatic adhesive system - (a) The photo-controllable device consists of a crosslinked azo-benzene containing liquid crystalline elastomer unit. At 50 μm, UV light illumination causes the device to expand and contact the glass sphere. UV driven preload is measured. When the illumination is switched off, the device contracts and detaches from the glass sphere. (b) Photo-isomerisation leads to change in shape of the azobenzene units leading to loss of contact area. Reproduced from [11] (c) Fibrillar adhesive device holding a 12.7 mm in diameter steel ball with complete and reduced contact area (d) (i – vi) depict the movement of different pillars once the device is inflated. When the device is fully inflated, only pillars at the centre are in contact, Modulating the air pressure enables the device to handle flat and curved surfaces. Reproduced from [67]

2.5. Electroactuation

The underlying principle in these approaches has been to induce a reversible deformation by applying the trigger, which in turn reduces the contact area and thereby weakens adhesion. Lately, electrical forces have also been directed to achieve this transition between the adhesive and non-adhesive states by using dielectric elastomeric actuators. Two synergistic effects

namely the Maxwell stress and electrostriction come into play when a dielectric medium is subjected to an externally applied electric field.

Maxwell stress as previously discussed in section 2.1.3 arises from the Coulombic interaction between free charges on the surface of the interacting bodies. In the case of dielectric elastomers, which are primarily amorphous polymers, Maxwell stress leads to the stretching of the polymer chains and is a dominant factor resulting in the deformation [70][71].

Electrostriction on the other hand, arises from the polarisation of the material and takes precedence in piezo and ferroelectric crystals due their crystalline nature.

This electro-mechanical coupling called electrostriction [13][12] distinguishes electrostrictive polymers from dielectric elastomers such as silicones.

2.5.1. Dielectric Elastomeric Actuators

Electrical fields are capable of inducing deformation in electroactive polymers. This effect of Maxwell stress is exploited in Dielectric Elastomeric Actuators (DEA). DEAs are compliant capacitors, consisting of a layer of dielectric film sandwiched between two compliant electrodes [72]. Applying a potential bias across the film creates electrostatic attraction between the electrodes, in turn compressing the film along the thickness direction. Being incompressible in nature, the film expands in area [73]. The operating principle is shown in Figure 21. Perline et al. [74] calculated the effective pressure (change in electrostatic energy per unit area per unit thickness of the dielectric) as a function of the electric field and the relative permittivity of the dielectric film.

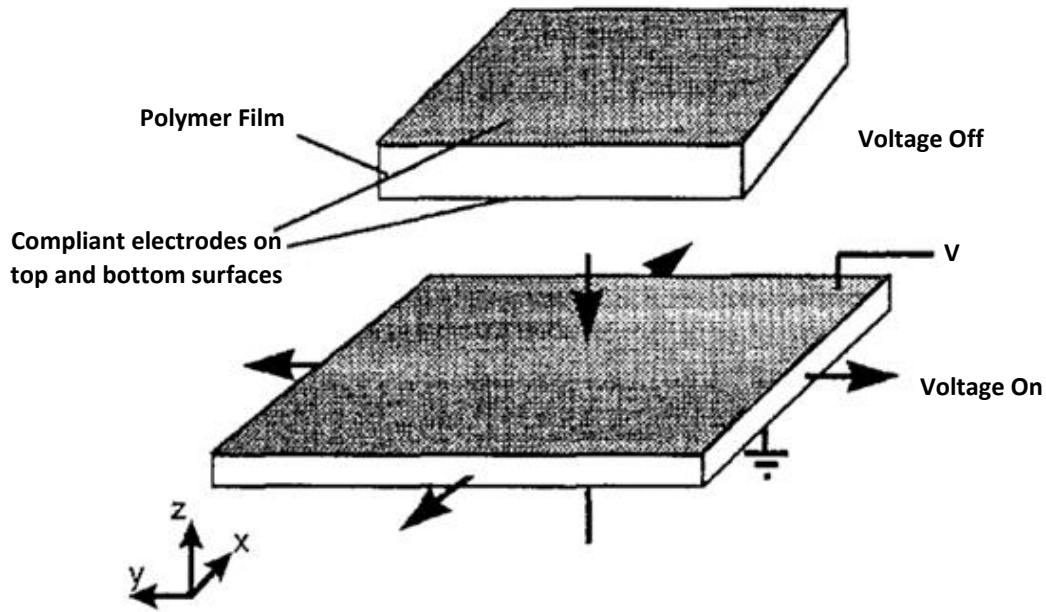


Figure 21 Operating principle of an electrostrictive polymer actuator. Reproduced from [72]

$$p = \epsilon_0 \epsilon E^2$$

2. 13

where, p is the effective pressure (actuation force per unit area), ϵ_0 is the permittivity of free space, ϵ is the relative dielectric constant and E is the applied electric field. One of the key advantages of the DEA technology as compared to its counterparts is the control over local deformations that can be programmed by constraining the film leading to anisotropic elongation as desired [75]. In this direction, different multi-segment actuators have been designed where the deformation can be selectively controlled in different segments [76]. Several different approaches have been employed to achieve in plane and out of plane actuation.

2.5.2. DEA Fundamentals

I. Conformal Electrodes

Stretchable electrodes are the key component of a DEA. In order to facilitate typical axial strain deformations (10-100 %), and still stay conductive, the electrodes sandwiching the dielectric

layer must be stretchable [77][78]. Compliant electrodes avoid stiffening the system. Different methods have been explored to fabricate compliant electrodes. These electrodes are either carbon based [79] or metallic [80].

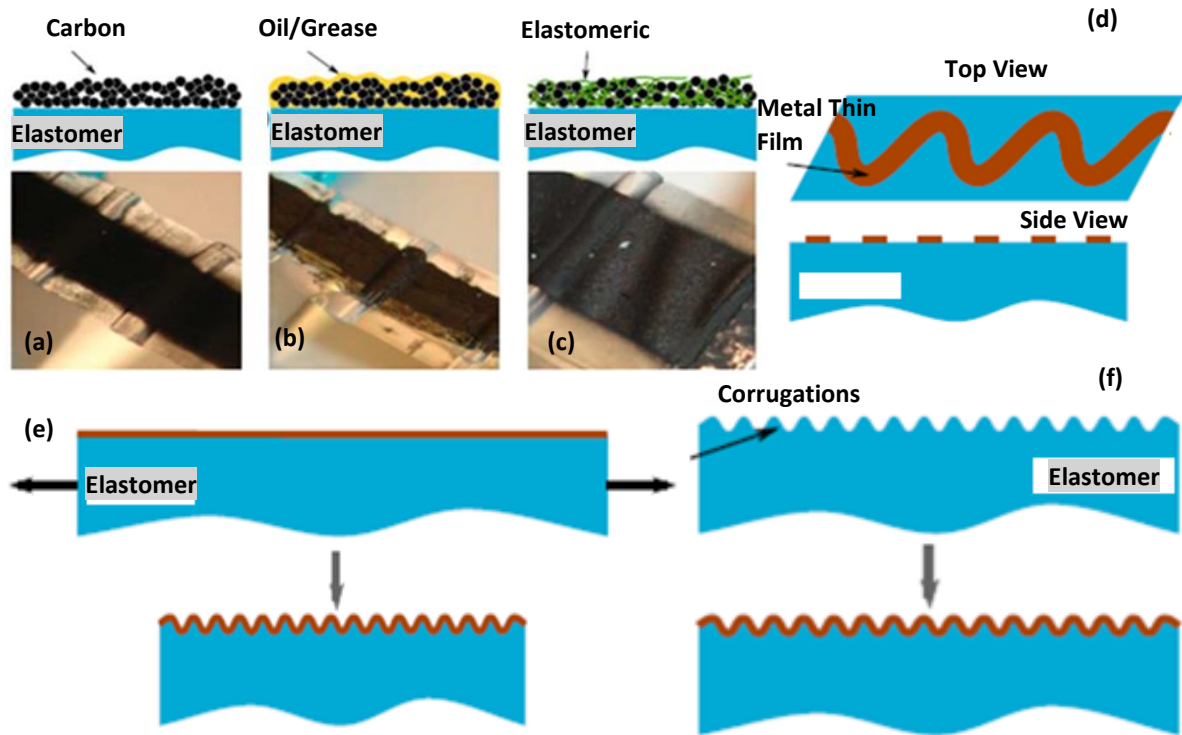


Figure 22 Different approaches for fabricating compliant electrodes: (a) Loose carbon powders applied on the elastomeric layer, (b) Carbon particles suspended in the viscous oil, (c) Conductive silicone composite by doping carbon particles, (d) Photolithographically patterned metallic electrodes, (e) Metallic electrodes deposited on a pre stretched membrane. Releasing the membrane leads to out of plane buckling (f). Reproduced from [78]

Carbon Electrodes:

Being dispersed in the form of loose powders (Figure 22a) or integrated in an elastomeric matrix (Figure 22c), carbon-based electrodes are among the most commonly used electrodes. While loose powders can be easily spray coated or brushed, they do not ensure homogenous coverage and long-term stability.

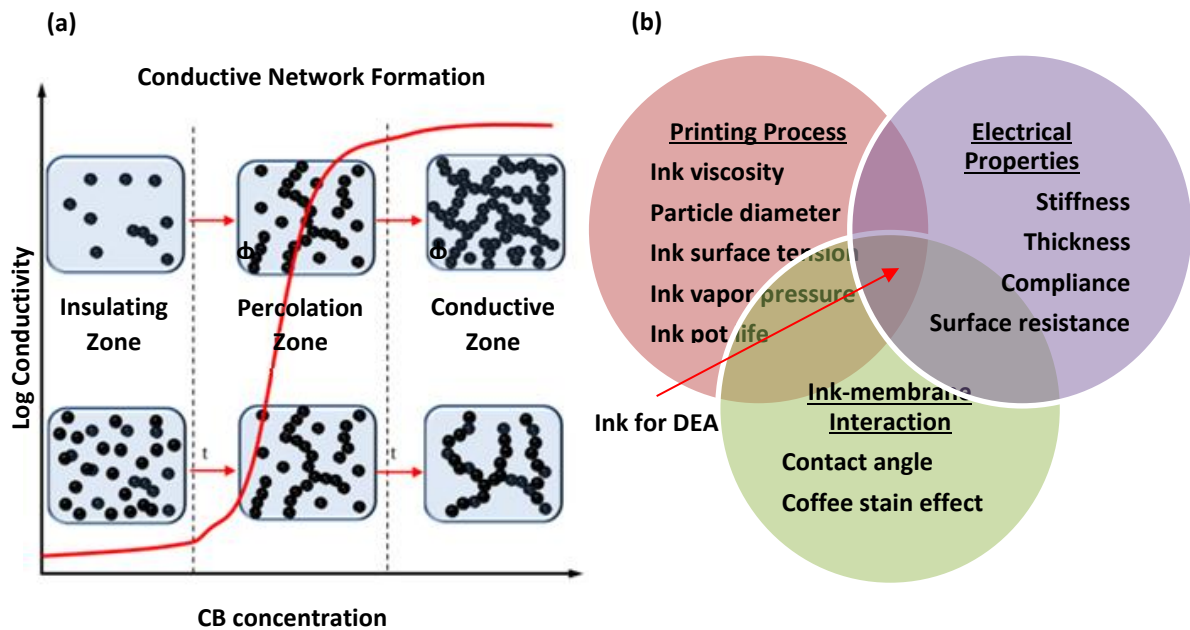


Figure 23 Parametric space for making conductive inks (a) Schematic representing the percolation threshold for conductive fillers as a function of filler concentration (b) Parameter space for conductive injectable inks for DEA applications. Reproduced from [78].

Conductive carbon particles are also embedded in elastomeric matrices to make composite blends. The stiffness of the composite is governed by the filler size and concentration. Percolation theory broadly explains the electrically conducting behavior of conductive composites [67]. When the filler content is gradually increased, the composite undergoes an insulator-to-conductor transition. The critical filler content at this transition is referred to as the percolation threshold [69]. The formation of continuous electron paths or conducting networks (Figure 23 a) leads to a sharp increase in conductivity. In order to adapt these carbon fillers to large scale applications and to make them processable for roll to roll manufacturing and inkjet processes, they can be processed into conductive inks. Figure 23 b represents the desirable properties for preparing conductive inks for DEA applications.

Metallic electrodes:

Three different methods have been tested [81] [82] to deposit metallic electrodes without significantly stiffening the system and hence lowering the strain output. Metal electrodes are sputter deposited on elastomers. These can be later patterned by photolithography to create zigzag patterns as shown in Figure 22d. The zig zag patterns enable uniaxial tensile strain in

the direction of patterning. Other approaches involve pre-stretching the membrane prior to the deposition of electrodes [81] (Figure 22 e) . Releasing the membrane leads to out of plane deformations. Depositing electrodes on wavy silicone mold for creating corrugated surfaces has also been positively investigated [82] (Figure 22f).

II. Dielectric Material

The strain across the thickness of the dielectric membrane in a DEA (Figure 21) is approximated by [73][72]:

$$s_z = -\frac{\epsilon_r \epsilon_0 V^2}{YZ^2} \tag{2.14}$$

where Y is the Young's modulus of the elastomer, and z is the thickness of the membrane. Soft elastomers like silicones, acrylic or polyurethane are most commonly used across different DEA applications. For applications that require high strains (> 10 %), acrylics are preferred over silicones [83]. On the other hand, silicones are better suited where fast electromechanical response with high reproducibility is needed [84]. S. Michel, et al. compared the Dow Corning silicone (DC 3481) and acrylic polymers VHB 4910 and F- 9473PC. Figure 24 shows the DMTA results for the two polymers. The moduli and phase shift were measured in the temperature range from -150 °C to 150 °C. The mechanical efficiency of the actuator is a function of the tangent of the phase shift [83].

$$\mu_m = \frac{1}{1 + \tan \delta} \tag{2.15}$$

where

$$\delta = \frac{G''}{G'} \tag{2.16}$$

where μ_m is the mechanical efficiency, δ is the phase shift, G' is the storage modulus and G'' is the loss modulus.

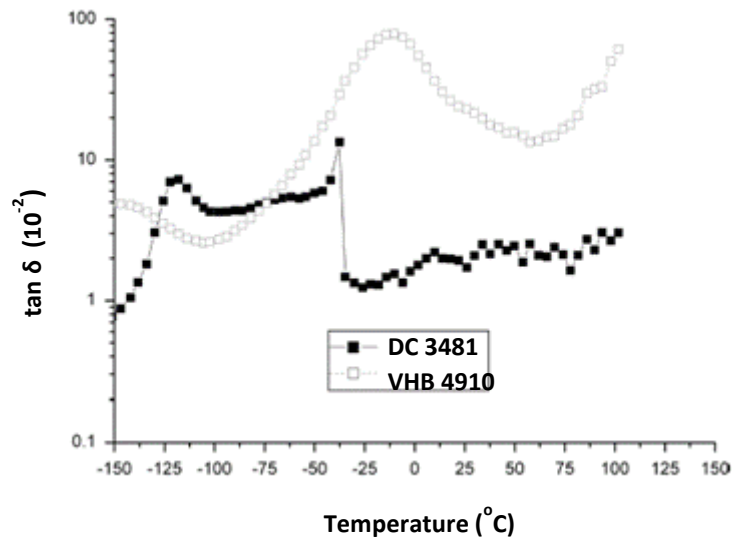


Figure 24 Torsional DMTA results of silicone DC 3481 and acrylic VHB 4910 elastomers. Reproduced from [83].

Although silicones have fast electromechanical response, their permittivity is typically low. Figure 24 shows the glass transition temperature of silicone and acrylic elastomers. The silicone has a narrow peak at -38 $^{\circ}\text{C}$ as opposed to a broad peak in the acrylic elastomer seen at -6 $^{\circ}\text{C}$. Silicones have a comparably smaller glass transition temperature range. Figure 25 shows the different elastomers that have been investigated for applications in DEA.

Different fillers such as BaTiO_3 , TiO_2 and others have been added to different elastomeric matrices. However, high filler concentrations also influence the mechanical properties of the dielectric, thereby increasing the stiffness of the system. Wacker Chemie AG has manufactured silicones by covalent modification of the siloxane polymer chain. With polymers such as Elastosil 5020 and Elastosil 2030 along with high permittivity, the Young's modulus can be tuned between 0.1 and 2.5 MPa [85]. Other high permittivity polymers have also been fabricated to achieve high strains at low driving voltages [86].

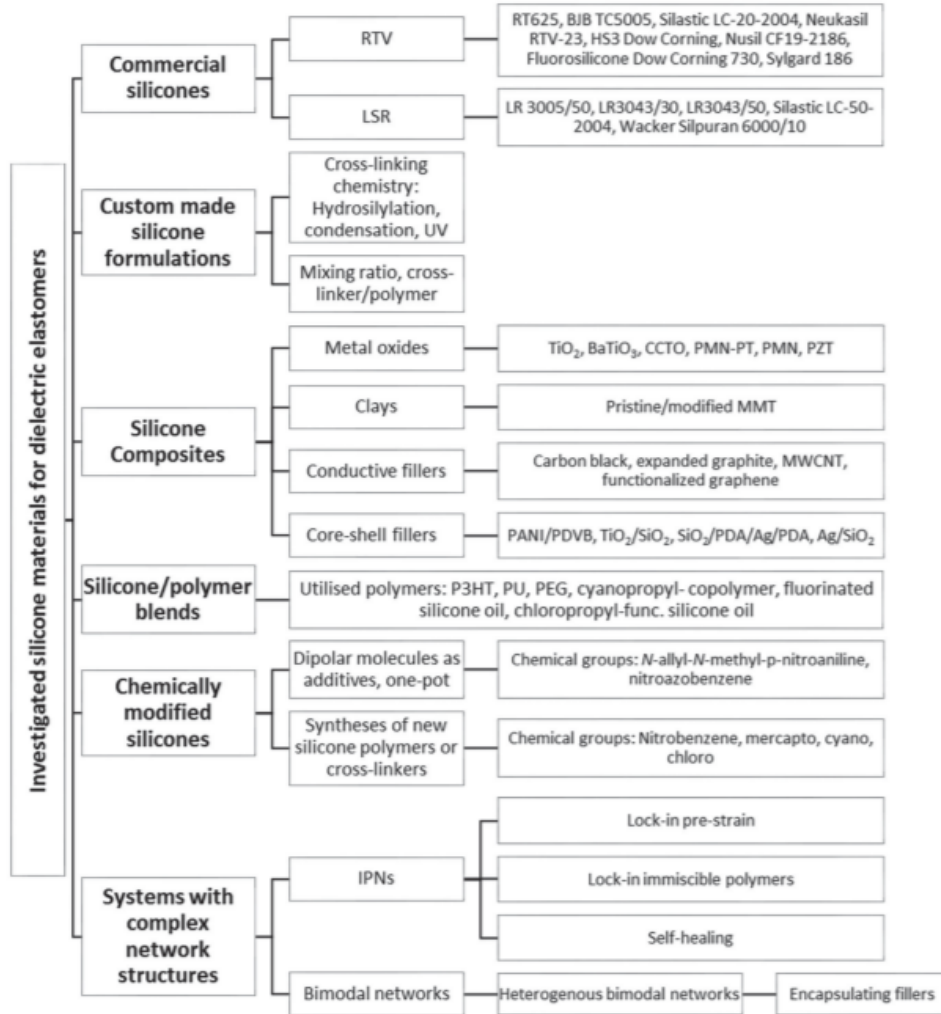


Figure 25 Schematic overview of the silicone dielectric elastomeric materials. Reproduced from [84].

III. Mechanical Pre-stretch

A DEA actuator undergoing deformation in the presence of a voltage is subjected to different modes of instabilities [87]. As soon as the voltage bias is applied, the dielectric membrane is compressed in the thickness region. As the thickness decreases, the same electric field is now acting across the reduced thickness intensely compressing it further. This instability is called the pull-in instability and is marked by λ_c in Figure 26. At higher strains, when the DEA passes the point of pull-in instability, it operates in a regime marked by red, termed as the snap-through instability until the point of complete elongation of the polymeric chains. λ_{lim} marks the elongation limit of the polymer chains.

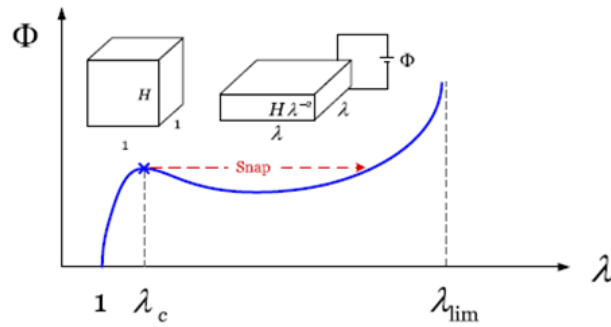


Figure 26 Instabilities in a dielectric actuator undergoing deformation in an applied electric field. Under an applied voltage, the dielectric elastomer fails at the pull-in instability at λ_c or snaps to a thinner state near λ_{lim} . Reproduced from [87].

By mechanically pre-stretching the membrane, the dielectric membrane stiffens, and the DEA operates in the thinner and stiffer region with a constant deformation until electrical breakdown occurs. Moreover, as prestretching reduces the thickness of the dielectric, the operating voltage is also reduced, which is desirable in all DEA applications.

2.5.3. Actuator Configurations

There are two main configurations of elastomeric actuators [88][89]: stack and membrane actuators, as show in Figure 27.

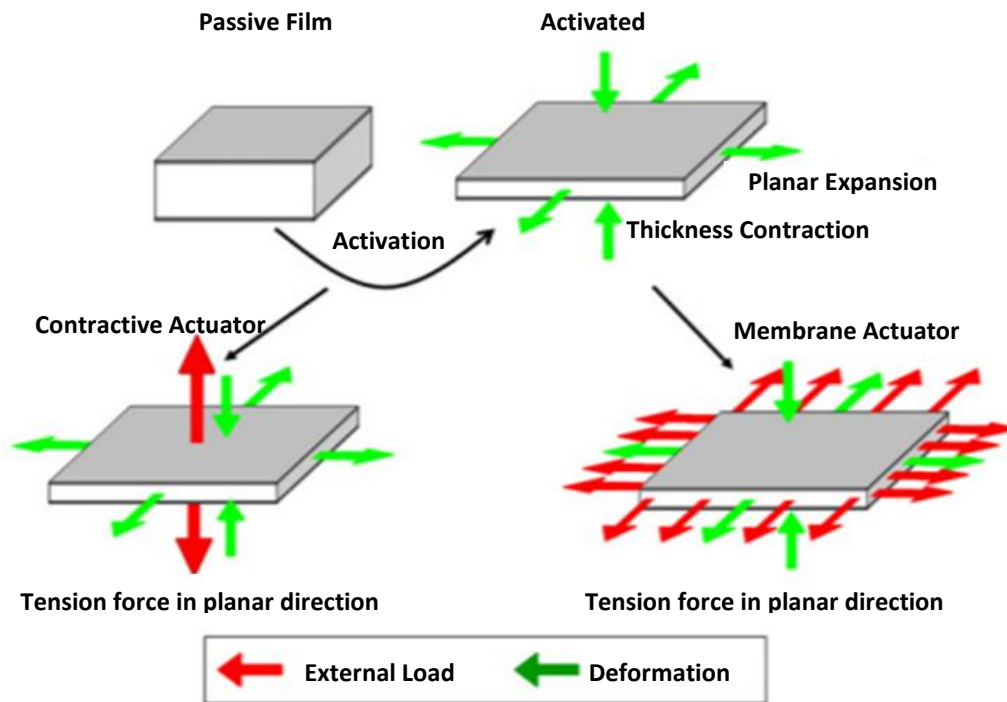


Figure 27 Actuator Configurations: Stack or contractive actuator and membrane or expanding actuator. Reproduced from [88].

I. Stack Actuators

The principle of DEA operation has been described in section 2.3.1. The earlier applications of DEA exploited the in-plane expansion of the dielectric membrane. However, the compression of the film along the thickness has also been explored by designing stack actuators. Stack actuators consist of layers of DEA which are alternately biased by electric fields. Therefore, mechanically they are connected in series and electrically parallel. As soon as the electric field is applied across the stack, the entire stack compresses. The net deformation achieved in a stack actuator is the sum of contraction of individual modules [90]. Different approaches have been tried for combining these single membranes into stacks. Schlaak et al. [91] developed a process where they heat cross linked silicone followed by deposition of electrodes via a shadow mask. This process could be repeated alternately to create a stack of up to 100 layers. Figure 28 shows the working of a stack actuator. The design consists of layers of dielectric films sandwiched between films of alternate polarities and requires passive area around the sheets for actuation. Actuation strains in the range of 5-20 % have been reported.

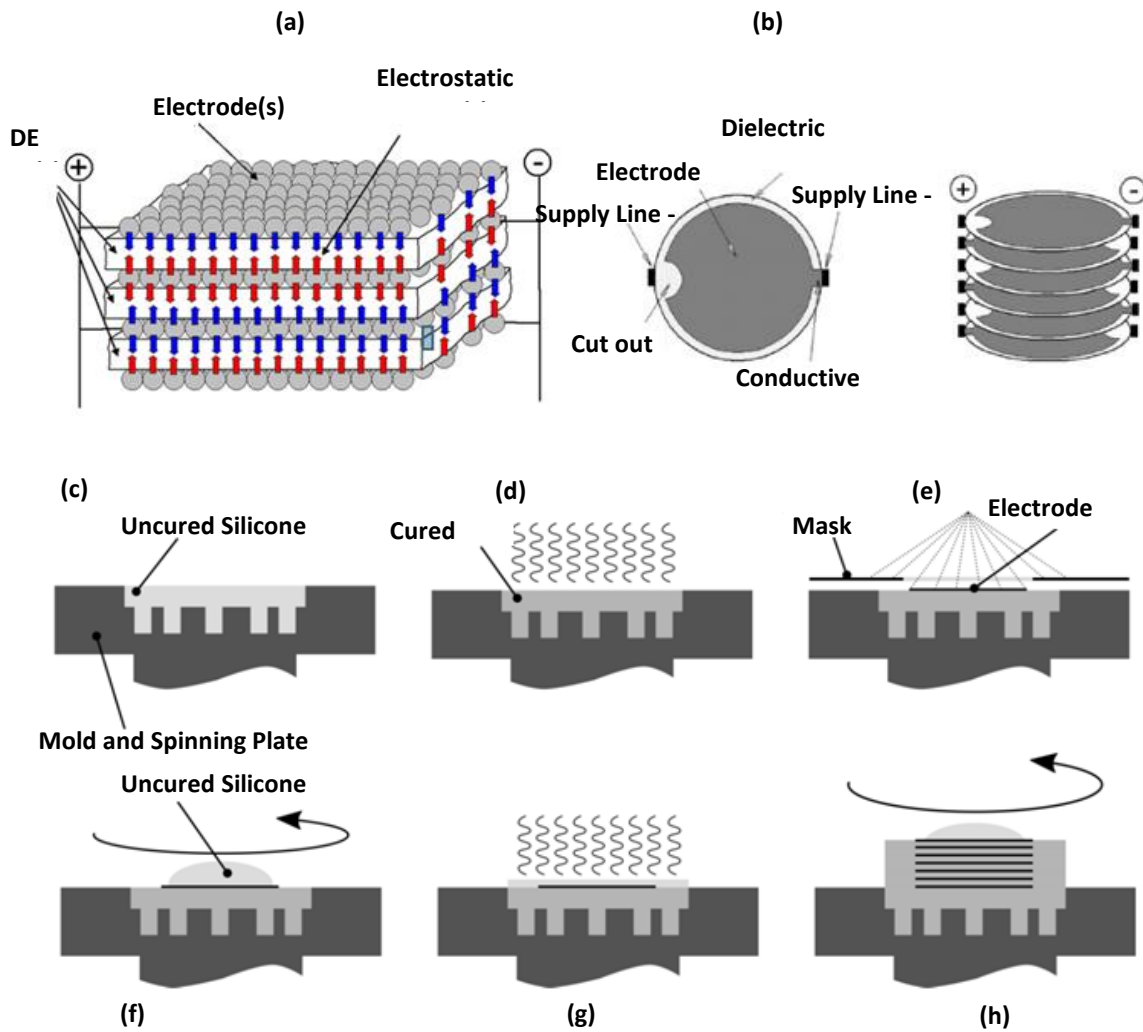


Figure 28 (a), (b) Layerwise composite structure of the stack DEA and its fabrication process. It is composed of alternating electrode and DE film layers. Reproduced from [88] (b-h) Fabrication process of stack DEA. (c) The mold for the micropatterns is filled with uncured silicone (d) Thermal curing of elastomer (e) The electrodes are spray coated (f) followed by spin coating of the subsequent dielectric layer (g) Thermal curing of the elastomer layer (h) the process is repeated until the desired number of layers have been stacked. Reproduced from [91].

II. Membrane Actuators

In membrane actuators the actuation takes place in the direction transverse to the applied electric field. Typically, these actuators are biaxially pre-stretched or biased with external elements to generate considerable strain [92]. Membrane actuators can further be classified as in plane and out of plane actuators. Circular In plane DEAs [93] (expanding circle DEA), Ring electrode DEA and Strip In Plane actuators are some of the most common In plane membrane

actuators. Cone actuators or Circular Out of Plane actuators represent the out of plane membrane actuators.

2.6. DEA Applications: Pick and Place

A brief overview of these configurations demonstrates the flexibility of design that is possible with DEA. These mechanisms have been used for different applications ranging from tunable lenses [94] to 2D mechanical simulation for cell culturing [95], for loudspeakers [96] to vibrotactile haptic devices [97].

Use of DEAs has lately been also directed towards grippers for pick and place applications. Schlaak et al [91] working with dielectric stack actuators, combined their actuators with dry patterned adhesives to design a switchable strategy for handling glass wafers as shown in Figure 29. At an applied bias of 2.5 kV, they could release a glass wafer weighing 12 g in 1s. They maximised the thickness compression by incorporating a stack of 60 dielectric layers in their device.

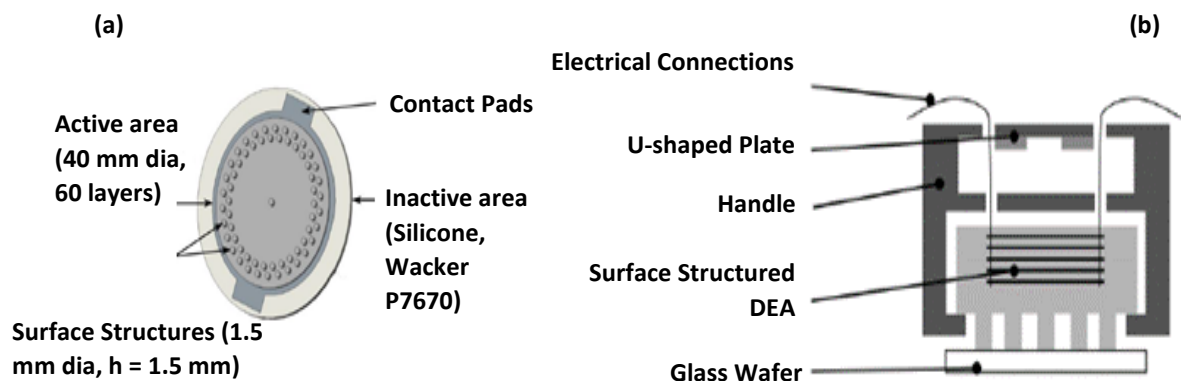


Figure 29 Stack actuator integrated with micropatterned adhesive layer (a) The prototype for stack actuator integrated with micropatterned structures. (b) Experimental set up to test the handling of the glass wafer using the stack DEA. Reproduced from [91].

In another design, Gao et al.[98] combined electroadhesion for gripping and resonant action of DEAs for releasing different surfaces [98]. They investigated the adhesion and release on different lightweight materials such as polypropylene, Mylar (common packaging material) and polyimide used in flexible circuits.

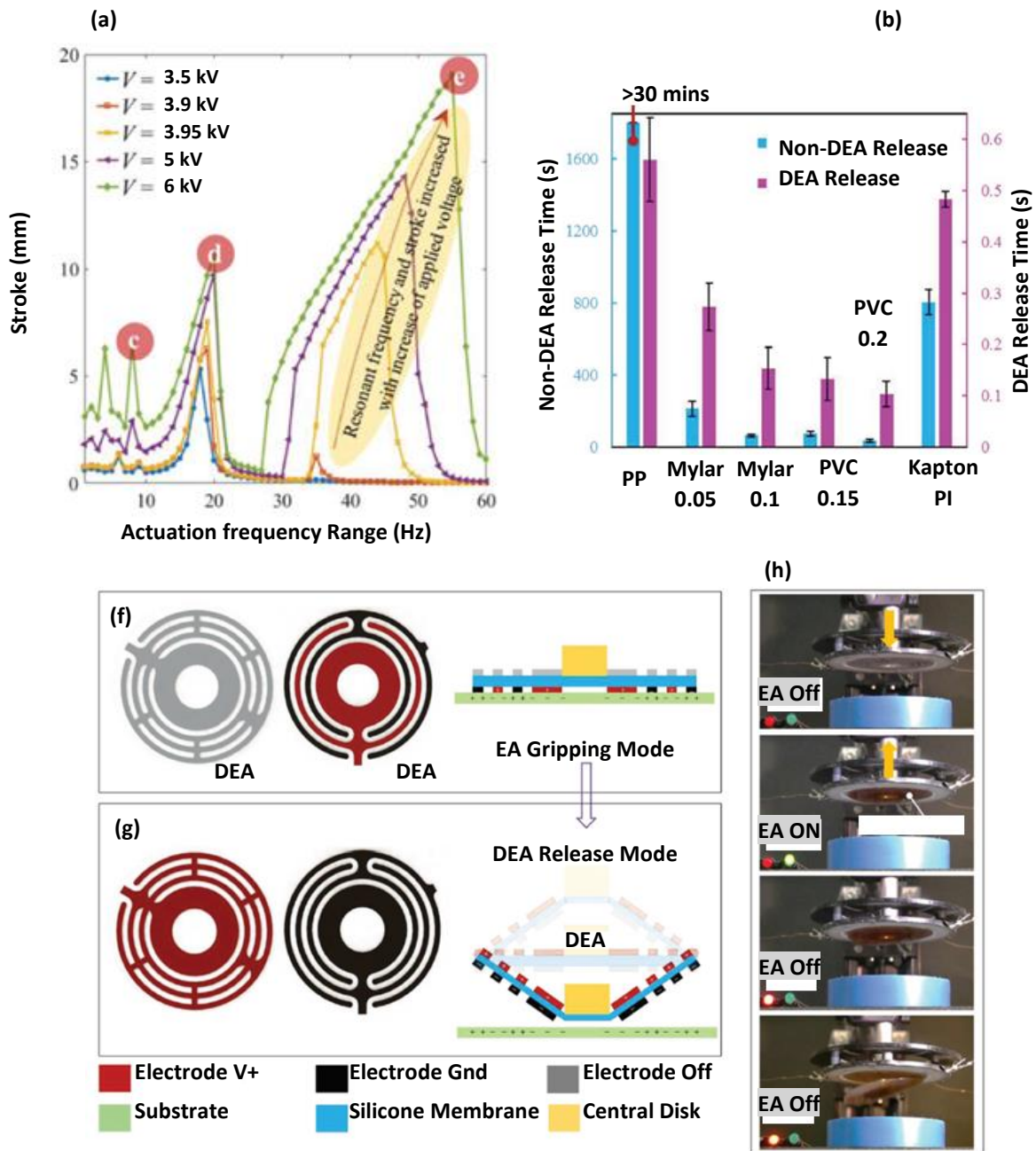


Figure 30 Design and operation of a device gripping via electroadhesion and releasing via use of out of plane actuation of a DEA (a) Square wave frequency from 1 to 60 Hz with applied voltages ranging from 3.5 kV to 6 kV (b) Release period without DEA oscillator (blue) and with DEA oscillator (red) (c) Oscillation profile at 8 Hz (d) Oscillation profile at 20 Hz (e) Oscillation profile at 55 Hz (f) Electroadhesive gripping mode (g) DEA release mode (h) Selectively engaging the electroadhesive and DEA oscillatory mode for handling of Kapton film. Reproduced from [98]

By incorporating DEA vibration in the device, the release times were reduced to a few ms as compared to few min. Figure 30a depicts the DEA stroke as a function of actuation voltage and frequency. At 3.5 kV, the fundamental frequency stroke peak is observed at 18 Hz. However, with increasing voltages, a second harmonic is observed at 35 Hz. The authors reported that with increasing voltage, the amplitude and the frequency of the second peak increased which led to shorter release times. Figure 30f shows the state in which the DEA is switched off and only the Electroadhesive gripping mode is enabled; Figure 30g depicts the release mechanism with the resonant DEA mode. Figure 30 h depicts the pick and place process of a Kapton film. Figure 30b shows the release times when the release process was solely determined by electroadhesion as compared to tapping in resonant vibration of DEAs. DEA assisted release allowed to shorten the release times by over two orders of magnitude compared to non-DEA release [98].

Both the above approaches leverage out of plane actuation of DEA as release mechanisms. Few approaches have also been reported using membrane actuators, which can bend uniaxially, and beam bending has been explored for such pick and place applications. One of the methods to ensure uniaxial elongation in DEAs has been to pre-stretch and confine the dielectric films in rigid frames. Frames add additional weight and complexity to the design. Shian et al, combined fibres with the dielectric film to break the symmetry and steer the bending direction along the direction of the fibres [75]. The design consisted of a bilayer where the active dielectric layer was combined with a passive layer and the fibre was located at the interface of the active and passive layers as shown in Figure 31a.

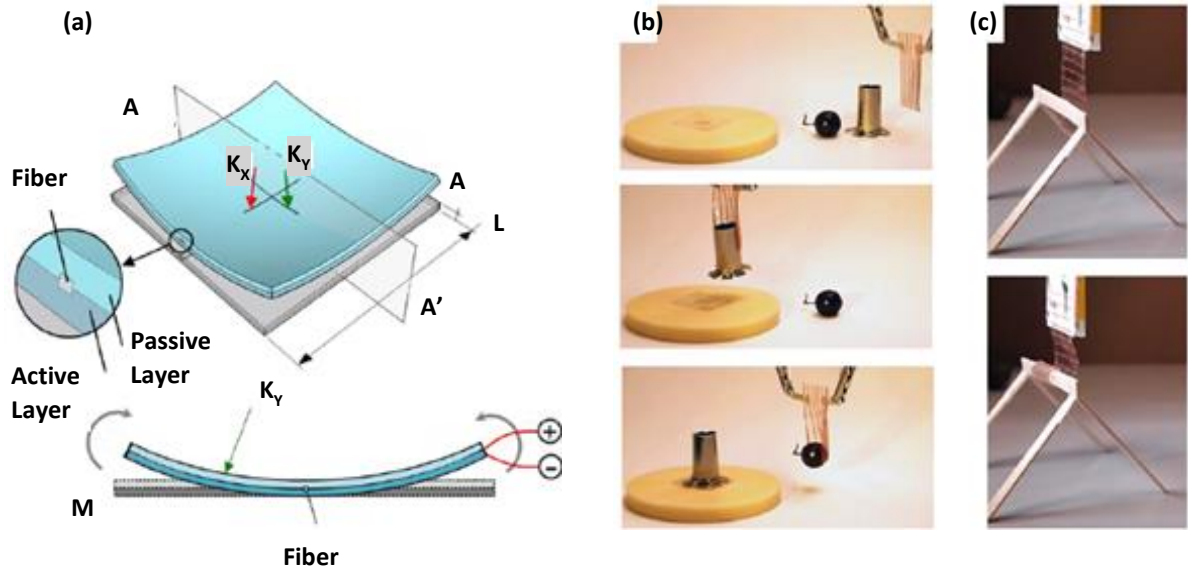


Figure 31 Schematic showing the position of fibres in a bi layer actuator and pick and place by controlling the bending direction (a) Finite element simulations of a bi layer structure consisting of a passive elastomer sheet bonded to a voltage actuated elastomer ($L/H = 25$, fibre width and heights ($H/10$)). The lower image shows the cross-sectional view showing the location of the fibre and the bending moment (b) and (c) Handling of curved and soft materials by uniaxially bending the DEA. Reproduced from [75]

These fibres were able to break the four-fold symmetry and, depending on their location, to control the direction of beam deflection. Figure 31(b-c) shows uniaxial deformation of DEA for picking up a curved cylinder, a soft grape and horizontal wrapping up of a wooden structure.

Vertical grippers designed by Shea et al [59] were another prototype that combined electroadhesion and electrostriction for regulating the pick and place processes as shown in Figure 32.

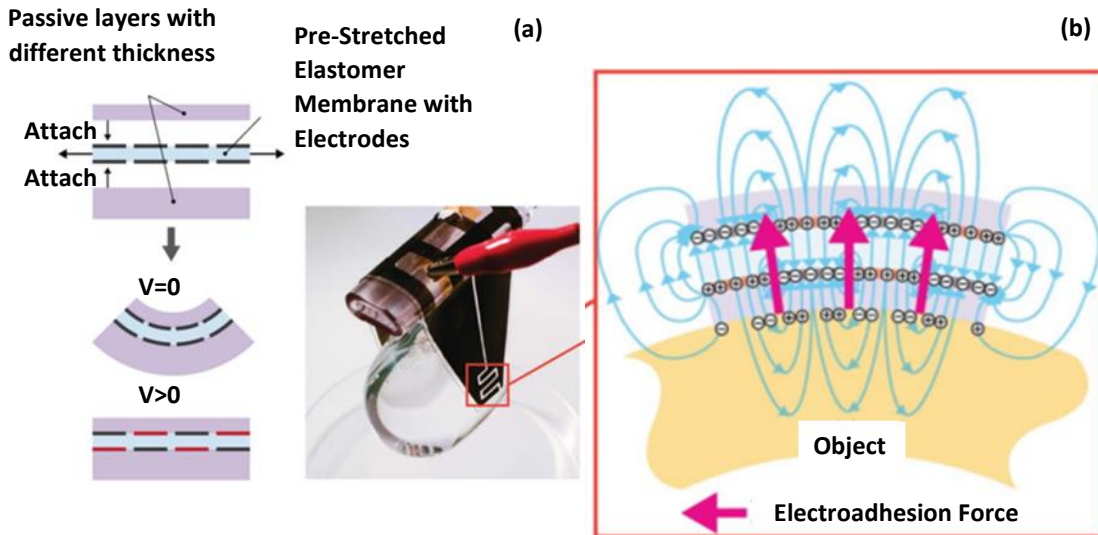


Figure 32 Structure and working of a compliant vertical gripper (a) The DEA part of the gripper consists of pre-stretched DEA bonded to passive layers. At 0 V, the structure is curled up and on applying Voltage across the top and bottom layers, uncurls the DEA to a flat configuration (b) Same voltage is applied between the top and bottom electrodes but these are laterally offset so that there is a high electric field normal to the membrane and strong fringe fields at the boundaries as shown by the arrows. Reproduced from [59]

Their 4-electrode configuration allowed them to selectively tailor either individual electroadhesion or DEA gripping mode or simultaneously activate both. The design flexibility provides a huge scope for modulating forces and bending moments.

2.7. Challenges: Electroadhesion and Electrostriction Devices

The dynamic controllability offered by electric fields has made them attractive for modulating adhesion. While sections 2.3 and 2.4 discuss the scope of engineering electroadhesive and electrostrictive forces, there still exist some challenges that are limiting the application of these technologies.

2.7.1. High operating Voltages

It is observed that adhesive forces and actuation pressures increase with increasing voltage and are only limited by the dielectric breakdown strength of the material. However, in order to adapt these technologies for practical applications and safe operation, there is a constant need for reducing the driving voltages without compromising the output forces and actuation pressures. One of the ways to meet this challenge has been to fabricate thinner dielectric

membranes. Several methods such as pad printing [99], Langmuir blodgett films [28], molecular beam deposition (MBD) [100], have been explored to print films in the micrometre thickness range and the driving voltage has been reduced to a few 100 Volts. By reducing the thickness of the dielectric membranes, the stiffness effect of the deposited electrodes becomes more pronounced. Thus, a balance is needed to ensure mechanical stability of thin films to produce reliable strains at low operational voltages.

Another route to achieve high adhesion stresses at low voltages, is to employ dielectric materials with high permittivity [85][86]. Use of fillers such as TiO_2 , BaTiO_3 and covalent modification of the polymer chains has been investigated. Kim et al. designed a soft nanocomposite electroadhesive (SNE) that operates at 30 V [101]. As shown in Figure 33, the device consists of forests of vertically aligned multiwalled carbon nanotubes (CNTs) grown on conductive electrode TiN, conformally coated by a layer of dielectric Al_2O_3 all in the nm range. Figure 33a shows the measurement, using a colloidal AFM tip, of the forces between the nanocomposite electroadhesive and a spherical 4 μm diameter Pt-coated spherical tip. The fibres show a low intrinsic adhesion which is enhanced more than 100 fold by applying 30 V to the CNTs. The authors demonstrated the micromanipulation of an unpackaged light emitting device (LED) chiplet. Figure 33c shows the map for the object range possible to be picked and placed against a flat surface with a coating of the same material at 30 and 100 V.

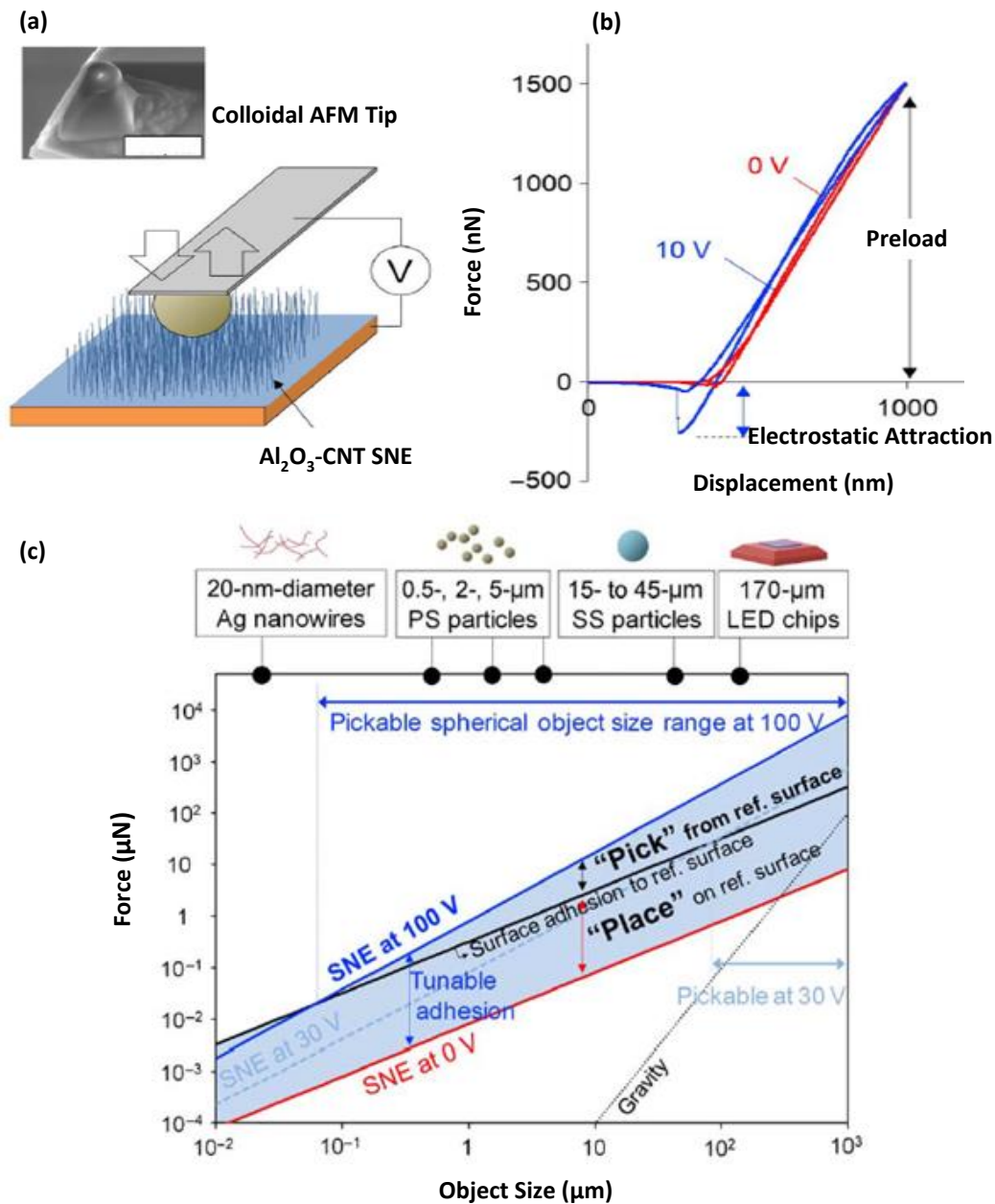


Figure 33 Pick and place of micro-objects using a soft nanocomposite electroadhesive device (a) Schematic of the pull off measurement system using a colloidal AFM having a Pt coated spherical tip. Inset shows the Pt coated tip (b) Force displacement curves without (red) and with (blue) applied voltage (c) A micro pick and place map for the target object range at 30 V and 100 V. Reproduced from [101]

2.7.2. Residual Charges

While such scaling strategies help in achieving low operating voltages, residual charges pose yet another bottleneck for the electroadhesion technology. Polarisation of dielectrics render it

difficult for rapid and complete removal of the residual charges since charges cannot freely migrate in a dielectric. The time taken for these charges to dissipate is a function of the dielectric relaxation time. Different strategies are being directed to overcome these residual charges for easy release of the target materials such as using passage of air jets [102], polarity reverse control [103] and use of resonant vibration of DEAs [98].

2.8. Objective of the thesis

As discussed in Section 2.3, dry adhesives are actively researched in combination with electroadhesives [45][61][60][104]. These studies have been focussed on measuring shear strength as they are targeted at applications such as wall climbing robots [58] and soft grippers [75]. Both the technologies work in vacuum but are sensitive to the environmental conditions, thus requiring controlled environments (humidity and temperature). These studies have also shown that the two technologies are complementary to each other.

With these developments in the field, the objective of the first part of the thesis was to integrate dry adhesives with electrodes to fabricate an electroadhesive and characterize the contribution to normal adhesion by building an inhouse electroadhesion measurement setup. The details are discussed in Chapter 3, where tuning the adhesion of micropatterns by superimposing DC electrical fields was experimentally demonstrated. A theoretical and numerical model was also developed in cooperation with TU Eindhoven to discuss the dependence of electroadhesive forces on applied voltages.

The second part of the thesis focusses on triggering detachment of micropatterned adhesives by inducing shear via Dielectric Elastomeric Actuators. The detachment process is critical for placing the objects during automated assembly. Challenges such as presence of residual charges make it difficult to overcome the existing adhesion between the target substrate and the adhesive pad. Within the scope of this thesis, we discuss a novel method where the uniaxial deformation of DEAs is used to induce shear detachment of the microfibrils. This approach actively engages the microstructure and the details are discussed in Chapter 4.

Chapter 3: Enhancing dry adhesion of polymeric micropatterns by electric fields*

3.1. Abstract

Micropatterned dry adhesives rely mainly on van der Waals interactions. In this paper, we explore the adhesion strength increase that can be achieved by superimposing an electrostatic field through interdigitated subsurface electrodes. Micropatterns were produced by replica molding in silicone. The adhesion forces were characterized systematically by means of experiments and numerical modeling. The force increased with the square of the applied voltage for electric fields up to 800 V. For larger fields, a less-than-quadratic scaling was observed, which is likely due to a small, field-dependent electrical conductivity of the materials involved. The additional adhesion force was found to be up to twice the field-free adhesion. The results suggest an alternative method for the controlled handling of fragile or miniaturized objects.

*This chapter was published in ACS applied materials and interfaces:

Vaishali Chopra, Maciej Chudak, René Hensel, Anton A. Darhuber, Eduard Arzt(2020). Enhancing dry adhesion of polymeric micropatterns by electric fields. ACS Appl. Mater. Interfaces.

The manuscript can be accessed at: DOI: [10.1021/acsami.0c05077](https://doi.org/10.1021/acsami.0c05077)

3.2. Introduction

Temporary adhesive contacts between solid bodies can be achieved using various techniques and promote attractive alternatives to mechanical grippers for continuous automatic handling and assembly. To date, vacuum grippers are widely used in pick-and-place applications with high precision in positioning [105]. Mechanical, magnetic and electromagnetic grippers offer alternatives for specific applications, but are used less frequently. A novel approach is the utilization of micropatterned adhesives [106]–[109]. Their performance relies mainly on van der Waals interactions and contact mechanics, which are controlled by mechanical properties and the proper design and arrangement of the microstructures in the adhesive array [110]–[112].

Pick-and-place applications necessitate a controllable switch between a high (pick) and a low (release) adhesive regime. Several examples of external stimuli for switching adhesion of micropatterned adhesives have been reported, including compressive loads [113], [114], heating [115], [116], magnetic fields [117], [118], pneumatic control [109], [119], and UV exposure [11]. Almost all mentioned strategies require specific designs or material selection, which potentially limit the range of application. In addition, most concepts allow switching between "on" and "off" states, but no specific adjustability to the required adhesion performance.

An approach to control adhesion during operation is electroadhesion. Electro adhesion functions for both conductive and insulating targets [120]–[122] and is, for example, used in semiconductor wafer handling [123] or microhandling [124]. Electro adhesion devices typically make use of interdigitated electrode arrays to maximize the spatial extent of regions with high electric field strength and high field gradients [121]. The traditional electrostatic models predict a dependence of the electro adhesion force on the square of the applied voltage difference [125]. Recently, electro adhesion has been combined with micropatterned adhesives for applications such as wall climbing robots [58] and flexible grippers [126]. Spenko et al. and Menon et al. have successfully demonstrated that the combination of both concepts improves shear adhesion, as the normal force induced by electrical fringe fields forces closer contact with higher friction [45], [127].

The objective of the present paper is to study the influence of superimposed electroadhesion on the normal adhesion of polymeric micropatterns. Details of the experimental setup and the electroadhesion device fabrication will be described in Section 2, the experimental results in Section 3. A description of theoretical models both for electrically insulating and electrically conductive materials will be given in Section 4, followed by an in-depth numerical evaluation of the models and a comparison with the experimental data in Section 5.

3.3. Materials and Methods

3.3.1. Device Fabrication

For the micropatterned electro adhesive device, micropatterned polymeric films were transferred onto interdigitated comb electrodes. The micropatterns consisted of cylindrical pillars with diameter and height of 7 μm (aspect ratio 1:1). The fabrication included three replication steps. In the first step, a lithographically patterned silicon wafer with holes (negative master template) was replicated using polydimethylsiloxane (PDMS, Sylgard 184, Dow Corning, Midland, MI, USA). PDMS was prepared by mixing ten parts of the base material with one part of the curing agent using a speed mixer (DAC600.2 VAC-P, Hauschild Engineering, Hamm, Germany) at 2350 rpm for 3 min. In the second step, a replica structure made of UV-curable perfluoropolyether-dimethacrylate (Fomblin MD40, Solvay, Bollate, Italy) was obtained. The pre-polymer contained 0.5 wt% of a photoinitiator (2-hydroxy-2-methyl-propiophenone, Sigma Aldrich, Taufkirchen, Germany). The mixture was poured over the first PDMS template and covered with a microscope glass slide. The pre-polymer mixture was exposed to UV (wavelength 365 nm, Omnicure S1500, Excelitas Technologies) in a nitrogen atmosphere for 5 min. The cured structure was carefully peeled and served as template (negative) for the fabrication of the micropatterned adhesive films made from polydimethylsiloxane (PDMS, Sylgard 184, Dow Corning, Midland, MI, USA). PDMS was prepared as described above. The mixture was poured over the MD40 template and covered with interdigitated electrodes (IDEAU200, Deutsche METROHM GmbH & Co. KG, Filderstadt, Germany). Prior to this, the electrodes were treated with oxygen plasma for 3 min in order to promote the adhesion of the silicone film to the electrode surface. Electrodes had a width of 220 μm and a gap between oppositely charged electrodes of 160 μm . A fixture was used to clamp the template, the electrodes and the intermediate liquid PDMS layer to set the

desired backing layer thickness of the micropatterned film. The whole setup was placed into an oven, thermally cured at 95 °C for 20 min and finally demolded.

The micropatterned electro adhesive device was fabricated by combining an elastomeric micropatterned film with an interdigitated comb electrode array as shown in Figure 34. The diameter and height of the micropillars were 7 μm . The pillars were arranged hexagonally with a center-to-center distance of 14 μm , which is one order of magnitude smaller compared to the width (220 μm) and distance (160 μm) between the electrodes. The backing layer was 55 ± 5 μm , which is one order of magnitude larger than the pillar height. Thus, we assume that the characteristics of the electrical fringe field were not influenced by the spatial orientation of the pillar array in relation to the direction of the electrodes.

3.3. Electroadhesion Setup

The normal adhesion was characterized using a custom built setup. A spherical glass lens with a curvature radius of 15.5 mm (Edmund Optics GmbH, Mainz, Germany) was used as probe. The probe was mounted to a load cell (KD 34s ME-Meßsysteme, Hennigsdorf, Germany) to measure normal forces. Probe and load cell were displaced using a linear stage (Q-545 Q-Motion, Physik Instrumente GmbH & Co. KG, Karlsruhe, Germany). The micropatterned electro-adhesive device was mounted below the probe and connected to a DC high-voltage power supply (HCN 14-3500, FuG Elektronik GmbH, Schechen, Germany). A LabVIEW program was developed to control the electro-adhesion setup. To reduce residual charges in adhesion measurements in the presence of an electrical field, probe and adhesive film were treated by an antistatic gun upon each measurement (Zerostat 3 Anti-Static, SPI Supplies, Glasgow, UK). All experiments were performed in a laboratory with controlled temperature and relative humidity (RH) at 21 °C and 50 ± 5 %.

During approach, the spherical probe was brought in contact with the adhesive film. At maximum indentation depth, the compressive preload was highest. This position was held for 1 s, before the probe was retracted. In all experiments, approach and retraction velocities were 1 $\mu\text{m/s}$. The displacement of the probe, u , was calculated as follows: $u = u_M - F/k$, where u_M is the displacement of the motorized stage, F is the force and $k = 6.17$ kN/m is the machine stiffness. The absolute value of the maximum adhesive force at detachment was

defined as pull-off force. Pull-off forces were converted into pull-off stresses by dividing them by the projected contact area A_p at maximum compressive preload. The projected contact area was calculated by the geometrical formula $A_p = \pi (R^2 - (R - u_p)^2)$, where $R = 15.5$ mm is the curvature radius of the probe and u_p is the distance from contact to maximum indentation of the probe into the micropatterned film.

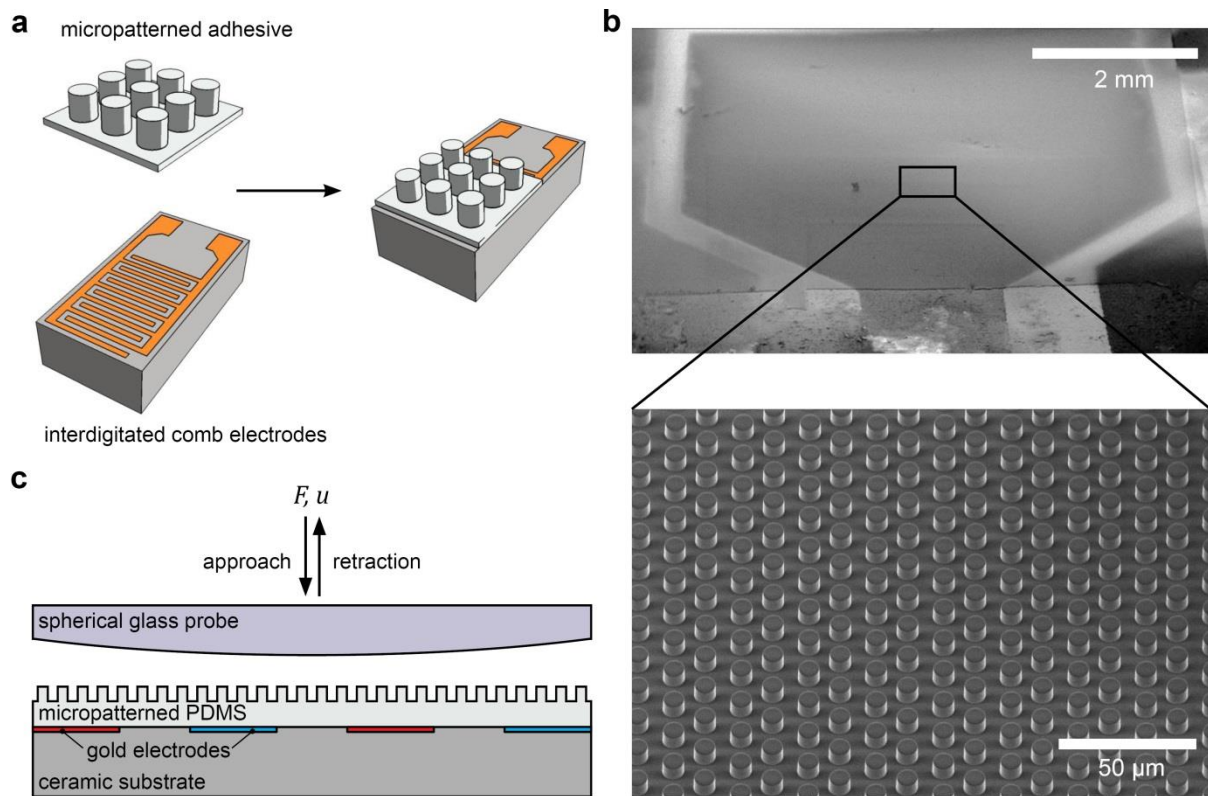


Figure 34 The micropatterned-electro adhesive device. (a) Illustration of the basic set-up. A micropatterned adhesive film was generated via replica molding and, subsequently, deposited on the interdigitated comb electrodes. (b) Schematic of the adhesion test setup. During the test a spherical glass probe was attached (approach) and detached (retraction) at different applied voltages. Normal forces F and displacements u were recorded. (c) Scanning electron micrograph of the micropatterned-electro adhesive device. The inset

3.4. Experimental Methods

Results of adhesion tests for different applied voltages are shown in Figure 35. Figure 35a compares results with (1.8 kV) and without (0 kV) applied electrical field. Without applied field (black curve), the normal force was zero before the probe contacted the micropatterned surface ($u \geq 0$ μm). Contact was established by pressing the probe into the adhesive film

(indentation) up to a preset displacement of $-2.3 \mu\text{m}$. At that position, the maximum compressive preload of 30 mN was achieved. Upon holding for 1 s, the probe was retracted. The probe detached from the surface at a maximum tensile force of -7 mN , i.e. a pull-off force of 7 mN. This pull-off force must be attributed to van der Waals interactions.

In the presence of an electrical field (red curve), the probe already experienced an attractive force before contact (for $u \lesssim 70 \mu\text{m}$). At contact, the attractive force due to the electrical field was -5 mN . The maximum compressive preload reduced apparently to 25 mN for a similar indentation of $-2.3 \mu\text{m}$ in relation to the experiment without electrical field. The attractive electrostatic force further caused earlier contact at $u = 1.1 \mu\text{m}$. This effect is related to the elastically deformable setup with a machine stiffness of 6.17 kN/m and constant motor displacement for all measurements. The pull-off force was 12 mN. Upon detachment, the force gradually decreased with increasing distance between the probe and the adhesive, similar to the approach. The slightly higher attractive force (about 1 mN) during retraction compared to the approach is most likely related to residual charges upon separation of contact.

Figure 35b shows the pull-off force as a function of the net preload (i.e. the sum of the negative, compressive mechanical preload and the positive, attractive electroadhesion) for various applied voltages. The pull-off forces increased with the applied voltage and at 2 kV were twice as high as at 0 kV. With increasing voltage, the net preload decreased for constant displacements due to increasing electrostatic attraction between the adhesive and the probe. Although the probe was spherical, pull-off forces were insensitive to preload, as all measurements were performed in saturation conditions, i.e. pull-off force was insensitive to preload [128]. Figure 35c summarizes the pull-off forces in terms of applied voltages. Pull-off forces and stresses increased with increasing electric fields, which suggests that the electrostatic forces superimpose on the van der Waals forces. Compared to the field-free case, a typical enhancement of adhesion by the factor 2 was achieved at a voltage of 2 kV. It is notable that the adhesion force or stress appeared to increase parabolically, as expected theoretically, only up to about 800 V; above this value an approximately linear relationship with applied voltage was found.

Importantly, the electrostatic force contributed to the contact formation of the probe with the adhesive, which led to a reduced net preload although the displacement from first contact to

maximum indentation was kept constant. Thus, the net preload reduced with increasing voltage as shown in Figure 35d. For small indentations such as $0.9\ \mu\text{m}$, the net preload turned negative for voltages larger than $1.5\ \text{kV}$. Here, the requisite compressive force of the probe to adhere to the surface was realized solely by electrostatic forces without mechanical compression.

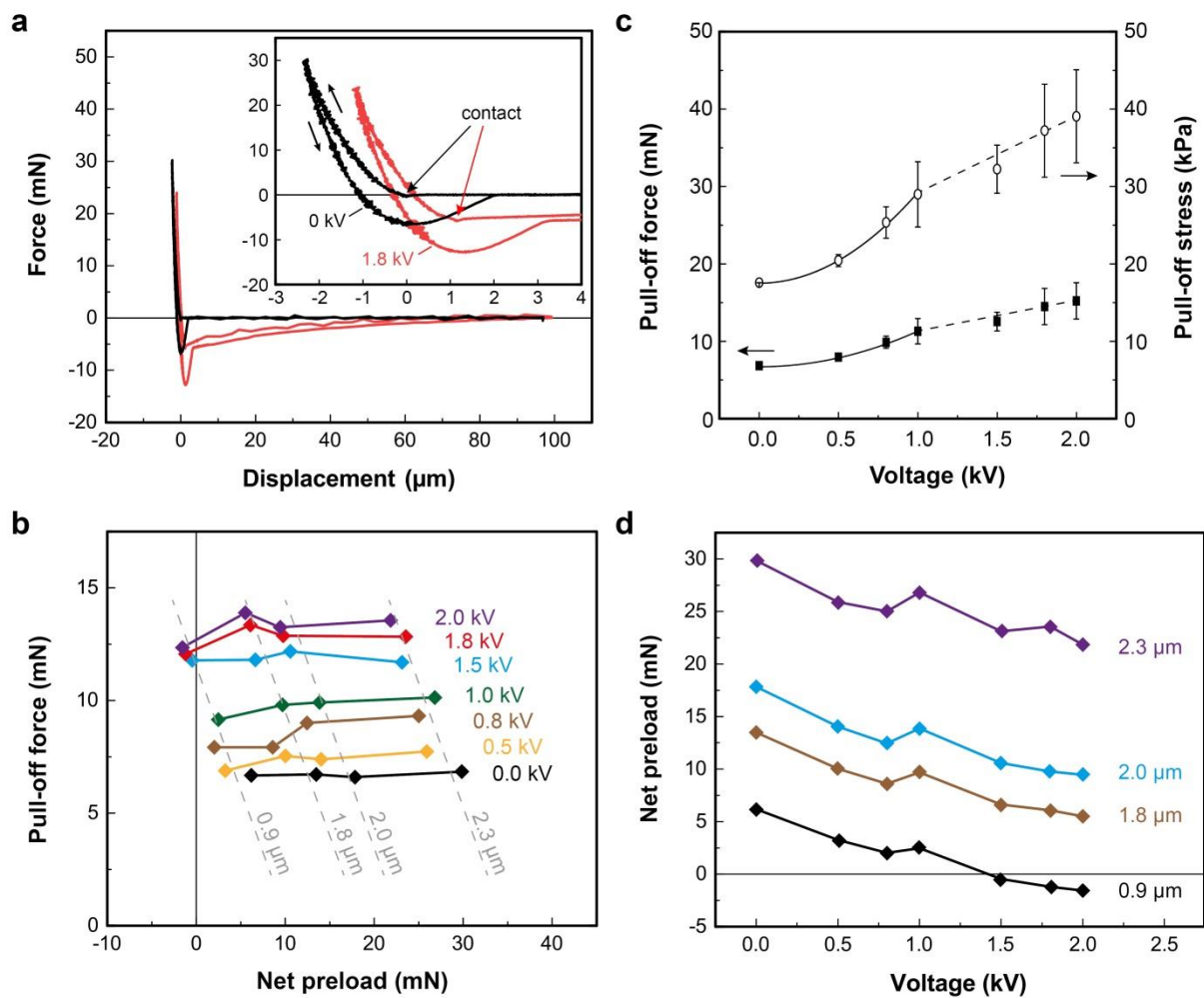


Figure 35 Electroadhesion results. (a) Force-displacement curves for $0\ \text{kV}$ (black) and $1.8\ \text{kV}$ (red). Positive and negative forces are compressive and tensile forces, respectively. The inset presents data close to the contact of the probe with the micropatterned adhesive film. Arrows indicate the path during approach and retraction. (b) Pull-off forces in terms of net preloads for various applied voltages. Dashed lines highlight data for constant indentations. (c) Pull-off force (solid squares) and pull-off stress (open circles) as function of the applied voltage. The solid and the dashed lines illustrate quadratic and linear functions, respectively. (d) Net preload as function of the applied voltage. Numbers present the indentation into the micropatterned adhesive.

3.5. Theoretical Models

The experimental results suggest that the achievable adhesion force was enhanced by a switchable electric field-induced force exerted on the probe. Below we present theoretical models for different types of materials as well as their numerical implementation to predict the steady-state values of the electroadhesion force. The boundary conditions are introduced in section 3.5.6. We used the finite-element software Comsol 5.2.

3.5.1. Electrostatic Interaction – Insulating Materials

We first consider a stationary electrostatic system that is composed of purely dielectric, i.e. electrically insulating, materials. The electric field distribution is governed by Poisson's equation

$$\nabla \cdot (\varepsilon_0 \varepsilon_r \nabla V) = -\rho \tag{3.1}$$

where ε_r is the relative permittivity of the respective material, ε_0 the vacuum permittivity, V the electric potential, and ρ the volume charge density. We assume the dielectric materials to be linear, non-dissipative, isotropic, and homogenous. We assume all material properties to be independent of elastic deformations. Moreover, we assume all surface and volume charge densities to be zero, except at the surface of the electrodes in all simulations pertaining to this section. The electrical potential is continuous at all interfaces, which implies the continuity of the tangential component of the electric field vector. The normal component of the electric field vector is discontinuous at the interface between two materials a and b according to

$$n \cdot (\varepsilon^a E^a - \varepsilon^b E^b) = 0 \tag{3.2}$$

(2)

where n is the unit normal vector of the interface pointing from material a to material b and E is the electric field vector.

3.5.2. Bulk-Conductive Materials

We now consider all materials to have a non-zero electrical bulk conductivity σ . This is motivated by the fact that, in the experiments, the electric field strength is comparable to or even above the dielectric breakdown strength of air of approximately 3 MV/m. At such high electric fields many materials that are normally considered electrically insulating actually behave as weak conductors. This applies to air, the elastomer and possibly also the glass [129]–[131].

Assuming no external currents, we solve the continuity equation in steady state

$$\nabla \cdot J = 0 \tag{2}$$

3. 3

where according to Ohm's law the bulk current density is given by $J = \sigma E$. eq. 3. 3 is equivalent to

$$\nabla \cdot (-\sigma \nabla V) = 0 \tag{3}$$

3. 4

We assume σ to be homogenous in all materials except air, where we consider the conductivity to be dependent on the local electric field, as discussed in section 4.4. The electrical potential is continuous at all interfaces. The normal component of the electric field vector is discontinuous at the interface between two materials a and b according to

$$n \cdot (\sigma^a E^a - \sigma^b E^b) = 0 \tag{5}$$

3. 5

which represents the continuity of the normal component of the bulk current density.

3.5.3. Surface-conductivity of Glass-Air Interfaces

In our experiments, we used glass lenses as probes. The electrical bulk conductivity of glass at room temperature is almost unmeasurably small, i.e. essentially zero [132]. However, there is a significant electrical surface conductivity due to moisture adsorption that must be taken into account [133]–[136].

The surface conductivity is implemented by assuming an ultralow bulk conductivity of the lens (10^{-30} S/m) and an additional interfacial condition at the glass-air interface

$$\mathbf{n} \cdot (\mathbf{J}^{glass} - \mathbf{J}^{air}) = \mathbf{n} \cdot (\sigma^{glass} \mathbf{E}^{glass} - \sigma^{air} \mathbf{E}^{air}) = -\nabla_s \cdot \mathbf{j}_s$$

3. 6

(6)

where ∇_s is the surface gradient operator, \mathbf{n} the unit normal vector of the interface pointing from glass to air [137]–[139]. Eq. 3. 6 represents charge conservation across the glass-air interface and relates a discontinuity in the bulk current density to the surface divergence of the surface current density $\mathbf{j}_s = \sigma_s \nabla_s V$, where σ_s is the surface conductivity. At all other interfaces, eq. 3. 5 holds. The electrical potential is continuous at all interfaces.

3.5.4. Variable Air Conductivity

At very high electric fields approaching the dielectric breakdown limit, the electrical conductivity of air σ_{air} is dependent on the electric field strength. Carlon has measured the electrical conductivity of air at very high relative humidities $RH \geq 66\%$ [140]. It was found that σ_{air} was constant for low fields and increased rapidly for $|E|$ exceeding a certain threshold value E_c . The blue symbols in Figure 3 below are extracted from his measurements for $RH = 66\%$. In this case, E_c is approximately 0.1 MV/m, which is substantially lower than the breakdown strength. He also observed very strong humidity dependence of the low field conductivity. Several groups reported low field conductivities of air between 1 and 100 fS/m, depending on the geographic location, air pollution and atmospheric conditions [129], [130], [141], [142]. Because quantitative measurements of field-dependent conductivity are scarce, we use the following empirical relation:

$$\frac{\sigma_{\text{air}}}{\sigma_0} = 1 + s_L E_0 \log \left[1 + \exp \left(\frac{|E| - E_c}{E_0} \right) \right]$$

3. 7

(7)

where σ_0 is the zero-field air conductivity, E_c is a critical field strength below which conductivity is constant and above which it increases, $E_0 = 0.1 \text{ MV/m}$ defines the width of the transition region and s_L defines the slope. Curves of $\sigma_{\text{air}}(E)$ for different values of E_c and s_L are illustrated in Figure 36. We assume $\sigma_0 = 4 \text{ fS/m}$ as standard laboratory conditions usually correspond to relatively dry air (RH 30 to 40%) [129]. It is seen that the empirical relation gives a smooth transition between the constant and linear regimes.

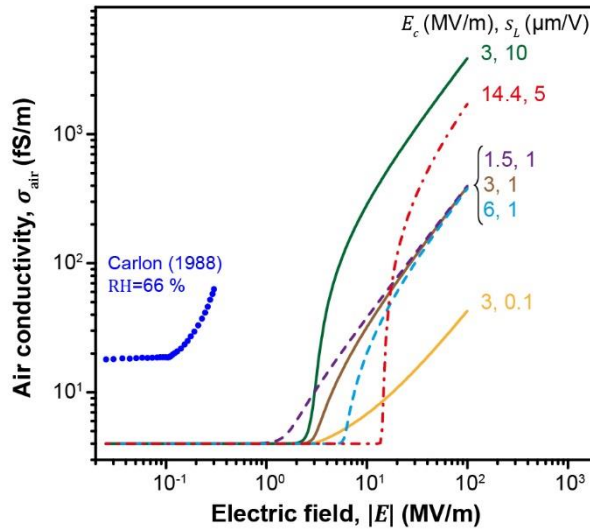


Figure 36 Models for the electric field-dependence of the air conductivity (see eq. 3. 5). Solid lines vary the slope s_L for threshold value $E_c = 3 \text{ MV/m}$, dashed lines vary E_c for $s_L = 1 \text{ } \mu\text{m/V}$. The dash-dotted red line was found to match experimental results with $E_c = 14.4 \text{ MV/m}$ and $s_L = 5 \text{ } \mu\text{m/V}$. Blue symbols are extracted from measurements of Carlton for moist air (RH = 66 %) [140].

3.5.5. Electroadhesion force

The electroadhesion force F_{es} acting on a target object in a non-uniform electric field is derived from the Maxwell stress tensor T_{ij} , given as

$$T_{ij} = D_i E_j - \frac{1}{2} \delta_{ij} \sum_{k=1}^3 D_k E_k$$

3. 8

(8)

where $E_i \equiv -\partial V/\partial x_i$ is the electric field, $D_i \equiv \epsilon_0 \epsilon_r E_i$ is the electric displacement field and δ_{ij} is the Kronecker delta. At a boundary between two materials of different permittivities such as glass and air, the stress tensor T_{ij} is discontinuous, which causes a mechanical force density S_i to act on the boundary

$$S_i = (T_{ij}^{air} - T_{ij}^{glass}) n_j$$

3. 9

(9)

The Maxwell stress vector S_i represents the electromechanical coupling. The total electroadhesion force is calculated by integrating S_z over the surface area A of the lens:

$$F_{es} = \iint S_z dA.$$

3. 10

(10)

3.5.6. Computational domain, boundary conditions and material properties

Figure 37 shows the model geometry. A glass lens is positioned above the electrode array. The width and length of the electrode array is $w_a = 2b(n - 1) + 2a$ with n interdigitated stripe electrodes of width $2a$ and period $2b$ (Figure 37a). The electrode array is deposited on a ceramic substrate with thickness $h_c = 3$ mm, relative permittivity $\epsilon_r = 10$ and conductivity $\sigma = 100$ fS/m. The array is covered with an elastomer layer of thickness $h_e = 55$ μ m, relative permittivity $\epsilon_e = 2.5$ and conductivity $\sigma_e = 25$ fS/m. The elastomer is covered with a

hexagonal array of cylindrical micropillars. As the pillars are too small to be considered individually, we use an effective medium approximation. The effective medium has a thickness equal to the pillar height $h_p = 7 \mu\text{m}$. Its permittivity and conductance are derived from that of the elastomer and air, equal $\varphi\epsilon_e + (1 - \varphi)\epsilon_{\text{air}} \approx 1.34$ and $\varphi\sigma_e + (1 - \varphi)\sigma_{\text{air}} \approx 8.76 \text{ fS/m}$, where $\varphi = \frac{\pi\sqrt{3}}{6} \left(\frac{2r_p}{s_p}\right)^2 \approx 0.227$ is the pillar array volume filling ratio, $r_p = 3.5 \mu\text{m}$ is the pillar radius and $s_p = 14 \mu\text{m}$ the spacing of the pillars. The glass lens has a relative permittivity $\epsilon_L = 5$, conductivity $\sigma_L = 1 \text{ pS/m}$, radius of curvature $r_L = 15.5 \text{ mm}$, diameter $2a_L = 16 \text{ mm}$, thickness $h_L = 4 \text{ mm}$ and is placed $\delta = 1 \mu\text{m}$ (unless specified otherwise) above the pattern. Air is assumed to have a relative permittivity of 1 and conductivity $\sigma_{\text{air}} = 4 \text{ fS/m}$ at zero field strength. All geometric and material parameters are summarized in Table 1.

Due to symmetry we only consider a cuboidal quarter of the system with width $x_m = 20 \text{ mm}$, length $y_m = 20 \text{ mm}$ and height $z_m = 40 \text{ mm}$. The glass lens is positioned above the electrode array (Figure 37b). A quarter of the electrode array has width and length $\frac{w_a}{2} = 3 \text{ mm}$ and is composed of $n = 8$ electrodes of width $2a = 220 \mu\text{m}$ and period $2b = 380 \mu\text{m}$. At $y = 0$ there is a symmetry plane where $n \cdot E = 0$ and $n \cdot J = 0$ hold. At $x = 0$, there is an antisymmetry plane where $V = 0$ holds. All other external boundaries are also considered to be symmetry planes and positioned distant enough (i.e. $x_m, y_m, z_m \gg \frac{w_a}{2}$) to have no influence on the solution.

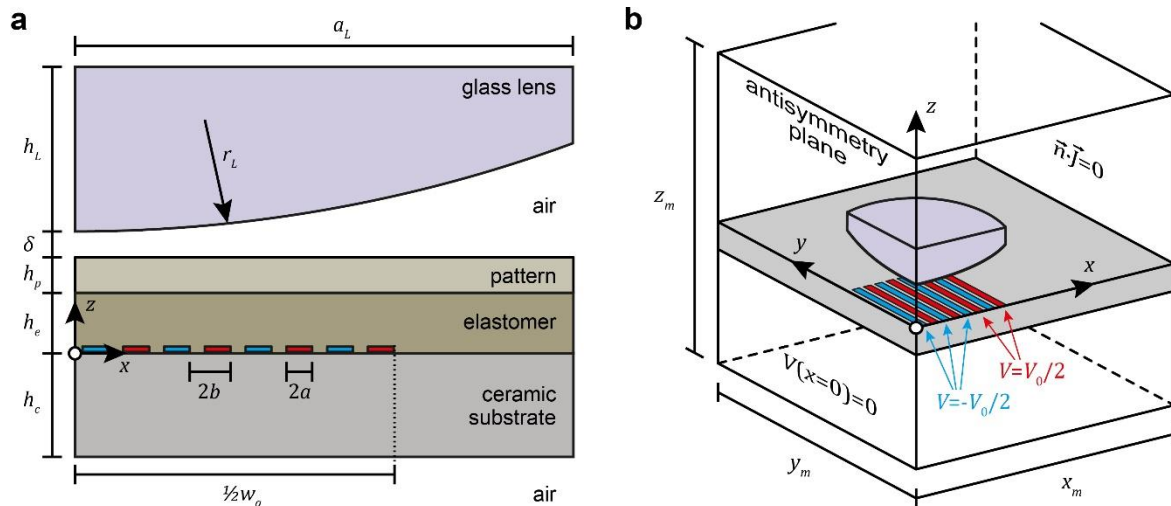


Figure 37 Schematic illustration of the computational model. (a) Cross-section ($y = 0$ plane) of the glass lens (purple, curvature radius r_L) placed above oppositely charged electrodes (red

and blue stripes) located on a ceramic substrate (grey). The electrode array is covered with a thin elastomer layer with thickness h_e . The patterned surface is approximated by a thin homogenous effective medium layer with thickness h_p . (b) In the simulations, a cuboidal quarter of the experimental setup is considered, with a symmetry plane at $\mathbf{y} = \mathbf{0}$ and an antisymmetry plane at $\mathbf{x} = \mathbf{0}$.

Table 1. List of variables as well as geometric and material parameters used in the numerical simulations.

Material	Property	Symbol	Value	Unit	Reference
Air	relative permittivity	ϵ_{air}	1	–	–
	conductivity	σ_{air}	$4 \cdot 10^{-15}$	S/m	[129]
	gap thickness	δ	10^{-6}	m	–
Lens	relative permittivity	ϵ_L	5	–	[143]
	conductivity	σ_L	10^{-12}	S/m	–
	surface conductivity	σ_s	$10^{-13} \dots 10^{-8}$	S	[144], [145]
	radius	a_L	$8 \cdot 10^{-3}$	m	–
	radius of curvature	r_L	0.0155	m	–
	thickness	h_L	$4 \cdot 10^{-3}$	m	–
Pattern	pillar radius	r_p	$3.5 \cdot 10^{-6}$	m	–
	pillar height	h_p	$7 \cdot 10^{-6}$	m	–
	pillar spacing	s_p	$1.4 \cdot 10^{-5}$	m	–
Elastomer	relative permittivity	ϵ_e	2.5	–	[146]
	conductivity	σ_e	$2.5 \cdot 10^{-14}$	S/m	[146]
	thickness	h_e	$5.5 \cdot 10^{-5}$	m	–
Electrode array	electrode half-width	a	$1.1 \cdot 10^{-4}$	m	–
	half-period	b	$1.9 \cdot 10^{-4}$	m	–
	number of electrodes	n	16	–	–
	applied voltage	V_0	2000	V	–

Ceramic substrate	relative permittivity	ε_c	10	–	[147]
	conductivity	σ_c	10^{-13}	S/m	[148]
	thickness	h_c	$3 \cdot 10^{-3}$	m	–
Computational domain	width, length	x_m, y_m	0.02	m	–
	height	z_m	0.04	m	–

3.6. Numerical results

Figure 38 shows an example of the Maxwell stress distribution $|S_z|$ on the lower surface of the lens. Faint white lines indicate the position of the electrode array. Most of the attraction is concentrated directly above each electrode and near the center of the lens being located $1 \mu\text{m}$ above the micropatterned adhesive. The outermost electrodes exhibit a weak long-range attraction due to fringe fields.

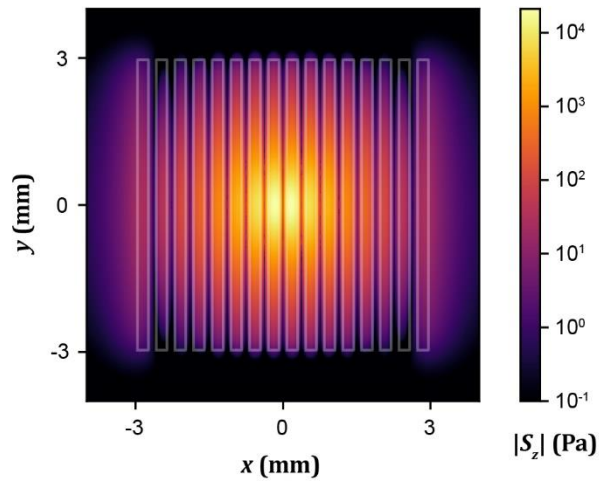


Figure 38 Distribution of electroadhesion: Logarithmic Maxwell stress map on the surface of the lens located $1 \mu\text{m}$ above the micropatterned electro-adhesive device. The white lines indicate the shape and location of the electrode array.

Figure 39 shows the extracted electroadhesion force F_{es} acting on the lens in terms of the applied voltage, as evaluated using eq. 3. 10. The black circles represent our experimental measurements. The dashed and dash-dotted black lines, both scaling as $F_{es} \sim V_0^2$, correspond to a constant air conductivity and the electrostatic model for insulating materials, respectively. It matches the experimental data well up to 800 V. Above that voltage the experiments no longer

follow the quadratic force-voltage dependence predicted by this model. Other symbols in Figure 39 correspond to a field-dependent air conductivity according to eq. 3. 7. The electroadhesion force is proportional to V_0^2 for low voltages, but exhibits a weaker scaling when $E > E_c$. The best fit is obtained for parameter values $E_c = 14.4$ MV/m and $s_L = 5$ $\mu\text{m}/\text{V}$ (red line). A comparison of the data for $E_c = 3$ MV/m and $s_L = 0.1$ and 10 $\mu\text{m}/\text{V}$ (orange and blue lines) illustrate that larger value of s_L induces a weaker dependence of F_{es} on V_0 for $E \gg E_c$. Variations of E_c (green and violet lines) determine at which voltage level the deviation from the square scaling occurs.

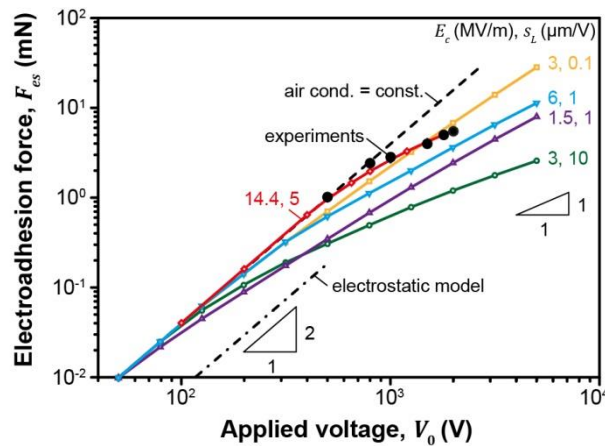


Figure 39 Numerical results of electroadhesion force as function of applied voltage: The variable air conductivity was calculated according to eq. 3. 5 with threshold value E_c and slope s_L (compare Figure 36). Black circles represent experimental results. The dashed black line assumes constant air conductivity. The dash-dotted black line corresponds to the electrostatic model.

A comparison of the models introduced in section 4 and specifically the effect of air conductivity and electric parameters are shown in Figure 40. First, the influence of the field-independent surface conductivity of the lens, σ_s , (blue crosses) and the field-independent bulk conductivity of the lens, σ_L , (orange diamonds) on the electroadhesion force F_{es} is displayed in Figure 40a. In both cases, F_{es} increases for a more conductive lens. It approaches a constant value for large σ_L , because the lens behaves as a perfect conductor and the interior electric field vanishes. Similarly, in the limit of small σ_L , the force approaches a constant value, as the lens becomes a perfect insulator. The force changes sign, because better conductors than air tend to be attracted to and poorer conductors than air repelled from regions with high electric fields.

We conclude that the two models give virtually identical results, if the value of σ_s is chosen as $\sigma_s = \lambda\sigma_L$, where $\lambda \approx 122 \mu\text{m}$ for our system. The line represents a fit based on the function

$$F_{es}(\sigma) = c_0 + \frac{c_1}{1 + \frac{c_2}{\sigma}}$$

3. 11

(11)

where c_0 , c_1 and c_2 are fit parameters. The dashed vertical line corresponds to the (field-independent) air conductivity σ_{air} . When $\sigma_L = \sigma_{\text{air}}$, the force crosses zero. For lower computational cost, the bulk conductivity model was chosen in further calculations, although the surface conductivity model was more physically relevant.

In Figure 40b, we show the dependence of F_{es} on the (field-independent) conductivity of air, σ_{air} , (red points) and of the elastomer, σ_e , (violet squares). F_{es} decreases with increasing σ_{air} . Consequently, if σ_{air} increases with field strength, the force will be lower. F_{es} substantially increases with increasing σ_e , because the high-field region extends closer to the air-lens interface. This can provide an additional parameter for tuning the performance of electroadhesion devices. F_{es} approaches zero in the limits of $\sigma_{\text{air}} \gg \sigma_e$, because large air conductivity prevents any appreciable electric field strength from reaching the air-lens interface. For the same reason, F_{es} approaches zero in the limit $\sigma_e \rightarrow 0$. Figure 40c displays the increase of F_{es} with increasing relative permittivities of the lens, ϵ_L , and the elastomer, ϵ_e , for purely dielectric materials. The electroadhesion force scales linearly with $\epsilon_L - 1$ for small ϵ_L and approaches a constant value for large ϵ_L . A scaling argument explaining these limiting behaviors is presented in section S5 in the Supporting Information. Figure 40d shows F_{es} as a function of the entire electrode array width and length w_a while keeping the number of electrodes and the ratio a/b constant. The electroadhesion force increases with larger w_a . For $w_a > 5 \text{ mm}$, the force approaches saturation as the array is much larger than the region of low separation and high attraction due to the curvature of the lens (compare Figure 38). Figure 40e illustrates how F_{es} varies with elastomer thickness h_e . For a large thickness, this relation is exponential as illustrated by exponential fits (solid lines), because the potential due to coplanar interdigitated electrode arrays decays exponentially in the direction normal to the

substrate.[149] For small separation the extracted force is higher than the long-range exponential fit. The dependence of the force on electrode width-period ratio a/b is given in section S1 in the Supporting Information.

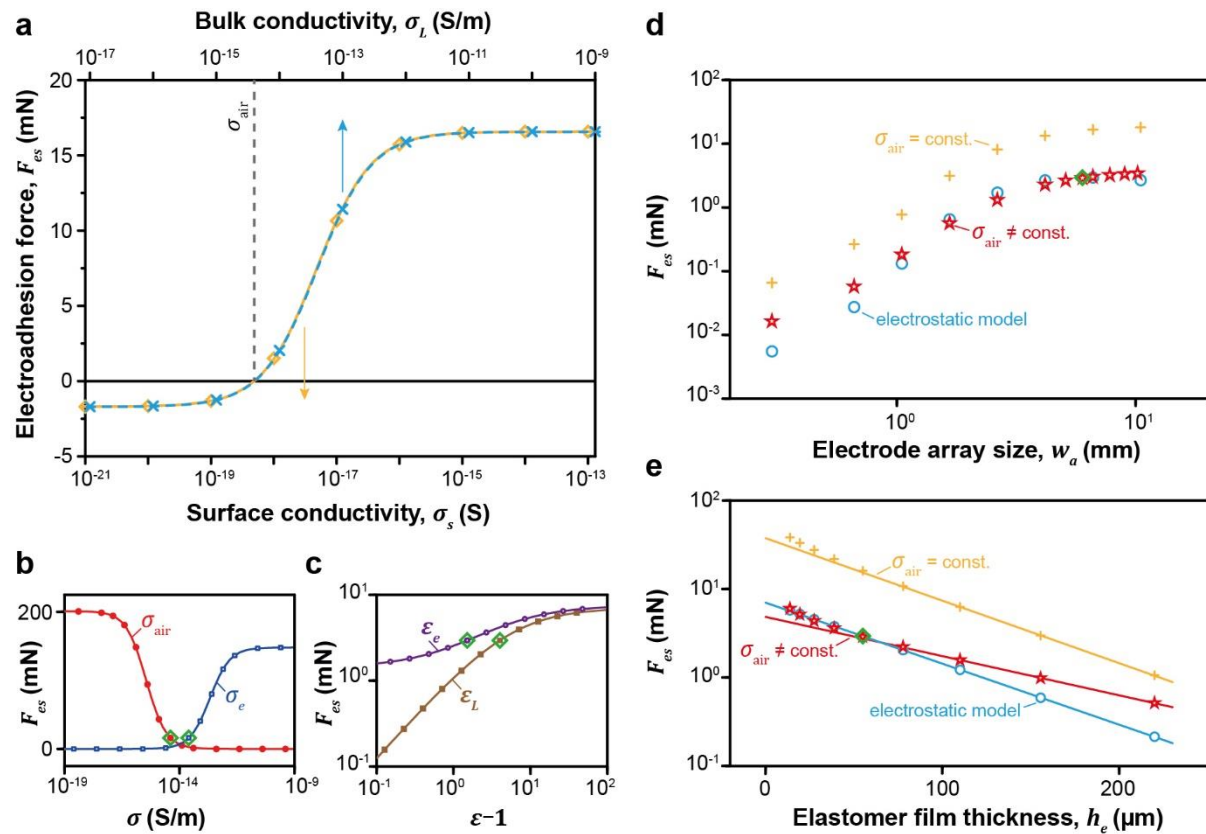


Figure 40 Comparison of numerical models, effect of air conductivity and of electric parameters on electroadhesive force F_{es} . (a) Comparison of the surface and bulk conductivity models: F_{es} in terms of the field-independent surface (σ_s , blue crosses) or bulk (σ , red circles) conductivity of the lens. Solid blue and red dashed lines are fits based on the logistic function, compare eq. 3.11 In the bulk conductivity model, the fitted function crosses zero force for a lens conductivity equal to that of air (dashed grey line). (b) Electroadhesive force as a function of air conductivity (σ_{air} , red circles) and elastomer conductivity (σ_e , blue squares). (c) Electroadhesive force as a function of lens permittivity (ϵ_L , brown squares) and elastomer permittivity (ϵ_e , violet circles). (d,e) Electroadhesive force in terms of (d) the size of the electrode array w_a and (e) the thickness of the elastomer film h_e for linearly varying air conductivity (red stars, $E_c = 3 \text{ MV/m}$ and $s_L = 1 \mu\text{m/V}$), field-independent air conductivity (orange pluses) and in the electrostatic model (blue circles). The lines in (e) represent exponential fits to the three thickest films of each data set. As a reference, the green diamonds in (b-e) represent the parameter values stated in Table 1.

3.7. Discussion

We have fabricated and evaluated a micropatterned electroadhesion device based on an interdigitated electrode and a polymer micropillar array. Attractive forces before and after contact were caused by long-range electrostatic forces, while during contact the short-range van der Waals forces additionally contribute to adhesion. The traditional theoretical models for electroadhesion consider purely dielectric materials, i.e. electrical insulators, for which the electroadhesion force scales quadratically with applied voltage. This is in contrast to our experimental results as well as previous ones reported in literature [150]–[152], where a weaker force-voltage scaling has been observed for voltages above 800 V. We have shown that accounting for minute but finite electric field-dependent electrical conductivities of air and the solid materials used in the device can quantitatively reproduce the experimental results.

The conductivities of the typical materials involved in an electroadhesion device can vary vastly. The surface conductivity of glass can change by seven orders of magnitude depending on the relative humidity and is sensitive to surface contamination e.g. due to fingerprints or residues upon repeated attachment and detachment cycles [153]. The bulk conductivity of polymers can vary strongly depending on impurity concentrations and production methods. Moreover, the conductivity of air depends on the relative humidity and the geographic microlocation of the measurement. Guo et al. reported a drop in electroadhesion force exerted on a glass target substrate by approximately a factor of 3 over the course of 3 days when the relative humidity decreased from approximately 64% to 43% [121]. This is qualitatively consistent with the variation observed in Figure 40a. These results and considerations point at the need for tightly controlled environmental parameters to achieve a stable and reproducible electroadhesion performance.

In terms of potential applications, the findings of this study offer an opportunity for novel pick-and-place devices: by combining the adhesion of a micropatterned polymer with electrostatic interaction, very fragile objects could be handled without applying mechanical compression. Electric fields could also be used to enhance adhesion to objects with rough surfaces, where van der Waals interactions are insufficient[122].

3.8. Conclusions

Our experimental and numerical approach successfully revealed how short-range van der Waals interactions can be superimposed by long-range electrostatic forces, which enables in-line regulation of preload and adhesion forces. The following conclusions can be drawn:

The presence of electrostatic fields enhances adhesion. Compared to the field-free case, an enhancement of adhesion by about a factor 2 (at a voltage of 2kV) was achieved.

Up to 800 V, the adhesion force scaled with the square of the applied voltage. For voltages larger 800 V, the scaling was weaker; this effect is very likely due to a small, field-dependent electrical conductivity of the materials involved.

Numerical results were similar for bulk-conductive materials and a model presuming surface-conductivity of glass-air interfaces. The latter has physical relevance due to possible adsorbed water films or residues through repeated adherence and detachment cycles.

The electrical adhesive force could be further increased by decreasing the thickness of the micropatterned polymer or by increasing the permittivity and conductivity of the elastomer material. Numerical results also indicate that the electroadhesive force is highly sensitive to the environmental conditions; in particular, the force is predicted to decrease with increasing air conductivity, which is directly related to humidity.

3.8. Supporting Information

The dependence of the electroadhesion force on the a/b ratio, the model validation for flat surfaces, the validation of the effective medium approximation, the comparison between idealized and realistic geometries of the electrode array, and the scaling of Maxwell traction for purely dielectric materials are supplied in appendix.

Chapter 4: Shear induced Peeling of Polymeric Micropillars using Dielectric Elastomeric Actuators

4.1. Abstract

Controlled release of micropatterned adhesives is challenging due to strong Van der Waals adhesion with the target object. We report a novel method for shear induced peel detachment in micropatterns combined with a membrane dielectric elastomeric actuator (DEA). An electrical bias of 1.2 kV translates to a lateral displacement of 127 μm and leads to crack initiation, crack growth and finally detachment within 5 seconds. A single large micropillar made of Sylgard 184, with cap diameter 710 μm and length 1600 μm , was used to study the detachment mechanism by in-situ optical visualisation. The detachment process from a glass plate always proceeded via an edge crack which is favourable for release mechanisms in comparison to the center cracks. The study points to the feasibility of controlled detachment of micropillar arrays by DEA.

4.2. Introduction

Bioinspired micropatterned adhesives are investigated for diverse applications such as climbing robots, pick and place systems and medical adhesives owing to their reversible and residue free adhesion. The last decade has seen tremendous progress in achieving high adhesion from polymeric micropatterns via different combinations of materials [32] and designs [154] [155] Presently the focus is shifting not only on achieving strong adhesion ($\sim\text{MPa}$) with diverse target substrates, but equally on facile detachment for precise handling and placement. Shape memory alloys [64], shape memory polymers [116] pneumatic switches [156], magnetic stimulus [10] and mechanical buckling [69] so far have been some of the attractive routes for switching adhesion between adhesive and non-adhesive states. Most of these mechanisms place additional requirements in terms of the material properties and some have relatively slow

response times. Of these existing methods, mechanical buckling exploits elastic instabilities in high aspect ratio structures [69], essentially, by applying a mechanical preload. The principle has been applied, for example, in double sided adhesives [114]. Buckling of high aspect-ratio structures results in a non-adhesive state desirable for release. There are two major limitations to this approach: firstly, a higher compressive load to achieve bending of the pillars can damage fragile target substrates and, secondly, the buckling process is random which poses challenges for precise handling. Hossfeld, Craig K., et al. studied the shear detachment of micropatterned adhesives. Peel testing was carried out by applying shear at different angles ranging from 0 to 30 degrees [157]. Shear was applied by using a custom-built constant angle peel test set-up.

In this chapter, we aim to explore the functionality of in-plane actuation of a dielectric elastomeric actuator (DEA) as a release mechanism, which leads to shear induced peeling of the micropatterned adhesives. Dielectric elastomeric actuator technology has gained interest in the field of soft robotics [63], particularly, as it is possible to attain local deformations tuneable by applied electric fields without the need of complex control mechanisms. In order to understand the underlying mechanism by in-situ visualisation, a mushroom structure with an aspect-ratio of 4 (stalk diameter 400 μm) was combined with a DEA. The fabrication process of the adhesive microstructure as well as the working principle of a DEA are discussed in Sections 4.3 and 4.4 respectively. This is followed by the description of the experimental set-up and methodology in Section 4.5 and 4.6. Section 4.7 provides an in-depth analysis of the detachment mechanism from the optical images and adhesion tests.

4.3. Materials and Methods

An elastomeric mushroom pillar of aspect-ratio 4, stalk diameter of 400 μm and height 1600 μm was used for this study. It was fabricated using replica molding from a micromachined aluminium mold, which consisted of 2 parts. The first part included the micromachined mushroom caps (with holes) and the second part acted as a lid. Fastening the lid after filling the prepolymer and curing agent resulted in a backing layer thickness of 2 mm. The cap diameter was 710 μm . To facilitate demolding, the aluminium mold was initially silanised in a vapor phase deposition process for 30 min, by using 50 μL of (1H,1H,2H,2H-perfluorooctyl) trichlorosilane (AB111444, ABCR, Karlsruhe, Germany). In a next step, polydimethylsiloxane (PDMS, Sylgard 184, Dow Corning, Midland, MI, USA) prepolymer and crosslinker were

mixed in a ratio of 10:1 using a speed mixer (DAC600.2 VAC-P, Hauschild Engineering, Hamm, Germany) at 2350 rpm for 3 min. In order to improve the imaging contrast, 10 wt % of blue pigment (PK 5091, Degussa, Essen Germany) was added to obtain a blue polymeric blend. The micromachined holes in the mold were meanwhile sealed with a polyethylene terephthalate laminating film Sigma 1 (SIG GmbH, Duesseldorf, Germany) to create a flat surface for the mushroom cap [158]. The mold was partially filled with the blue polymer blend and degassed using a vacuum oven (Mettert VO200, Schwabach, Germany) at 1 mbar for 10 min. After expulsion of air bubbles, the mold was filled completely and the lid was fastened. The entire assembly was cured in an oven at 75° C for 2 hours. After curing, the mushroom pillar was carefully demolded.

4.4. Dielectric Elastomeric Actuator

Dielectric elastomeric actuators are transducers that are capable of voltage tunable mechanical deformation. They are composed of a sandwich of dielectric layer in between conformal electrodes. Application of the bias across the dielectric film, results in attraction of the oppositely charged electrodes leading to thickness reduction of the film. Since the film is incompressible (Poisson's ratio $\nu = 0.5$), the film expands in area in order to maintain constant volume [74]. This is the scenario for an unconstrained elastomeric membrane that results in bidirectional actuation. However, in the interest of diverse applications, new strategies are explored to constrain the movement of DEA along a specific direction. To ensure unidirectional lateral displacement, Huang, Jiangshui, et al. incorporated stiff fibres in the DEA membrane. This resulted in unidirectional motion which could further be implemented in the form of a soft gripper [159], [160]. One of the other techniques to achieve unidirectional actuation is by constraining and pre-stretching the dielectric membrane within a rigid frame. In the present study, a dielectric actuator designed by Artificial Muscle Inc. was used [161]. The in-plane actuation of the DEA was leveraged in a haptic module designed for mobile handsets.

The DEA design and working principle is shown in Figure 41. The DEA consisted of 3 periodic sections supported on a rigid frame [161], as shown in the top view of Figure 41a. Each periodic section consisted of movable bars (black), electrodes (green and blue) and a sandwiched layer of dielectric (grey-textured pattern). These sections were separated by rigid dividers (grey colour) which are connected to the outer frame. The DEA was comprised of different sections

of electrodes (I-VI) with alternate sections shown in blue and green. The mushroom pillar was glued on the central movable bar, as indicated by a red dot in Figure 41a (top view). This can also be seen in the cross-sectional view in Figure 41b, which shows the dielectric layer sandwiched between top and bottom electrodes. The top electrodes of the sections were alternately grounded (labelled as GND) and alternately connected to high voltage (labelled as V_1). The bottom electrodes of all the sections were connected to a common output wire V_2 .

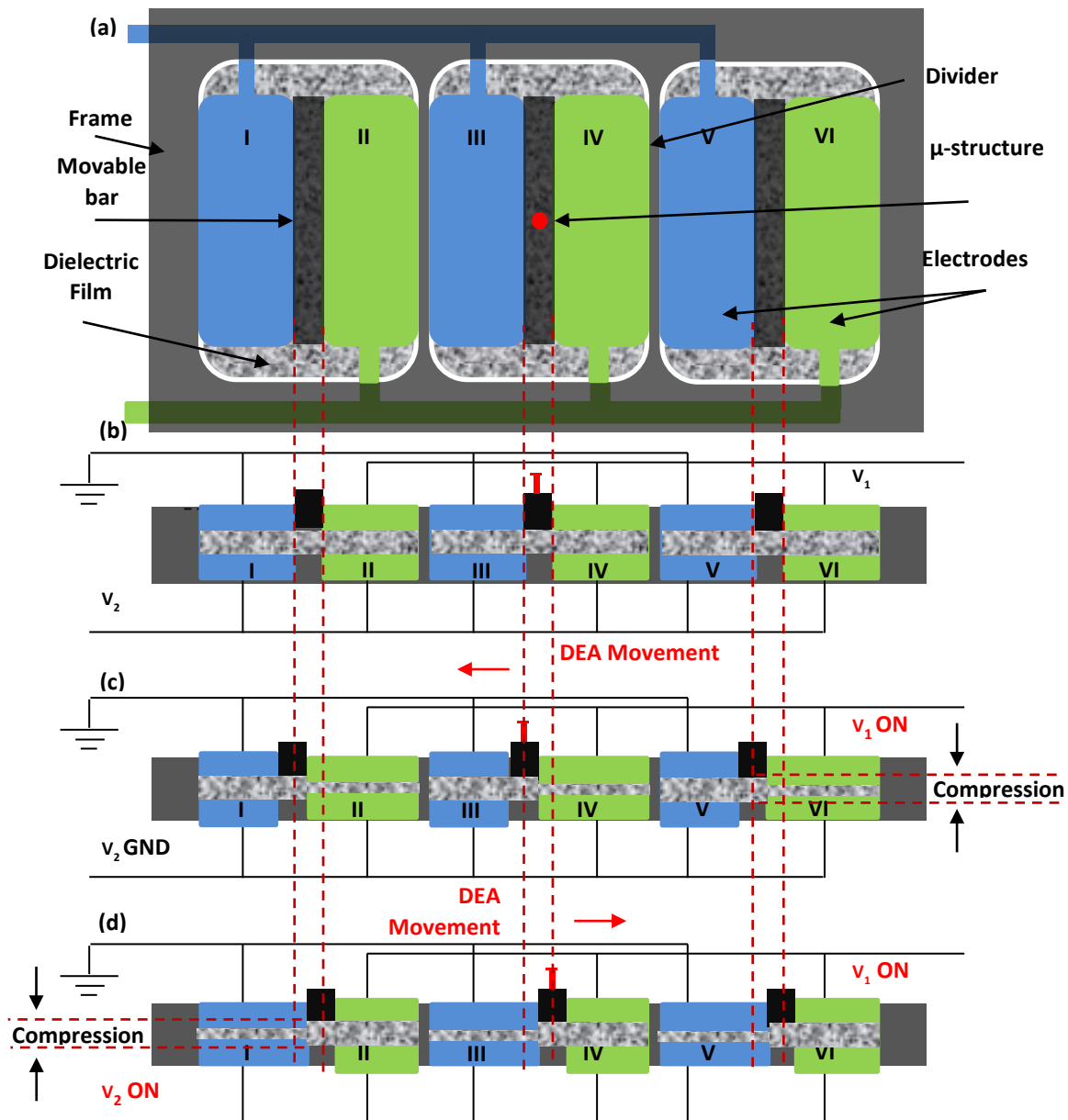


Figure 41 DEA design and working principle: (a) Top view of the linear actuator. Top and bottom electrodes are shown in green and blue sections. Red dot marks the micropillar with mushroom tip. (b) Cross-section view of an unbiased DEA-micropillar assembly. (c) V_1 is

biased causing the green sections II, IV and VI to compress in the thickness direction. Net movement to the left as shown by the direction of the arrow. (d) Biasing the electrode V₂ and V₁ (V₂ = V₁) results in compression of the blue sections I, III and V and net displacement occurs towards the right.

Figure 41 (b-d) explain the unidirectional movement of the DEA resulting from selective biasing of the electrodes V₁ and V₂. When a high potential is applied at V₁ (Figure 41c), while V₂ is also grounded, it leads to compression of the dielectric film in sections, II, IV and VI (highlighted in green). The film tends to expand in both directions, owing to its incompressible nature, however the rigid divider attached to the frame restricts the movement and guides the net movement of the bar and the micropillar unidirectional to the left. Similarly as seen in Figure 41d, upon applying equal potentials to V₁ and V₂, sections I, III and V (shown in blue) are compressed along the thickness direction and the presence of rigid divider leads to a net displacement to the right. Furthermore, the higher the applied voltage, the higher is the lateral displacement. Therefore, in addition to the voltage dependent deformation, the number of segments and footprint of the device could also be tailored to meet the requirements of the desired final application. This highlights the degree of flexibility in design of these actuators.

4.5. Experimental Setup

The DEA-microstructure device was characterized using a custom-built adhesion setup as shown in Figure 42. The outer frame of the DEA was firmly attached to a rigid stage and the pillar with the mushroom cap facing upwards. The stage was connected to a dual axis goniometer (GN L10, Thorlabs, Ann Arbor, Michigan, United States) to ensure complete alignment of the mushroom structure with respect to a flat glass, which was used as the target substrate for measuring adhesion. The target was connected to a load cell (KD 45 2N, ME-Meßsysteme, Hennigsdorf, Germany) which was mounted on a linear drive. An optical camera (Imaging Source DMK 33UX252, Bremen, Germany) fitted with a zoom system to obtain high magnification images of the contact (12x zoom lens Navitar, New York, USA) was mounted on the same linear drive orthogonal to the lateral displacement of the DEA, in order to enable a view through the target glass substrate. This allowed visualization of the contact and peeling events of the microstructure in top view. Another small zoom camera (Imaging Source DMK 23U445, Bremen, Germany) was mounted in the plane of the DEA movement and captured the overall displacement of the DEA and the micropillar. A LABVIEW program was written to

control the displacement of the target substrate for adhesion measurements and to record the measured force-displacement and force-time data. The DEA was biased using a High voltage DC power supply (FuG Elektronik HCN 7E 20 kV, Schechen, Germany).

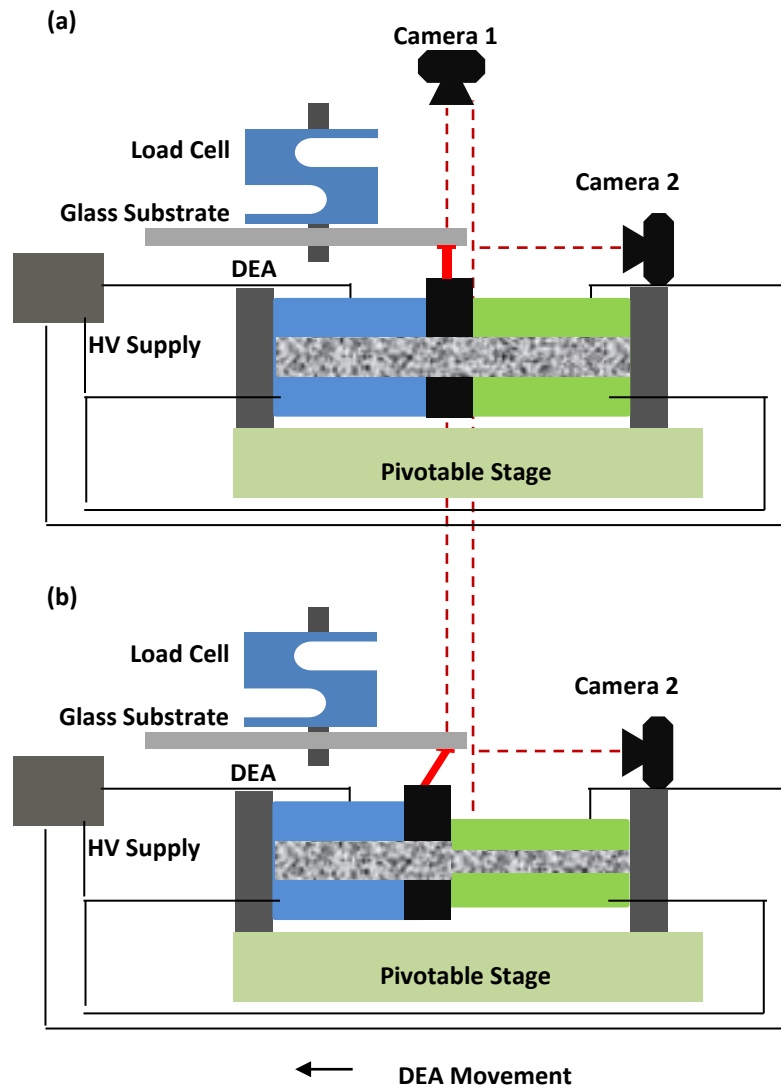


Figure 42 Schematic of the experimental setup for studying the detachment mechanism. Cross-section view depicts a section of the DEA with the micropillar attached to the central movable bar. Glass substrate connected to a linear stage is brought in contact with micropillar and a preload is applied. The substrate is retracted to the touch point, followed by switching on the DEA (biasing the green electrodes). In this image, the fibril gets sheared to the left resulting in a peel front at top right edge.

4.6. Adhesion Measurements

The DEA was characterized systematically at different biasing voltages and the lateral displacement was recorded optically. These measurements were repeated and compared after the microstructure was glued on the DEA. It was observed that the net lateral displacement of the DEA is measured to be 52 μm at 800 V and 127 μm at 1.2 kV (red curve) with the microstructure.

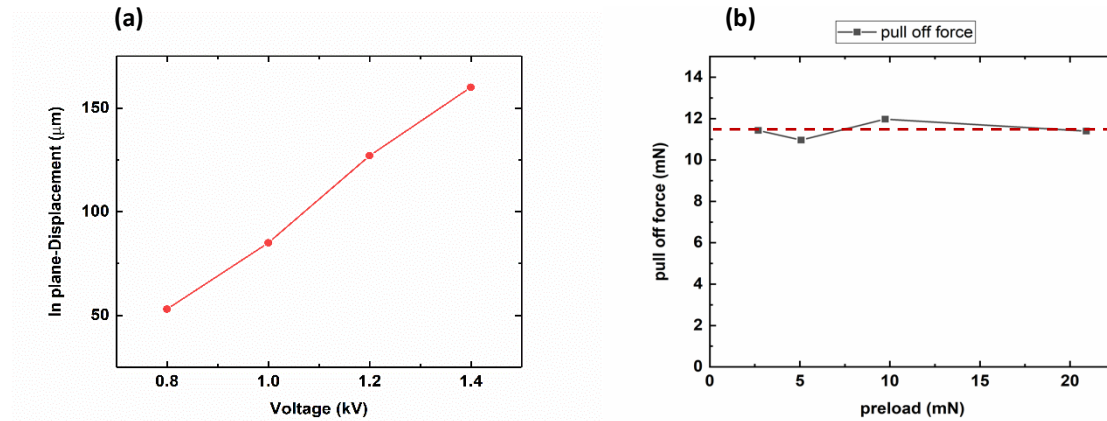


Figure 43: Control experiments (a) Characterisation of the DEA with the microstructure (red curve) showing the voltage dependent in-plane displacement. (b) Pull off force is independent of the applied preload.

Prior to the adhesion tests, the alignment between the target substrate and the micropillar was adjusted using the goniometer. In one experiment, a compressive force (preload) of 3 mN was applied for 1s and the target substrate was retracted until complete contact was lost. The maximum tensile force (pull off force) was recorded to be 12 mN. Adhesion measurements were repeated for preloads ranging from 3 mN to 20 mN (Figure 43b) and the mean value of pull off force was measured to be 11.45 mN with a deviation of $\pm 5\%$. The classical Johnson-Kendall-Roberts (JKR) [162] approach derives the adhesion between an elastic body and half space with adhesion force as a function of elastic modulus and contact radius. It is further independent of the applied compressive load (preload). One of the limitations of the JKR theory is the assumption of not considering any surface roughness. Tabor [163] and Maugis [164] provide the theoretical basis for effect of roughness on adhesion. In the present experiments, involving elastomer Sylgard 184 and a flat glass substrate, pull-off force is observed to be dependent on preload. Based on the previous studies, three major contributors surface

roughness [163] [165], viscoelasticity [166] and misalignment [167] (incomplete contact between the target object and deformable body) are considered to explain this observation. Qualitatively, due to the nature of silicones, the contribution from viscoelasticity will have a small contribution. The hold times in the present experiments were not found to have an impact on the measured pull off forces. Furthermore, repeated measurements against the same smooth substrate also diminishes the role of surface-roughness to affect adhesion. The dominant effect can then be explained based on the degree of misalignment which leads to partial contact at low preloads. Therefore, as found in the present study, a preload independent adhesion behaviour observed for the preloads ranging from 3 mN to 20 mN was used as an indicator for an aligned setup. As the adhesion strength becomes independent of the applied compressive load (preload), good contact and alignment is usually ensured between the two bodies. All the future measurements were carried out at a fixed preload of 3 mN. Once aligned, adhesion measurements were performed without any external bias. After an applied preload of 3 mN, a pull-off force of 12 mN was observed.

Optical images in Figure 44 give an overview of the experimental procedure. After applying a preload of 3 mN for 1s, the target was manually retracted until touch point was reached again (point of zero compressive force) as shown in Figure 44b. At this point a bias of 1.1 kV (V1) was applied, resulting in a net movement of the DEA to the left. As visible in Figure 44c, the stalk of the pillar which was glued to the DEA, was displaced to the left (shown by the direction of the arrow), whereas the tip was still in contact with the glass substrate. The bias was switched on for a varying duration and switched off prior to further retracting the pillar.

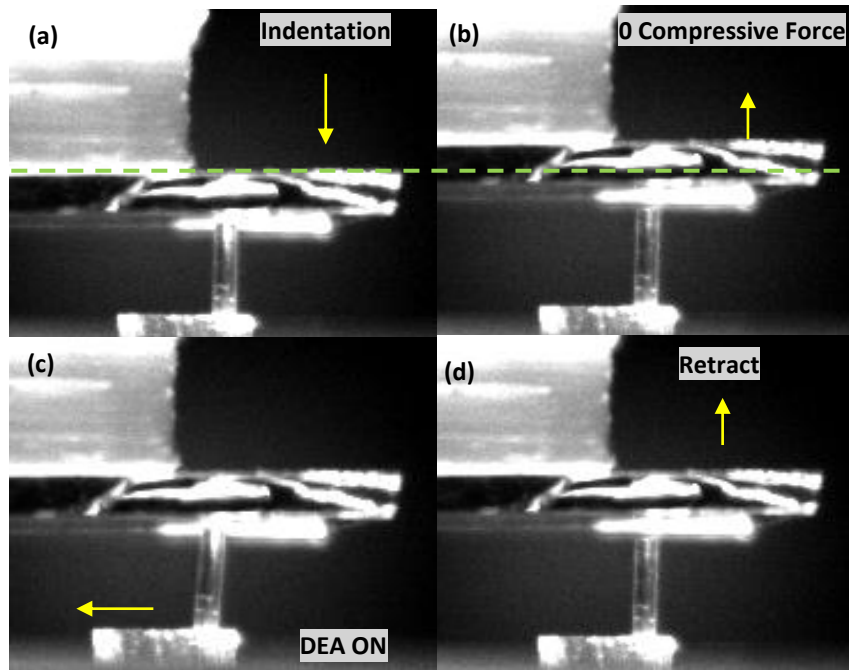


Figure 44 Optical images of the side view showing the pillar bending under shear induced torque (a) The micropillar is in contact with the target glass substrate. (b) Target attached to the linear drive is retracted to the point of zero compressive force. (c) A bias of 1.1 kV is applied, and the DEA displaces to the left as shown by the arrow. The backing layer and the stalk displaces while the tip is still in contact with the glass surface. (d) Target substrate is retracted after the bias was applied for 1 s.

4.7. Results and Discussions

4.7.1. Effect of varying hold time

As discussed in Section 4.6, all the measurements were performed at a preload of 3 mN. In Figure 45a, the force displacement curve for a preload of 3 mN is shown. No external bias was applied at this point. Corresponding force-time measurement was also recorded (Figure 45b). Approach and retraction of the target were carried out in steps of 1 μm and are marked by the direction of arrows. The different color bands correspond to the compressive and tensile regimes in the force-time and force-displacement curves. Green bands refer to the compressive zone while blue bands mark the tensile regime.

Figure 45c depicts the force displacement curve when the bias was applied for 5s. At this point, the target and the micropillar were in contact owing to Van der Waals forces. Now the electrical bias of 1.1 kV was switched on, resulting in the lateral displacement of 110 μm . As soon as the

bias was switched on, there was a sharp rise in the tensile force by 3 mN. This is because the DEA is laterally displaced, thereby displacing the microstructure with it. Furthermore, the pillar was also pulled away, as the dielectric film was compressed along the thickness. After applying the bias for 5s, it was observed that there was some residual adhesion and therefore the target had to be retracted until it was completely detached. The pull off force dropped from 12 mN at 0 V to 7 mN at a bias of 1.1 kV for 5s. Next, the measurement was repeated with the bias of 1.1 kV applied for an extended duration of 15s. Grey bands in the force time curve mark the time duration for which the bias to the DEA was switched on, resulting in lateral displacement with respect to the original position.

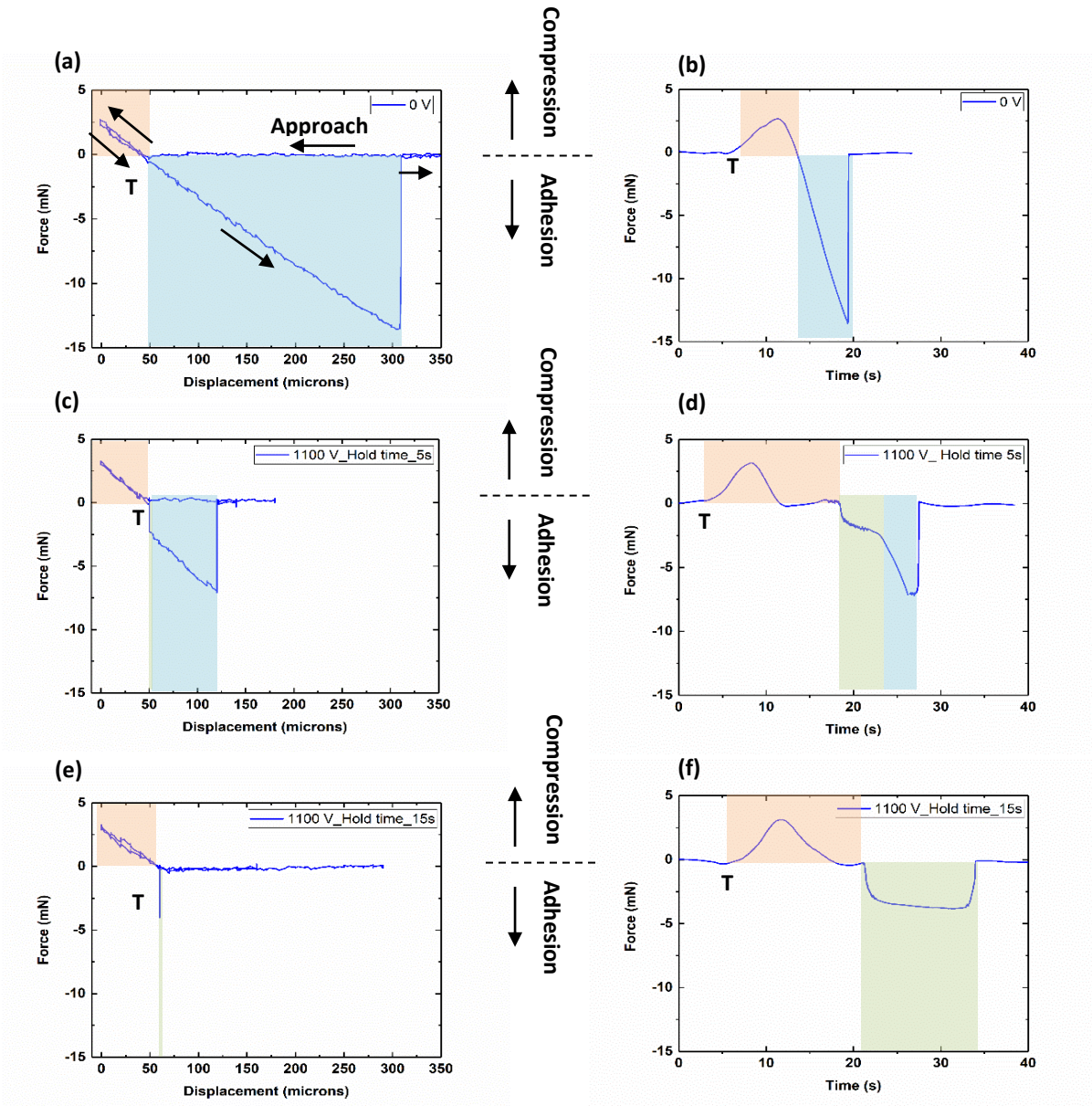


Figure 45 Adhesion measurements on an unbiased (a,b) and biased (c-f) DEA-microstructure assembly. Green bands represent the compressive regime, blue bands indicate the tensile region and grey bands in the force time curves illustrate the hold time duration for which the electrical bias was applied (a) Force displacement curve at 0V. A preload of 3 mN was applied for 1s and the measured pull of force is 12 mN. (b) Force-time curve at 0V. (c) Force displacement curve with 1.1 kV applied for 5s. Pull off force is 7 mN. (d) Force time curve showing the green region during which the crack is growing however at the end of 5s, target is retracted and the residual adhesion of 7 mN is measured marked by the blue band. (e) Force displacement shows complete loss of adhesion when the bias is applied for 12s. Arrows mark the approach and retraction phases in the measurement. (f) Force-time curve shows that during the time period of 12 s when the bias was turned on, the crack fully peels from one edge to the other

and the force drops to zero. Absence of blue band show that adhesion was lost solely by the shear-force due to DEA.

Figure 45e shows the force displacement curve, where the adhesion was completely lost. The force time curve shows that the entire contact was peeled off, as the tip lost contact with the target within 12s. No additional mechanical force was needed to overcome adhesion. The absence of blue band signifies, that detachment took place solely due to the shear-induced peeling. No further retraction was required, as was the case at shorter hold times.

4.7.2. Effect of varying bias on crack growth

In order to understand the detachment mechanism, the experiments were extended to different voltages of 1.0 kV, 1.1 kV, and 1.2 kV and different duration of bias switched on (hold time). Qualitatively, in order to observe the decay of pull-off stresses, DEA was biased, in increasing intervals of 5s and the residual adhesion was recorded as shown in Figure 46 a. The time taken for the contact to peel off is termed as the peeling time. The higher the applied voltage, the larger is the lateral displacement (Figure 43 a) and thus the pillar is subjected to additional lateral and tensile forces. These forces have been calculated in Section 4.7.4 assuming a simplified model. The pull off stress decreased from 35 kPa at 0 V to zero when the DEA was biased at 1.2 kV for 5 s (Figure 46 a) Similarly, as the lateral displacement is low at lower voltages, it took longer for the contact to peel. It is observed that it took 12s for the loss of adhesion at 1.1 kV whereas even after a duration of 20 s the pull off stress of 2 kPa was measured at a bias of 1.0 kV. Similar trends were also observed when the work of separation was calculated at these voltages, by integrating the area under the adhesion curve (Figure 46b).

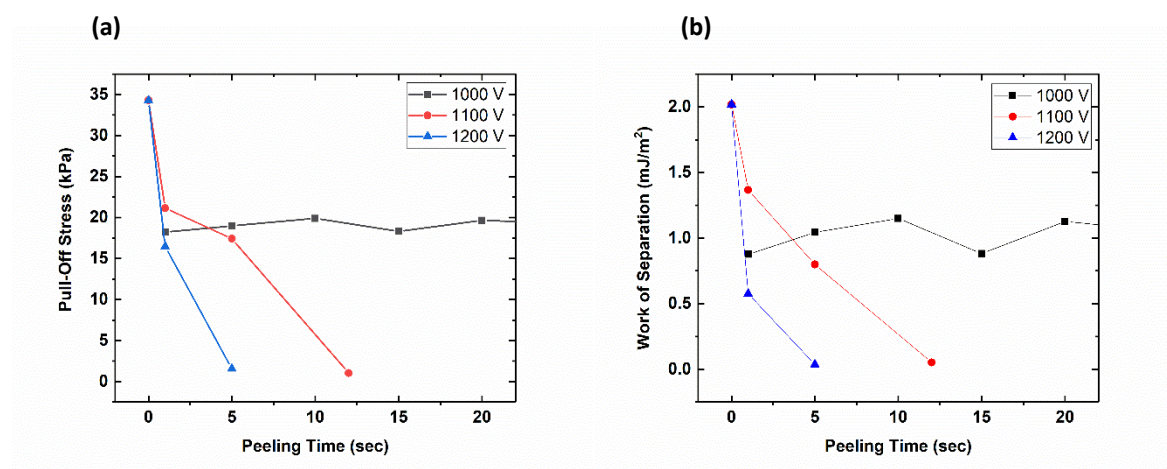


Figure 46 Effect of varying bias on Peel time (a) Decay in pull-off stress was measured at bias of 1 kV, 1.1 kV and 1.2 kV with increasing time duration of applied bias and the time taken for the contact to fully peel off was measured. (b) Work of separation also shows similar trends as the pull-off stress for the corresponding bias.

4.7.3. Time Dependence of Crack Growth

The optical images in Figure 47 (b-e) capture the contact signature showing the evolution of a crack that proceeds from the edge opposite to the direction of applied shear force. The force time curve in Figure 47 a results from the adhesion measurement when a bias of 1.1 kV was applied for a hold time of 15s. After retracting the target substrate to the point of zero compressive force, as denoted by the touch point T, the bias was switched on. As soon as the bias was switched on, there was a drop in measured force.

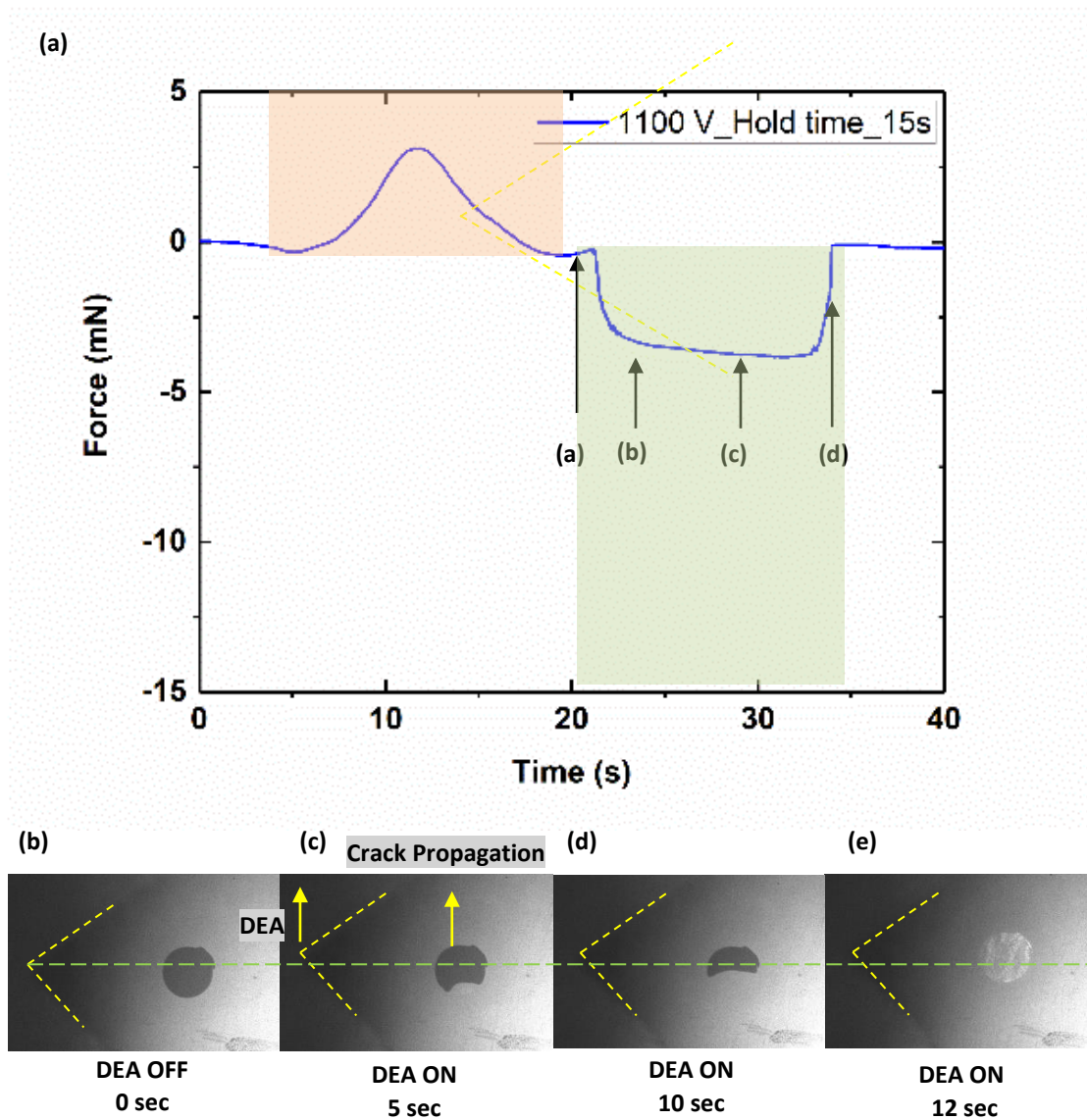


Figure 47 Effect of hold time on crack growth (a) Force time curve showing the crack propagation at a bias of 1.1 kV, applied for 15s. (b-e) Optical images show the top view of the contact.(b) High contrast shows that the tip is in contact with the glass surface.(c,d) Crack initiates at the edge opposite to the direction of the applied shear force as shown by the direction of the arrow.(e) Complete loss of contrast shows the contact has completely peeled off. Dotted lines in yellow mark the edge of the displaced backing layer in the background when the bias was switched on.

This tensile force is attributed to the squeezing of the sandwiched elastomeric layer of the DEA, and dominantly the lateral displacement. As it squeezes in the thickness direction and laterally displaced, it pulled the microstructure away from the glass. The plateau region depicts the hold time of 15s, where the defect propagated from the edge. At the end of 12s, the tip had

completely peeled off from the surface and the pull off force dropped to zero. The peeling took place as the crack propagated from one edge to the other and grew across the interface. No mechanical force was needed to achieve this, as otherwise needed at shorter holding times as seen in Figure 47 e. This demonstrates that the shear induced due to in-plane displacement of the DEA enabled peel detachment of the microstructure from the target substrate.

The observation of an edge crack is untypical for mushroom shaped pillars. Previous studies by [168] [169] have explained the occurrence of an edge or center crack by analyzing the different stresses acting on a fibril (flat vs mushroom tip) under a normal tensile load. In an ideal case, the corner stress singularities in a flat tip fibril lead to an edge crack. By modifying the tip to a mushroom cap, the additional material at the circumference reduces these corner singularities. The stresses at the center of the stalk are higher, thereby favoring detachment via a center crack. Additionally, the presence of defects [158] modifies this behavior by acting as local sites where the fibril loses contact and in turn leads to a deviation from the expected crack types.

The situation differs in the present scenario as the fibril is under an inhomogeneous stress distribution. Lateral displacement of the DEA induces a tensile stress in the fibril leading to elongation of the pillar. Additionally, the pillar bends under the torque acting at the contact interface. These stresses collectively result in the edge opposite to the applied shear, as the preferred site for detachment, which is also observed in the present study.

The time dependence is speculated to be arising as a result of the viscoelasticity of the silicones. The elastomeric fibril used in this study was fabricated using Sylgard 184. For a perfectly elastic material, the crack would proceed instantly across the interface. Persson et al [170] [171], have studied the influence of viscoelasticity and surface roughness on adhesion for Sylgard 184 by analyzing the work of adhesion as a function of crack tip velocity by introducing viscoelasticity in the theoretical calculations. For a lower crack tip velocity, the experimental results agree with their theoretical calculations.

Another hypothesis to explain the time-dependence can be understood as follows. In addition to the inhomogeneous stress distribution discussed above, in-plane stresses also develop at the interface when the fibril is preloaded and brought back to the touch point. As the fibril is geometrically constricted between the two ends, these stresses are only able to relax when the

peel front develops at the edge, once the DEA is biased. As the peel front grows, the defects can act as sites where these in-plane stresses advance quickly. Depending on the distribution of these defects, some contacts may break and reform and collectively govern the time scale of detachment. In these instances, may be a threshold value of stress is reached, at which the peel front is not able to propagate and there, defects might pin the contact line. This is only an assumption and needs a sophisticated FE analysis of the stress distributions at the peel front which is beyond the scope of this work.

Furthermore, silicones are also present as the dielectric material in the DEA. These materials have been studied and different theoretical frameworks [70] [172] have been discussed to account for the dissipative processes of silicones in a DEA. Some studies are also investigating the effect of pre stretch to reduce the relative creep behavior arising from viscoelasticity [173].

An experiment was designed to further shed light on the influence of the torque acting on the fibril, wherein a center crack was specifically formed due to inhomogeneities arising from a curvature in the mold in the center of the pillar tip. Figure 48(a-h) show the progression of an edge crack in a fibril with a prescribed delamination of the center region. As soon as the DEA is biased, the edge crack arising at the pillar edge opposite to the direction of lateral displacement of the DEA propagates through the contact area and fuses with the center crack before completely peeling off. Edge cracks are particularly unstable in comparison to the center cracks and preferred for achieving low adhesion states by facilitating the release process.

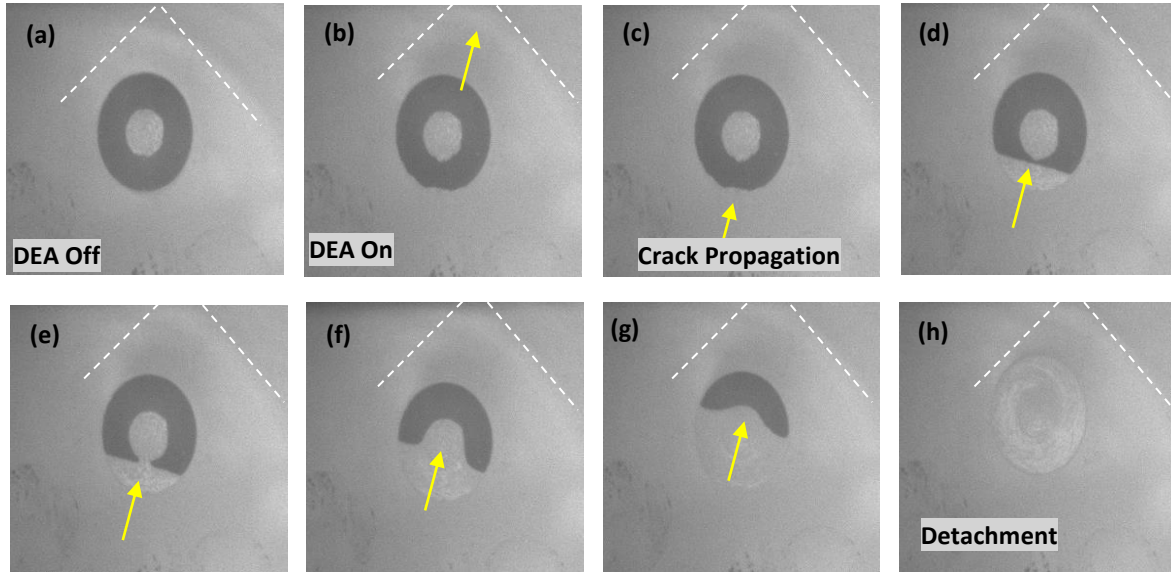


Figure 48 Crack growth in a fibril with a prescribed center crack (a) Top view shows a fibril in contact with the target substrate (dark circle). The bright spot in the center arises from a center crack where contact to the substrate is lost. Dotted white lines mark the edge of the backing layer. (b-e) Backing layer corner displaces out of the view of the image when the bias is on. An additional crack originates at the edge and the center crack fuses with the propagating edge crack. Loss of contrast in (h) shows that the crack has peeled completely.

4.7.4. Detachment under tensile loads

Force time curves of the pillars under tensile loads are shown in Figure 49. After applying a preload of 3 mN, the fibril was retracted, until a tensile force of 1 mN (Figure 49a), 2 mN (Figure 49b) and 8 mN (Figure 49c) was reached in three different experiments. This corresponds to an effective deformation of 15 μm , 30 μm and 140 μm respectively in the system (fibril + backing layer + DEA membrane). Under this tensile load, the DEA was biased at 1.1 kV. The slight relaxation of the initial tensile force during that holding time is attributed to the viscoelastic properties of the elastomeric fibril, backing layer, and DEA membrane. As in the previous Figure 45, the green bands in the diagrams correspond to the compressive region and the tensile regions are shown in blue. Green bands mark the time during which the bias was applied. Compared to the initially relaxed fibril (subject to no compressive or tensile load) (Figure 47), cracks propagated much faster when under an initial tensile load. For the relaxed fibril, it took 12 s for the loss of complete adhesion. This time period was reduced to 9.3 s under a tensile load of 1 mN (15 μm net elongation), to 2 s under a tensile load of 2 mN (30

μm net elongation) and further reduced to 800 ms under a tensile load of 8 mN (140 μm net elongation).

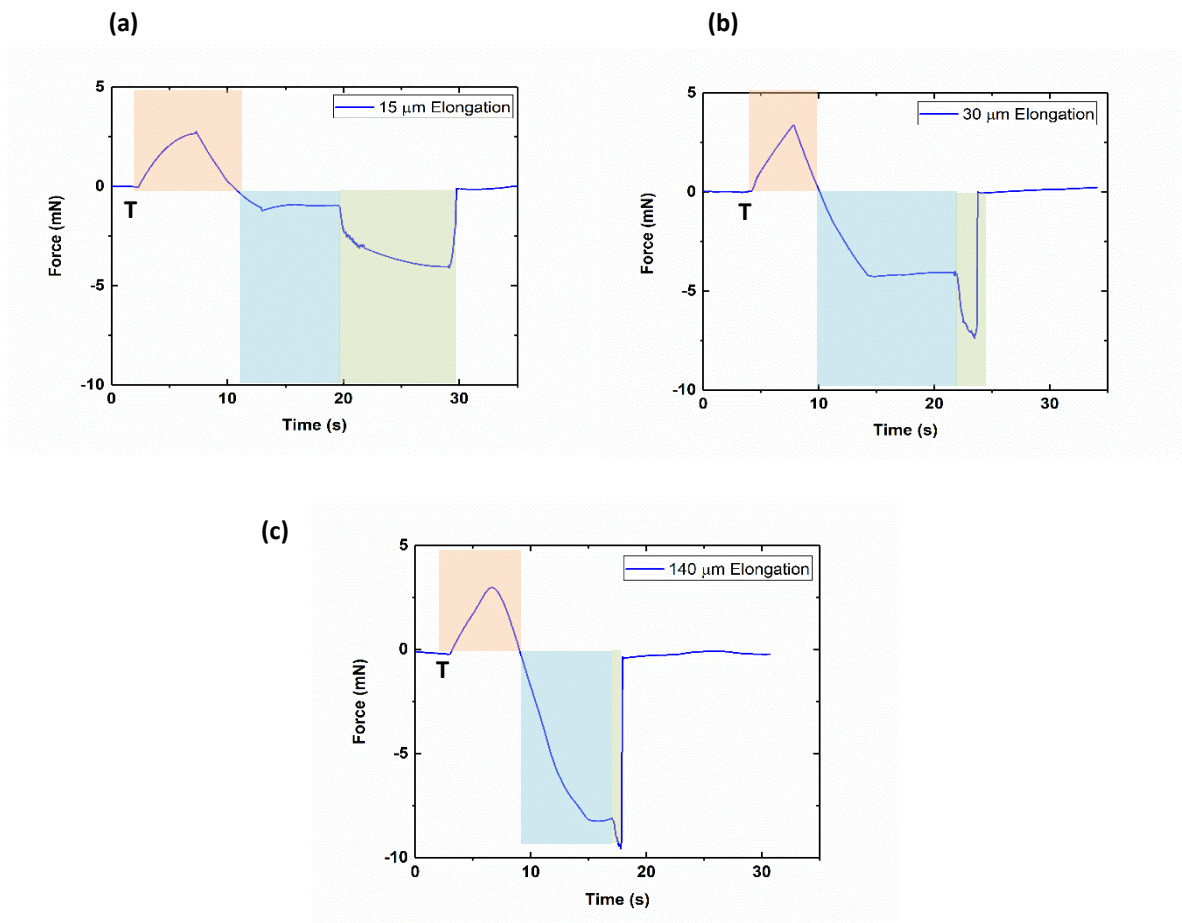


Figure 49 Force time curves for axially elongated pillars when subjected to bias at elongations of (a) 15 μm (b) 30 μm and (c) 140 μm . The detachment time was found to be reduced due to high tensile stresses acting along the fibril.

In the above sections, we observed that the lateral displacement between the DEA and target substrate, while the fibril stayed in contact with both (under condition of no slippage), leading to a bending and elongation of the pillar and in conjunction also with the torque at both ends of the fibril.

Figure 50 illustrates this detachment process. The voltage-dependent displacements of the backing layer in comparison to the pillar length are relatively small ($< 10\%$) and do not allow for detailed information (gained from the experiments) regarding the peel angles and the relative strains in the individual mechanical components – namely the fibril, backing layer and

the dielectric actuator. A detailed analysis is required to calculate the bending moment, acting at the interface between pillar and substrate due to the lateral displacement between backing layer and substrate.

In this section, a simplified analysis is presented, to gain some estimates of the evolution of peel angle under tensile loads at lateral displacement.

The angle between the original position of the fibril and the final position at maximum lateral displacement at each bias is defined by α . We define the peel angle as the maximum angle between the fibril and the target object and which evolves opposite to the direction of the lateral displacement represented by θ (i.e. $90 + \alpha$). As explained in Figure 41, the dielectric actuator consists of three periodic sections with the movable bars. Figure 50a shows the side view for one of these sections. There are two different experimental cases under discussion.

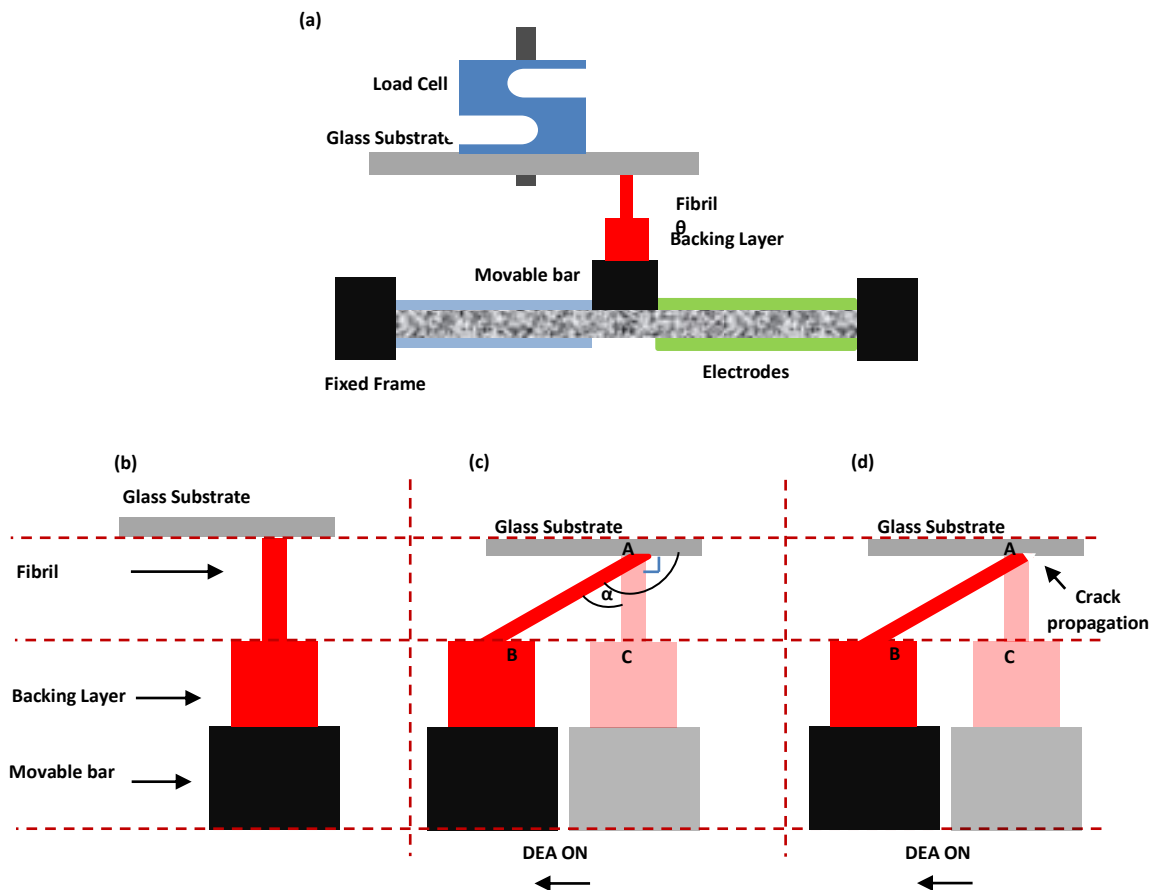


Figure 50 Schematic showing an elongated fibril bending due to shear-induced torque (a) Schematic showing the micropillar integrated with the dielectric elastomeric actuator on the movable bar. It is in contact with the glass substrate (b) Zoomed in view depicting the

micropillar with the backing layer and the movable bar. (c) Zoomed in view showing micropillar under deformation once the DEA is biased. Arrows mark the direction of lateral displacement. The figures are not drawn to scale and present only a simplified view of the fibril with the backing layer displaced due to the action of dielectric actuator. (d) With time, the peel front at the interface starts to grow.

The force-time and force- displacement measurements for the scenario shown in Figure 57(a-b) were discussed in Figure 45. In the force-time curves shown in Figure 45(d-f), as soon as the DEA is switched on, a tensile force was measured. This is marked by the onset of the green section. The experimentally measured peel stress corresponds to 8.76 kPa. Using these calculations, a theoretical estimate of the peel stress (shear and normal stress) is obtained to compare with these experimental values.

Figure 50b shows an illustration of the fibril, backing layer and the movable bar. The DEA action displaces the backing layer, leading to elongation and bending of the pillar (Figure 50c). As the pillar is in contact with the glass substrate, the substrate is pulled down. The sketches are not drawn to scale and the angles have been exaggerated for clarity. Furthermore, the calculations have been carried out for a fibril with a flat tip as opposed to a mushroom tip used in the experiments. In an actual scenario, the pillar will deform and have a curvature at the interface once it is bent and elongated. This has not been reflected in the drawings. Figure 50d shows the beginning of the crack at the interface.

Some simple mathematical estimates of stresses and strains in the fibrils are presented in the Appendix.

4.7.5. Micropatterned Arrays

This study discusses the detachment mechanism for a single micropillar. In order to further extend the findings for realizing a gripper, it becomes important to analyze the differences once an array of microfibrils is integrated with the DEA. Keeping the material constant, few of these possible scenarios from the design perspective are:

I. Design of DEA

A circular DEA can be designed where in-plane actuation corresponds to expansion and contraction of the active region in the DEA and the pillars have rotational symmetry. Pillars in an array will experience different displacements depending on their position. The majority of

pillars can then be distributed at the outer circumference so that they experience maximum displacement and bending moment leading to early detachment. The pillars that get displaced the farthest will bend more and will lose contact earlier as compared to the rest. In effect, the load distribution per pillar still in contact will increase, facilitating quicker detachment of the remaining pillars.

The active regions in the DEA can also be designed in a way that the bending moment for all the pillars can be directed radially inwards or outwards for precise handling.

II. Design of Pillars

The highly simplified mathematical estimates discussed in the Appendix, show that the maximum deformation arises from the DEA membrane. An array of pillars with dissimilar lengths can also be integrated. In case of a small and light-weight object, a low preload will be applied, so that only the longer pillars will come in contact. For heavier objects, the preload will be increased, so that also the shorter pillars get in contact. Buckling of the taller pillars will be prevented as the DEA membrane will provide the main requisite deformation.

4.8. Conclusion

Our experimental findings reveal a novel method that exploits the in-plane actuation of the dielectric elastomeric actuator to induce peeling of the fibril at the interface with the target substrate. Overall, the results can be summarized as follows:

- In the set-up used, a bias of 1.1 kV applied to the DEA led to an in-plane displacement of 110 μm which caused peeling of the microfibril from the glass substrate in 12s. At a higher bias of 1.2 kV, the contact peeled in 5 s. The peel stress was experimentally measured to be 8.76 kPa and the calculations showed a deviation of about 25 %, being in good agreement in first approximation.
-
- Detachment occurs via peeling at the interface of the fibril and the glass substrate, due to the torque that acts on the fibril from the lateral displacement of the DEA. The theoretical estimates discuss how the peel angle evolves differently under scenarios when the pillar is subjected solely to the elongation due to DEA as compared to an

elongation due to additional tensile loads. Only edge cracks were observed, in contrast to studies on mushroom-shaped pillars under normal pulling forces. The reason lies in the torque acting at the interface owing to lateral displacement of the DEA, directing a detachment from the edge. The detachment started at the edge in the direction opposite to that of the displacement of the substrate by the DEA.

- It is experimentally observed that under additional tensile loads, peeling times are expedited. As the peel stresses will be highly inhomogeneous as discussed, they can only be calculated in good approximation using “Finite Element Analysis” (FEA) which is out of the scope of this thesis. The simplified calculations also reveal that the maximum deformation under tensile loads is arising from the DEA membrane and along with the fibril and backing layer it is sufficient to result in peeling at the interface.
- The reasons for the time dependence of the detachment process were not fully clarified in the present study. It is not unlikely that some viscoelastic contribution to the fibril deformation was responsible for this effect. In terms of potential application, such a time dependence could be undesirable and should be minimized by the materials or the design.
- The present study confirmed the principal feasibility of detaching a single polymeric adhesive fibril from a glass substrate by actuation with a DEA. In order to detach a whole array of many fibrils, further considerations will be necessary. For example, the amount of shear, and therefore torque, on the individual fibrils will depend on the relative position the fibril and hence the fibrils will detach at different times. This could possibly be utilized to realize controlled detachment from delicate objects. Further work along these lines is necessary to validate the concept for handling applications.

Chapter 5: Summary and Outlook

5.1. Summary

Adhesion modulation is equally significant in designing a multi-target handling system as in a live gecko. Relying on principles of contact mechanics, researchers tailor dry adhesives for different target objects. Microstructure tip geometry [30] [155] [169], aspect ratio [174], backing layer thickness [175] and elastic modulus of materials [176] are different variables that help customize the stress concentrations at the interface of the adhesive and target object. These findings provide dedicated solutions for each application however do not offer dynamic control over adhesion strengths.

In the first part of this thesis, electric fields were harnessed in combination with the dry adhesives to tune the adhesion strengths. By fundamentally analysing the superposition of electric fields on Van der Waals mediated adhesion through a custom made electroadhesion measurement setup, the electrical forces were engineered to enable attachment (via electroadhesion) and detachment (via Dielectric Elastomeric Actuators) of patterned adhesives. Analysis of the force- displacement measurements showed an adhesion strength increase by a factor of 2 with an applied DC potential of 2 kV in comparison with the scenario without any externally applied bias. It was observed that electrical fields also exert a preloading effect which is attractive. This is extremely useful for handling fragile target objects such as thin foils and silicon wafers, where compressive preloads can be invasive for these objects.

The second part of the thesis focussed on release mechanism for detaching microstructures for placing the target objects. For automated handling of components in the industry, release mechanisms are critical in addition to the pick-up processes. A membrane DEA was combined with a high aspect ratio macroscopic fibril and a novel release mechanism was investigated and demonstrated. The in-plane deformation facilitated the introduction of a crack at the contact interface. By using DEA to induce a shear detachment, the crack growth always proceeded via an edge crack which originated opposite to the direction of applied shear force. This is connected to previous statistical studies on the detachment behaviour which have shed light on the role of local surface defects of individual fibrils in governing the global adhesion of an array [111] [158]. Depending on the presence of local defects and the stress concentrations at

the interface, the detachment process was found to proceed via a distribution of centre and edge cracks. Centre cracks on average take longer to proceed whereas edge cracks are faster and unstable [158]. Furthermore, studies at different bias voltages showed that the release times could be accelerated from 12 s at 1.1 kV to 5 s for a bias of 1.2 kV. Limited by the breakdown field strength of the actuator being used, the maximum operating voltage was restricted to 1.2 kV. However, by tailoring the design and material properties of the device, higher voltages could be applied, which in turn will further reduce the release duration. Thus, electrical fields can also dynamically regulate crack growth and expedite the release times.

Overall, electric fields were successfully integrated with micropatterned adhesives. They provided additional dynamic control over the adhesion and detachment processes to meet real time requisites for different applications.

5.2. Outlook

With steps toward Industry 4.0, automated and self-regulatory multifunctional systems are in demand more than ever [177]. From this perspective, attachment and detachment regulation offered via electric fields can pave the way for incorporating more sophistication for designing collaborative robots (cobots) equipped with micropatterned adhesives.

Presently these prototypes are in the testing phase at the research level. However, efforts have started towards scaling them up for large area fabrication. Roll to roll manufacturing processes are developed for manufacturing dry adhesives [178]. Similarly, large scale fabrication of electrodes via techniques such as laser ablation are being tested for DEAs [179]. Such efforts will further strengthen the possibility of producing the combinatorial adhesive prototypes (dry + DEA) at large scales. DEAs are starting to find applications in commercial products [180].

Within the scope of this thesis, the detachment mechanism was experimentally demonstrated for a single micropillar. It will be interesting to study the behaviour at the level of an array of similar fibrils, as the distribution of local defects at the pillar surfaces will influence the detachment process.

Electrostatic preload reported in this thesis has been concluded to be useful in handling of fragile objects such as thin foils etc. In other studies, this preload has also been demonstrated to help compensate for the loss in adhesion in case of micropillars fabricated from high

modulus materials [181]. Similarly, dry adhesives are highly sensitive to misalignment between the adhesive pad and the target object. Electrostatic preloads can also be evaluated in their potential for creating an equal load sharing condition for the fibrils.

With the flexibility to optimise design, materials and their implementation across the three technologies of electroadhesion, dry adhesion and dielectric actuators, there exists a huge space for innovation.

Appendix

A. Additional Information: Chapter 3

I. Dependence of the electroadhesion force on the a/b ratio.

Figure 51 shows the dependence of the electroadhesion force on a/b , i.e. the ratio of the electrode width to the array period.

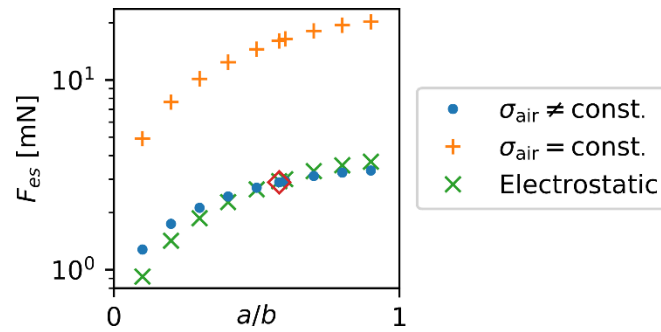


Figure 51 Dependence of the electroadhesion force on the a/b ratio for $\delta = 1 \mu\text{m}$ and $V_0 = 2 \text{ kV}$. Blue points are for $E_c = 3 \text{ MV/m}$ and $s_L = 1 \mu\text{m/V}$

II. Model validation for flat surfaces

For validation we compared our numerical model to the results reported in (Cao et al., 2016). Therefore, simulations were performed using the geometry similar to that shown in Figure 52 (c), without a pillar array. Cao et al. report that in a flat-flat contact (i.e., non-patterned elastomer film and a flat wall as a target surface) the average adhesion stress σ_{ad} has the form

$$\sigma_{ad} = \frac{1}{2} \varepsilon_0 \left(\frac{V_0}{2b} \right)^2 \left[\left(\frac{\varepsilon_w}{\varepsilon_0} \right)^2 - 1 \right] C = \sigma_0 C$$

A1.

where V_0 is the voltage applied to the electrodes, b is the half-period of the electrodes, ε_w is the permittivity of the wall, C is a dimensionless stress scale function dependent on the geometric parameters of the system, i.e. electrode width, elastomer and air gap thickness as well as the permittivity ratio of the elastomer and wall. We define $\sigma_0 \equiv \frac{\sigma_{ad}}{C}$. This equation was

derived with the approximation that the system is periodic with symmetry planes through the center of each electrode and antisymmetry planes in between the electrodes.

Figure 53 shows the influence of chosen dielectric and geometric parameters on the electroadhesion stress scale. Our numerical results almost quantitatively reproduce the theoretical prediction based on eq. A1. They slightly underestimate the stress values, by 5 to 13%. This may be due to the different numerical methods employed, as the cited values were obtained with a point matching method described in Ref. (Marcuse, 1989).

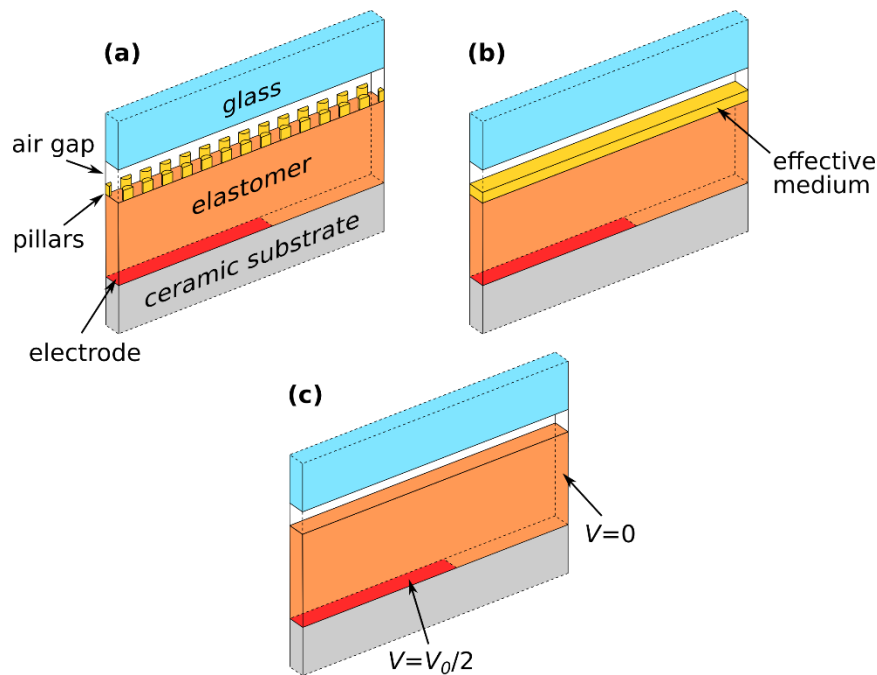


Figure 52 Illustration of the periodic numerical model geometry. (a) Realistic representation of the hexagonal pillar array. (b) Pillar array layer represented by an effective medium approximation. (c) Model with no pillar array or effective medium.

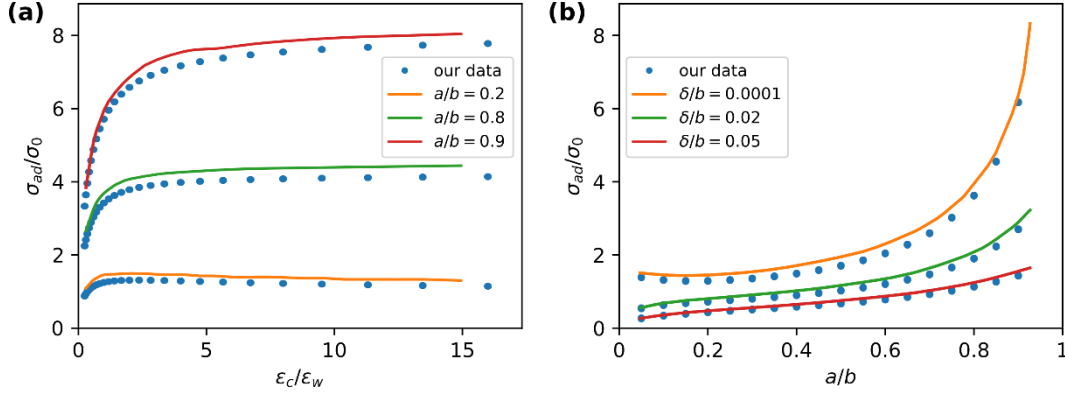


Figure 53 Comparison of the non-dimensional electroadhesion stress $\frac{\sigma_{ad}}{\sigma_0}$ (a) as a function of the permittivity ratio $\frac{\epsilon_c}{\epsilon_w}$ of the cover and the wall, respectively, for three values of $\frac{a}{b}$ and (b) as a function of $\frac{a}{b}$ for three values of $\frac{\delta}{b}$. Blue symbols represent our results, solid lines those of [48].

III. Validation of the effective medium approximation

In order to validate the effective medium representation of the micropillar array, we consider a periodic cell model, assuming an infinite electrode array contacting an infinite, flat object. In this case an elementary unit cell can be defined, bounded by adjacent symmetry planes. Figure 52 (a-b) shows two considered geometries, Figure 52a a realistic representation of the hexagonal micropillar array and Figure 52b an effective medium approximation. We consider all external boundaries to be symmetric ($n \cdot E = 0$), with exception of the boundary intersecting the space between electrodes, where an antisymmetry condition holds ($V = 0$).

Figure 55a shows the average electroadhesion stress σ_{ad} as a function of air gap thickness δ , considering the realistic pillar array geometry (dashed orange line, Figure 52a) and an effective medium approximation (solid blue line, Figure 52b). Both lines overlap and converge to an exponential function (grey dotted line). In Figure 55b the ratio of the two extracted stresses is plotted as a function of δ , σ_{ef} relating to the effective medium approximation and σ_{pil} to the realistic geometry. At $\delta = 1 \mu\text{m}$ the effective medium approximation *underestimates* the pressure by around 2% but at $\delta > 3 \mu\text{m}$ it *overestimates* the pressure by less than 1%.

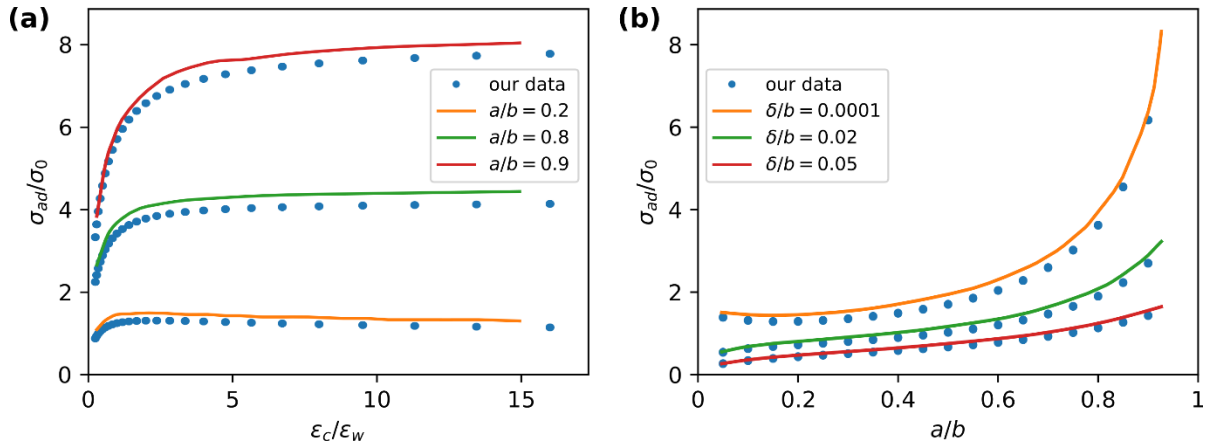


Figure 54 Comparison of the non-dimensional electroadhesion stress $\frac{\sigma_{ad}}{\sigma_0}$ (a) as a function of the permittivity ratio $\frac{\epsilon_c}{\epsilon_w}$ of the cover and the wall, respectively, for three values of $\frac{a}{b}$ and (b) as a function of $\frac{a}{b}$ for three values of $\frac{\delta}{b}$. Blue symbols represent our results, solid lines those of Cao et al., 2016.

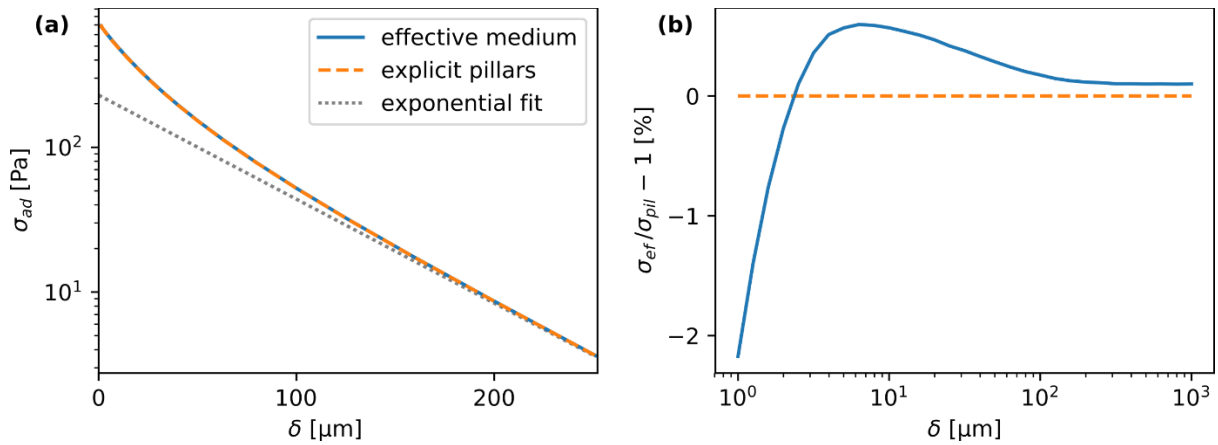


Figure 55 (a) Average electroadhesive pressure considering realistic pillar array geometry (dashed orange lines) and an effective medium approximation (solid blue lines) as a function of air gap thickness δ . Both lines overlap and converge to an exponential function (grey dotted line). (b) Ratio of the two extracted pressures as a function of δ . At $\delta = 1 \mu\text{m}$ the effective medium approximation underestimates the pressure by around 2%.

IV. Comparison between idealized and realistic geometries of the electrode array

Figure 56 shows a comparison of logarithmic pseudocolor maps of the electroadhesion pressure for the electrostatic model for $\delta = 1 \mu\text{m}$ and $V_0 = 2 \text{ kV}$, using different computational domain geometries. Figure 56a A realistic electrode array geometry including horizontal electrode

segments, Figure 56b an idealized geometry which assumes a symmetry plane at $y = 0$ and an antisymmetry plane at $x = 0$ (dashed white lines) and Figure 56c an infinite array, derived from the periodic unit cell model, presented in subsection III. In Figure 56c the pressure map is obtained by tiling the periodic cell results. Here, the curvature of the lens is accounted for by spatially varying the air gap thickness [akin to the Derjaguin approximation known from the theory of Van der Waals forces (Derjaguin, 1934; Parsegian, 2005)]. The fringe fields at the edges of the electrode array are noticeably different in each of the three models. This difference, however, accounts for less than 3% of the total force on the object and is therefore not significant. Model in Figure 56a is the most realistic, but also the computationally most expensive. Model in Figure 56b reduces the required number of mesh elements by 75%. Model in Figure 56c is computationally the most efficient and allows to include the micropillars explicitly, but does not allow to realistically consider electrical conduction and requires approximating the shape of the target if it isn't flat and parallel to the array. We decided to use model in Figure 56b in the main text.

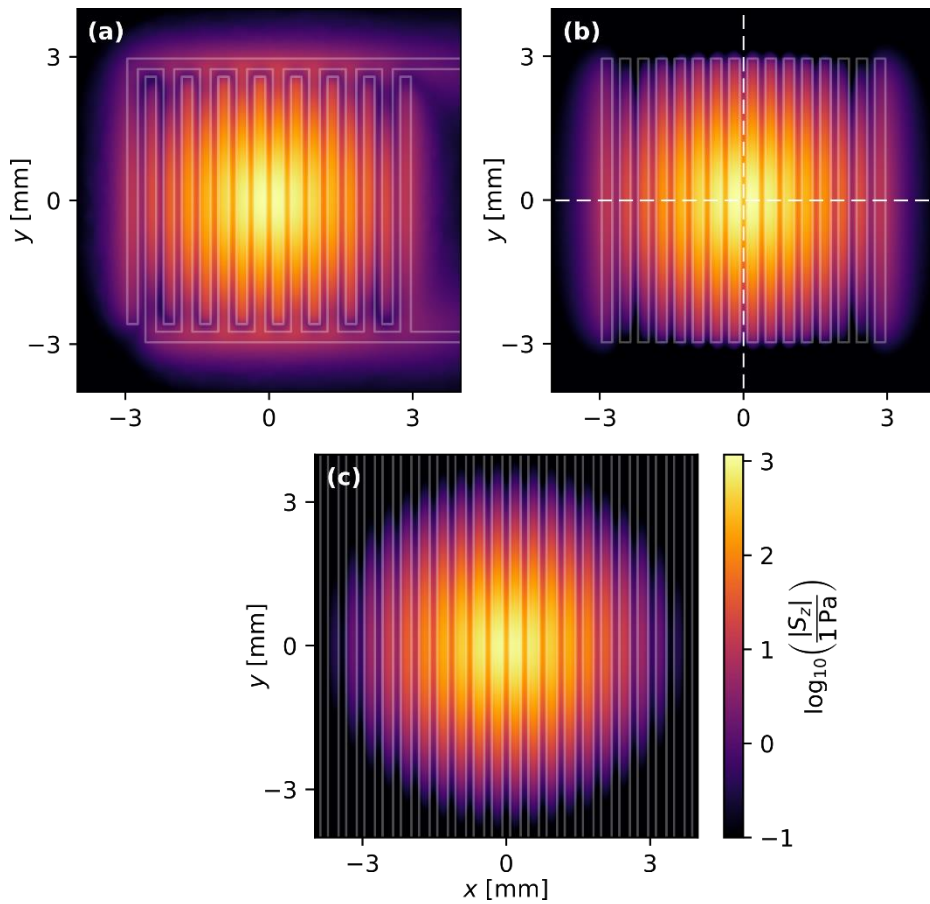


Figure 56 Logarithmic pseudocolor maps of the electroadhesion pressure for different electrode array shapes represented by the faint white lines, when $\delta = 1 \mu\text{m}$ and $V_0 = 2 \text{ kV}$. (a) Realistic electrode geometry including horizontal electrode segments. (b) Assuming a symmetry plane at $y = 0$ and an antisymmetry plane at $x = 0$ (dashed white lines). (c) Infinite array, derived from the periodic unit cell model.

V. Scaling of Maxwell traction for purely dielectric materials

We consider a simplified system of a bilayer of two materials a (air) and b (lens) sandwiched between two parallel plate electrodes, to make it amenable to an analytical treatment. In this case the electric field vector only has a single non-zero Cartesian component. The Maxwell traction acting at the interface scales as

$$\varepsilon_a E_a^2 - \varepsilon_b E_b^2 = \varepsilon_a E_a (E_a - E_b) = \varepsilon_a E_a^2 \left(1 - \frac{\varepsilon_a}{\varepsilon_b}\right) = \frac{\varepsilon_b - 1}{\varepsilon_b} E_a^2$$

A2.

where in the first and second steps we have used the discontinuity condition $\varepsilon_a E_a = \varepsilon_b E_b$. In the last step, we used $\varepsilon_{air} \approx 1$. The traction, therefore, approaches a constant for large ε_b (essentially all the voltage drop will be in the a phase and also E_a will become constant). Similarly, it scales as $\varepsilon_b - 1$ for small $\varepsilon_b \approx 1$ (because now $E_a \approx E_b$ both become constants, which are determined by the spacing of the electrodes). Both limits are in accordance with the results in Figure 40c in the manuscript.

The electroadhesion geometry includes two air-lens interfaces instead of one. However, the electric field at the more distant interface further away from the electrode array is already so weak due to the rapid exponential decay of the field strength, that its contribution to F_{es} is negligible.

B. Additional Information: Chapter 4

Peel Angle: Theoretical Estimates

All the following calculations only present a very simplified view of the different scenarios. In the real detachment process, the stress distribution will be inhomogeneous due to the bending

of the pillar under the existing bending moment and peeling process. The stresses will be higher at the crack front and lower at the other end.

We define the following stresses: The “peel stress” (σ_p) is the axial stress along the pillar at any angle alpha. The normal stress (σ_n) is the stress component normal to the surface of the glass plate, the shear stress (σ_s) parallel to it. The initial length of the fibril is represented by AC and the elongated length is given by AB as shown in Figure 57. BC represents the maximum lateral displacement at any applied bias. The maximum measured displacement $s = BC$ was $110 \mu\text{m}$ at a bias of 1.1 kV , the fibril length $L_0 = AC$ will be assumed as $1600 \mu\text{m}$.

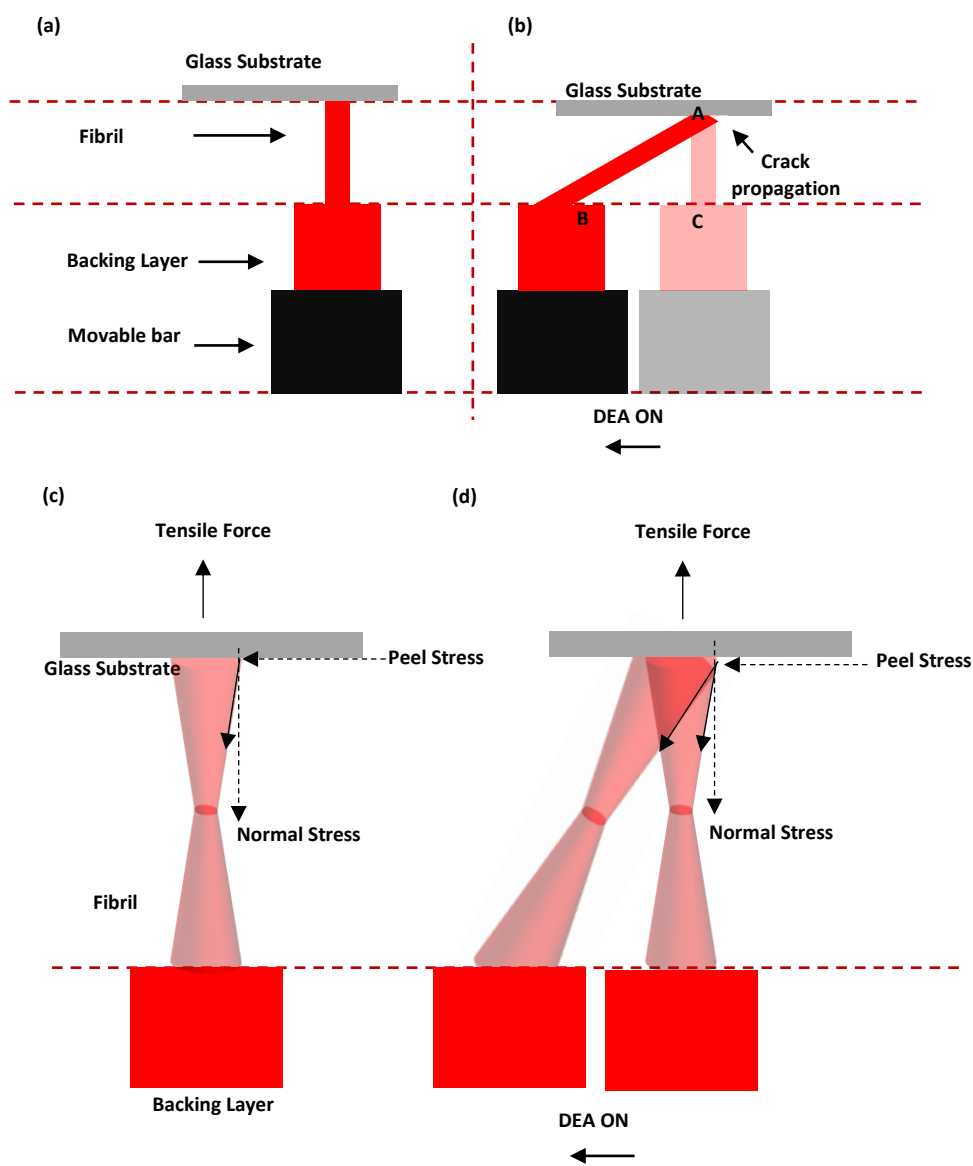


Figure 57 Simplified schematic of the pillar deformation during shearing and pulling: Scenario 1 (a) Schematic showing the fibril at its original position with no compressive or tensile force. (b) DEA is switched on resulting in lateral displacement of the fibril and beginning of an edge crack due to peeling at the interface under the influence of a shear-induced torque. Scenario 2 (c) Before switching on the DEA, a tensile load is applied to the fibril. A simplified sketch illustrates the pillar as divided in two symmetric truncated cones (d) DEA is switched on. The pillar, backing layer and DEA as a whole deform (elongate) more in comparison to scenario 1. The pillar deformation is highly simplified, and the Poisson contraction is exaggerated.

Using simple trigonometry, we find for the maximum displacement an angle alpha of:

$$\alpha = \arctan \frac{s}{L_0} \approx 3.9^\circ$$

B. 1

For the longitudinal strain in the fibril, we arrive at:

$$\epsilon = \frac{L - L_0}{L_0} = \frac{1}{\cos \alpha} - 1 \approx 0.00236$$

B. 2

Hence, the maximum peel stress $\sigma_p = E\epsilon$ where $E = 2.8$ MPa is Young's Modulus of Sylgard 184, yielding

$$\sigma_p = 6.608 \text{ kPa}$$

B. 3

The resulting maximum shear stress is

$$\sigma_s = \sigma_p * \sin \alpha = 0.070 \text{ kPa}$$

B. 4

and the maximum normal stress

$$\sigma_N = \sigma_P * \cos \alpha = 6.59 \text{ kPa}$$

B. 5

The experimentally obtained value for the peel stress is 8.76 kPa, about 25 % higher than the result of this simple calculation.

We define the peel angle θ as the maximum angle between the fibril and the substrate. In scenario 1, when the DEA is switched on under conditions of zero compressive load on the fibril, θ is measured as 94° .

Now, in scenario 2, we also consider the contribution of the DEA-membrane and the backing layer and the overall deformation (elongation) of the system under additional tensile force. Figure 58 depicts different components namely the fibril, backing layer and the DEA under elongation. The strains acting in each of the components differ owing to different areas of cross-section. The drawing in Figure 58 shows a simplified version, again with the degree of deformation exaggerated for clarity.

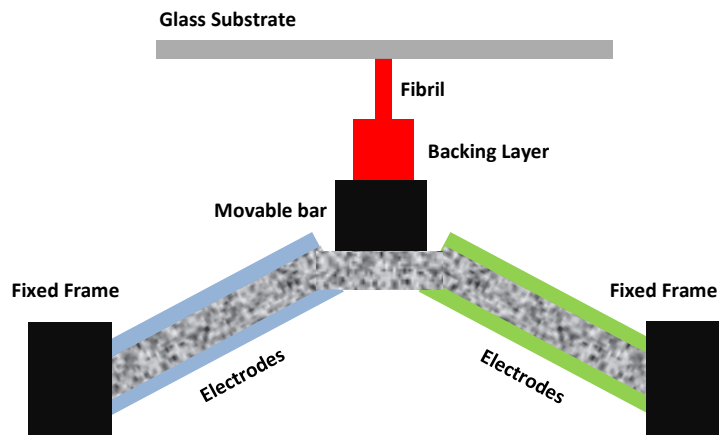


Figure 58 Schematic representing the scenario when a tensile load is applied to the fibril. All the components comprising the fibril, the backing layer and the DEA membrane undergo deformation. The angle of deformation is exaggerated for the purpose of understanding and the figure is not drawn to scale.

Experimentally, for a tensile load of 8 mN, a net elongation of 140 μm was measured. We use this simplified analysis, to estimate the individual contributions from the fibril, the backing layer and the DEA on overall deformation.

I. Deformation of the Pillar

Applied tensile force, $F_T = 8 \times 10^{-3} \text{ N}$

Initial Length of the fibril, $L_P = 1.6 \times 10^{-3} \text{ m}$

Area of cross-section of the pillar is given by A_P

$$A_P = \pi r^2 = \pi \times 355 \times 10^{-6} \text{ m} \times 355 \times 10^{-6} \text{ m}$$

Young's Modulus of Sylgard 184, $Y_P = 2.8 \times 10^6 \text{ Pa}$

The deformation in the fibril length, D_P

$$D_P = \frac{F_T}{A_P} \times \frac{L_P}{Y_P}$$

B. 6

And $D_P = 11.55 \mu\text{m}$

$$\text{Strain in the Fibril} = \frac{\text{elongated length} - \text{initial length}}{\text{initial length}} = \frac{\Delta l}{l_0}$$

($D_P \stackrel{\text{def}}{=} \Delta l$)

$$= (1611.55 \mu\text{m} - 1600 \mu\text{m}) / 1600 \mu\text{m} = 0.0072 \approx 0.7 \%$$

B. 7

This is a small deviation for elastomeric materials.

II. Deformation of the DEA-membrane

A periodic section of the DEA with the movable bar is shown in Figure 59a. Deformation in the DEA is calculated by assuming the contribution arising from the electrodes and the sandwiched layer surrounding it (marked by area A_1 and A_2). For the purpose of simplification, only the contributions from the area A_1 and A_2 are considered.

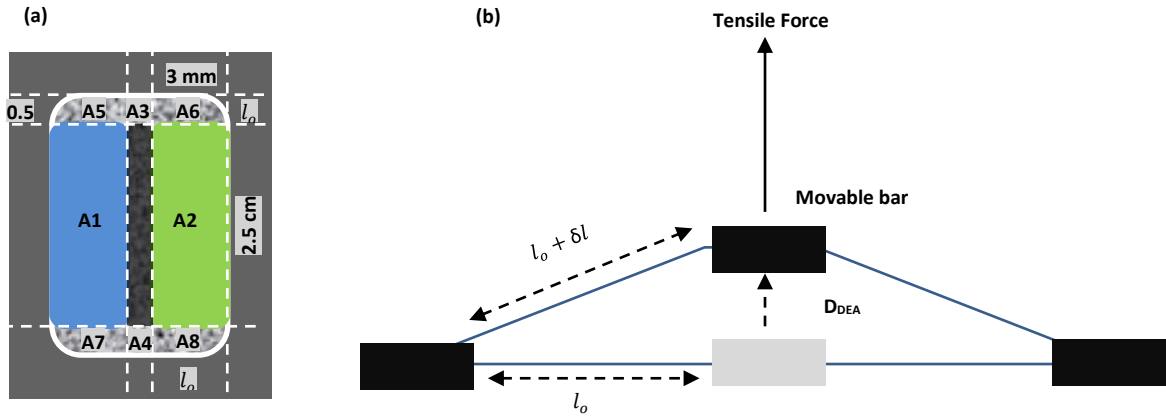


Figure 59 (a) Schematic showing one of the sections of the DEA with the movable bar. Sections A1 and A2 represent the stack of electrodes. Sections A3-A8 are the regions with the dielectric silicone. For the simplicity of the calculations, these areas have not been considered (b) Side view represents the elongation of the DEA under the tensile load. l_0 represents the membrane width of the region A1. The sketch is not drawn to scale.

The thickness of the dielectric membrane is unknown. Assuming a thickness of $50 \mu\text{m}$ which is typical of Elastosil films from Wacker, we assume that a biaxial pre-stretch of 20 % is applied. Owing to the incompressible nature of the elastomer, the volume will remain unchanged. Therefore, for an initial length (l_1), initial width (w_2) and initial thickness (t_1), the initial volume, V_i is given by

$$V_i = l_i \times w_i \times t_i \tag{B. 8}$$

After the pre-stretch, final length, $l_f = 1.2 l_i$, final width, $w_f = 1.2 w_i$

$$V_f = 1.2l_i \times 1.2w_f \times t_f \tag{B. 9}$$

Equating $V_i = V_f$

$$t_f = \frac{t_i}{1.44} \tag{B. 10}$$

The thickness of electrodes, t_{ele} is assumed to be $25 \mu\text{m}$ per electrode

$t_i = \text{thickness of 2 electrodes} + \text{thickness of the DEA membrane}$

$$t_i = 25 \times 2 \mu m + 50 \mu m$$

B. 11

Therefore, final thickness of the stack, t_3 , consisting of the electrodes with the silicone is t_f is given by

$$t_f = \frac{100}{1.44} \mu m = 69.44 \mu m$$

B. 12

*Area of the deformed membrane, $A_1 = \text{Membrane width} * \text{Membrane thickness}$*

$$\text{Membrane width} = 25 \times 10^{-3} m$$

$$\begin{aligned} A_1 = A_2 &= 25 \times 10^{-3} m \times 69.44 \times 10^{-6} m \\ &= 1736.11 \times 10^{-9} m^2 \end{aligned}$$

B. 13

$$\text{Total Area } A_{DEA} = 2A_1 = 2 \times 1736.11 \times 10^{-9} m^2 = 3472.22 \times 10^{-9} m^2$$

B. 14

$$\text{Net Stress, } \sigma = \frac{F_T}{A_{DEA}} = \frac{8 \times 10^{-3} N}{3472.22 \times 10^{-9} m^2} = 2.3 \times 10^3 \frac{N}{m^2}$$

B. 15

Strain in the DEA membrane,

$$\delta l = \frac{\text{Net Stress} \times \text{Initial Length}}{\text{Young's Modulus of the conductive electrodes}}$$

$$\delta l = \frac{\sigma * l_e}{Y_e}$$

B. 16

The Young's modulus for the conductive pads is assumed to be, $Y_e = 2.5 \times 10^6$ Pa. Initial length of the region A_1 , $l_e = 3 \times 10^{-3}$ m

$$\begin{aligned}\delta l &= \frac{2.3 \times 10^3 \text{ N/m}^2}{2.5 \times 10^6 \text{ N/m}^2} \times 3 \times 10^{-3} \text{ m} \\ &= 2.76 \times 10^{-6} \text{ m} = 2.76 \mu\text{m}\end{aligned}$$

B. 17

Strain in the direction of applied tensile load is given by D_{DEA} . Using Pythagoras theorem,

$$\begin{aligned}D_{DEA}^2 &= 3002.76^2 \mu\text{m}^2 - 3000^2 \mu\text{m}^2 \\ D_{DEA} &= 128.71 \mu\text{m}\end{aligned}$$

B. 18

III. Deformation of the Backing Layer

Finally, we calculate the deformation of the backing layer, D_{BL} .

Thickness of the Backing layer, $T_{BL} = 2 \times 10^{-3}$ m

Area of the Backing layer, $A_{BL} = 2 \times 3 \times 10^{-6}$ m²

Young's Modulus of Sylgard 184 = 2.8×10^6 Pa

$$D_{BL} = \frac{F_T * T_{BL}}{A_{BL} * Y_{BL}}$$

$$D_{BL} = \frac{8 \times 10^{-3} \text{ N} \times 2 \times 10^{-3} \text{ m}}{2 \times 3 \times 10^{-6} \text{ m}^2 \times 2.8 \times 10^6 \text{ N.m}^{-2}}$$

$$= 0.952 \mu m$$

B. 19

Thus, summing up the individual contributions of the deformations from the fibril, backing layer and the DEA, the net deformation accounts to $141.212 \mu m$. This is in good agreement with the experimentally measured value of $140 \mu m$. Qualitatively, with this simplified analysis, it can be concluded that the maximum deformation arises from the DEA.

IV. Peel Angle Under Tensile Loads

Under this scenario of tensile load, the elastomeric pillar undergoes elastic deformation. With maximum contraction at the center (half the pillar's length). As a result, the angle between the pillar and the substrate changes at the pillar's circumference. Simplified calculations are undertaken to evaluate the change in this angle defined as the peel angle within the present context.

Figure 60a shows the simplified version assuming the elongated pillar will be divided into two symmetrical truncated cones. The volume of the pillar will be equal to twice the volume of individual geometrical sections. In order to calculate the peel angle γ , the internal angle α is calculated.

Volume of the pillar is given by V_p ,

$$V_p = \pi \times r^2 \times L_p$$

$$V_p = 3.14 \times 355 \times 355 \times 1600 \times 10^{-9} mm^3$$

$$= 0.633 mm^3$$

B. 20

The volume of the truncated cone shown in Figure 60b is given by

$$V_{TC} = \frac{h \times \pi \times (r_1^2 + r_1 \times r_2 + r_2^2)}{3}$$

B. 21

Where,

$$\begin{aligned}
 h = AB &= \frac{\text{Length of the elongated pillar}}{2} \\
 &= \frac{1600 \mu\text{m} + 11.55 \mu\text{m}}{2} \\
 &= 805.75 \mu\text{m}
 \end{aligned}$$

B. 22

(derived from the calculations on pillar deformation).

$$2V_{TC} - V_P = 0$$

$$\frac{2h\pi}{3} \left[(r_1^2 + r_1r_2 + r_2^2) - \frac{3r_1^2L_P}{2h} \right] = 0$$

$$r_1^2 \left(1 - \frac{3L_P}{2h} \right) + r_1r_2 + r_2^2 = 0$$

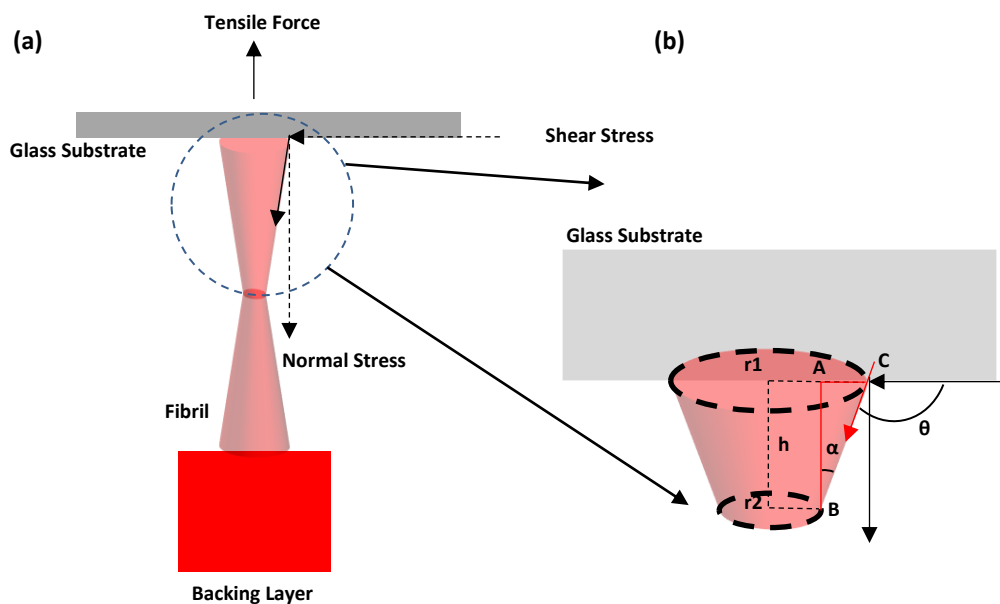


Figure 60 (a) A simple representation of the pillar under an applied tensile load. The pillar is assumed to be deformed into two symmetrical geometrical sections (b) Schematic shows the

zoomed in version of the top section in contact with glass. The peel angle is analysed when the pillar has been elongated.

$$(355^2 * 10^{-12} m^2) \left[1 - \frac{3 \times 1600 \times 10^{-6} m}{2 \times 805.75 \times 10^{-6} m} \right] + 355 \times 10^{-6} \times r_2 + r_2^2 = 0$$

$$r_2 = \frac{-355 * 10^{-6} m \pm \sqrt{((355 \times 10^{-6})^2 m^2 + 4 \times (249397 * 10^{-12}) m^2)}}{2}$$

$$r_2 = \frac{705}{2} \mu m = 352.5 \mu m$$

B. 23

Therefore,

$$AC = r_1 - r_2 = 355 - 352.5 \mu m = 2.5 \mu m$$

B. 24

and

$$\begin{aligned} \alpha &= \tan^{-1} \left(\frac{AC}{AB} \right) = \tan^{-1} \left(\frac{2.5}{805.75} \right) \\ &= \tan^{-1}(0.0031) = 0.177^\circ \end{aligned}$$

B. 25

These calculations for a fibril under tensile loads show that the pillar undergoes elongation with maximum contraction at the center of the fibril and thus also change the angle (*by* $\approx 0.18^\circ$) it makes with the glass object at the circumference even before the DEA has been switched on. Lastly, as shown in Figure 61b, once the pillar is elongated under an applied tensile load, switching on the DEA further elongates the pillar. The peel angle defined by the maximum angle the pillar makes with the glass substrate further grows, and this leads to a relatively faster release time for the contact to completely peel off as opposed to scenario without any applied tensile load.

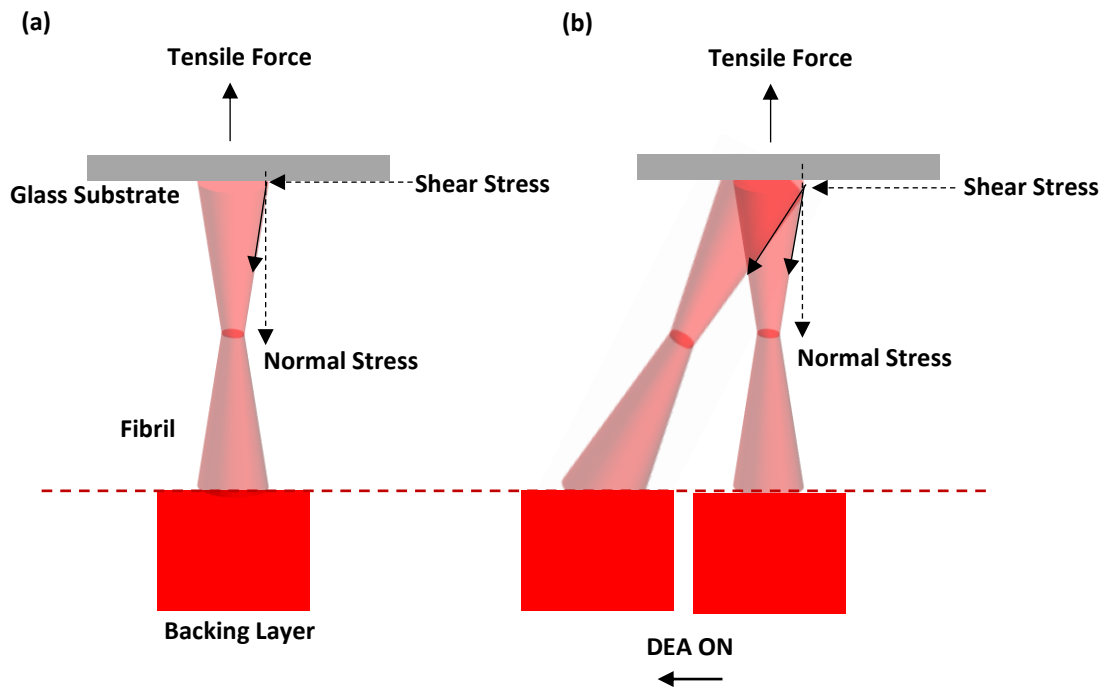


Figure 61 (a) Schematic represents the elongated pillar under an applied tensile load (b) Schematic depicting an elongated pillar which starts to peel once the DEA is switched on, due to the torque that acts at the interface resulting in the pillar to bend. Under a tensile load, the contact peels within few ms as compared to no tensile load.

List of Figures

Figure 1 Scanning electron micrographs of the toe pads of Gecko gecko (a) (b) Toe pads consist of hundreds of setae (ST represents a single seta) (c) Each seta is branched further in to sub micrometre spatula (SP). BR denotes the branches. Reproduced from [2] 4

Figure 2 Graph – Lennard Jones potential with interaction potentials $A = 10^{-77} \text{ J m}^6$ and $B = 10^{-134} \text{ J m}^{12}$. r_e is the equilibrium separation, where the force is zero and the energy is minimum. r_s is the point at which the two atoms separate spontaneously when pulled apart by the pull- off force, F_{max} . Reproduced from [22]..... 9

Figure 3 Parallel plate capacitor clamp configuration- Schematic representing an electrostatic chuck with the insulating layer of thickness r separating the backing electrode and the imperfectly flat wafer with a height h as a function of position . E_1 and E_2 represent the Electric fields in the insulator and wafer, respectively. This is a coulombic capacitive clamp. Reproduced from [26]. 10

Figure 4 Johnson Rahbek capacitive clamp configuration- Cross sectional view of the electroadhesion setup. Electrodes (blue) are embedded in a dielectric layer with thickness d and dielectric constant ϵ_1 . The target material has a dielectric constant ϵ_2 . A uniform air gap of width u separates the pad from the target. Reproduced from [29]. 11

Figure 5 Polarisation types in a linear dielectric material under a time-varying electric field Reproduced from [35]..... 13

Figure 6 Principle of Dielectrophoresis -Dielectric particles experience different forces in a non-uniform electric field due to different dielectric constants. Dielectrophoresis is the process used for particle separation. Reproduced from [41]..... 14

Figure 7 Schematic representing electroadhesion mechanism in an electrostatic chuck. Reproduced from [30]. 15

Figure 8 Micro aerial vehicle (MAV) design and operation (a) Schematic depicting the trajectory of the micro-aerial vehicle engaging with the target surface by means of electroadhesion (b) The aerial device consists of compliant copper electrodes coated on a polyimide film and covered by Parylene C. The entire structure is supported by a carbon fibre attached to a polyurethane foam mount that acts a damper in case of high velocity collisions and stabilises the device (c) An electroadhesive patch was designed using interdigitated electrodes and normal adhesion pressures were measured across different substrates with absolute values of surface asperities mentioned in the parenthesis. Reproduced from [13]..... 17

Figure 9 Theoretical and experimental results discussing the effect of electrode geometry on electroadhesion- (a) Four layer model of the electroadhesive pad consisting of interdigitated electrodes embedded in a dielectric layer [34] (b) Variation of parameter C for different normalised electrode width a/b when $h_1/b = 0.02$ and $\epsilon w = 5\epsilon_0$ (c) Simulation models of different electrode patterns [44] (d) Experimental results showing shear pressures measured for different electrode patterns on drywall, cedar and tile substrates [44]..... 19

Figure 10 Experimental validation of the relationship between the electroadhesive forces obtainable and spaces between the electrodes and its comparison with the theoretical results. Reproduced from [35].	20
Figure 11 Directional microwedges integrated with interdigitated electrodes -(a) Hybrid electroadhesive device with microwedges (b) Shear stress as a function of surface roughness. On roughness below 10 μm , all adhesive technologies perform closely. For surface roughness > 50 μm , hybrid device has highest adhesive pressures. Reproduced from [48].	22
Figure 12 Effect of Humidity on adhesion (a) The effect of relative humidity on electrostatic adhesion on wood. The adhesion pressure on plywood was found to increase with increasing relative humidity. Reproduced from [13] (b) Electroadhesive forces measured on the glass surface over a 5 day period corresponding to the fluctuations in relative humidity and temperature. Reproduced from [35].	23
Figure 13 Bi-layer electroadhesive design and effect of filler on roughness (a) The electroadhesive device had a bi- layer design where the high voltage electrodes were separated from the ground electrodes with a Kapton sheet. (b) AFM images of the Cu-Pc (Copper Phthalocyanine doped elastomeric samples for different weight concentration ratios. The surface roughness RMS varies directly with the dopant's concentration. Reproduced from [47].	24
Figure 14 Shear stress measurements for a flat doped dielectric layer. Shear stresses measured on a medium density fibreboard (MDF) for an unstructured bi-layer electroadhesive structure with increasing weight concentration of Copper (II) Pthalocyanine Cu-Pc particles. Reproduced from [47].	25
Figure 15 Shear stress measurements of doped and undoped bi- layer electroadhesives- Shear stress measurements on medium density fibre board and drywall substrates (a)R1 is the reference undoped micropatterned sample with Sylgard 184 and C1 is the doped micropatterned sample (b) Sylgard 170 microstructured undoped sample is the reference R2 and C2 is the doped Sylgard 170 sample (c) Reference undoped Sylgard 184 sample is compared to doped microwedges sample R3. Reproduced from [47].	26
Figure 16 Shear stress measurements for conductive micropatterned adhesives (a) Scanning electron microscope image of conductive carbon black filled PDMS microstructures (b) The increase in shear strength on drywall, polypropylene and polymethacrylate substrates at an electrical potential of 2 kV (c) Concept for using microstructures as electrodes in an electroadhesive device. Reproduced from [31].	27
Figure 17 Bi- layer structure of micropatterned electroadhesive using(a) Non- directional structures (b) Directional microwedges. Reproduced from [47].	28
Figure 18 Model design for a micropatterned electroadhesive pad(a) Schematic representation of an electroadhesive pad with artificial hairs mimicking gecko structures (shown in blue). Reproduced from [34].	29
Figure 19 Different gripping technologies depending on the object types. Reproduced from [50].	30

Figure 20 Fabrication and working of a photo-controllable and a pneumatic adhesive system -(a) The photo-controllable device consists of a crosslinked azo-benzene containing liquid crystalline elastomer unit. At 50 μm , UV light illumination causes the device to expand and contact the glass sphere. UV driven preload is measured. When the illumination is switched off, the device contracts and detaches from the glass sphere. (b) Photo-isomerisation leads to change in shape of the azobenzene units leading to loss of contact area Reproduced from [56] (c) Fibrillar adhesive device holding a 12.7 mm in diameter steel ball with complete and reduced contact area (d) (i – vi) depict the movement of different pillars once the device is inflated. When the device is fully inflated, only pillars at the centre are in contact, Modulating the air pressure enables the device to handle flat and curved surfaces. Reproduced from [54] 31

Figure 21 Operating principle of an electrostrictive polymer actuator. Reproduced from [60] 33

Figure 22 Different approaches for fabricating compliant electrodes: (a) Loose carbon powders applied on the elastomeric layer, (b) Carbon particles suspended in the viscous oil, (c) Conductive silicone composite by doping carbon particles, (d) Photolithographically patterned metallic electrodes, (e) Metallic electrodes deposited on a pre stretched membrane. Releasing the membrane leads to out of plane buckling (f). Reproduced from [66]..... 34

Figure 23 Parametric space for making conductive inks (a) Schematic representing the percolation threshold for conductive fillers as a function of filler concentration (b) Parameter space for conductive injectable inks for DEA applications. Reproduced from [66]..... 35

Figure 24 Torsional DMTA results of silicone DC 3481 and acrylic VHB 4910 elastomers. Reproduced from [72]..... 37

Figure 25 Schematic overview of the silicone dielectric elastomeric materials. Reproduced from [73]. 38

Figure 26 Instabilities in a dielectric actuator undergoing deformation in an applied electric field. Under an applied voltage, the dielectric elastomer fails at the pull-in instability at λ_c or snaps to a thinner state near λ_{lim} . Reproduced from [76]..... 39

Figure 27 Actuator Configurations: Stack or contractive actuator and membrane or expanding actuator. Reproduced from [77]..... 40

Figure 28 (a), (b) Layerwise composite structure of the stack DEA and its fabrication process. It is composed of alternating electrode and DE film layers. Reproduced from [77] (b-h) Fabrication process of stack DEA.(c) The mold for the micropatterns is filled with uncured silicone (d) Thermal curing of elastomer (e) The electrodes are spray coated (f) followed by spin coating of the subsequent dielectric layer (g) Thermal curing of the elastomer layer (h) the process is repeated until the desired number of layers have been stacked. Reproduced from [80]. 41

Figure 29 Stack actuator integrated with micropatterned adhesive layer (a) The prototype for stack actuator integrated with micropatterned structures. (b) Experimental set up to test the handling of the glass wafer using the stack DEA. Reproduced from [80]. 42

Figure 30 Design and operation of a device gripping via electroadhesion and releasing via use of out of plane actuation of a DEA (a) Square wave frequency from 1 to 60 Hz with applied voltages ranging from 3.5 kV to 6 kV (b) Release period without DEA oscillator (blue) and with DEA oscillator (red) (c) Oscillation profile at 8 Hz (d) Oscillation profile at 20 Hz (e) Oscillation profile at 55 Hz (f) Electroadhesive gripping mode (g) DEA release mode (h) Selectively engaging the electroadhesive and DEA oscillatory mode for handling of Kapton film. Reproduced from [87] 43

Figure 31 Schematic showing the position of fibres in a bi layer actuator and pick and place by controlling the bending direction (a) Finite element simulations of a bi layer structure consisting of a passive elastomer sheet bonded to a voltage actuated elastomer ($L/H = 25$, fibre width and heights ($H/10$). The lower image shows the cross-sectional view showing the location of the fibre and the bending moment (b) and (c) Handling of curved and soft materials by uniaxially bending the DEA. Reproduced from [63]..... 45

Figure 32 Structure and working of a compliant vertical gripper (a) The DEA part of the gripper consists of pre-stretched DEA bonded to passive layers. At 0 V, the structure is curled up and on applying Voltage across the top and bottom layers, uncurls the DEA to a flat configuration (b) Same voltage is applied between the top and bottom electrodes but these are laterally offset so that there is a high electric field normal to the membrane and strong fringe fields at the boundaries as shown by the arrows. Reproduced from [46] 46

Figure 33 Pick and place of micro-objects using a soft nanocomposite electroadhesive device (a) Schematic of the pull off measurement system using a colloidal AFM having a Pt coated spherical tip. Inset shows the Pt coated tip (b) Force displacement curves without (red) and with (blue) applied voltage (c) A micro pick and place map for the target object range at 30 V and 100 V. Reproduced from [90] 48

Figure 34 The micropatterned-electro adhesive device. (a) Illustration of the basic set-up. A micropatterned adhesive film was generated via replica molding and, subsequently, deposited on the interdigitated comb electrodes. (b) Schematic of the adhesion test setup. During the test a spherical glass probe was attached (approach) and detached (retraction) at different applied voltages. Normal forces F and displacements u were recorded. (c) Scanning electron micrograph of the micropatterned-electro adhesive device. The inset..... 54

Figure 35 Electroadhesion results. (a) Force-displacement curves for 0 kV (black) and 1.8 kV (red). Positive and negative forces are compressive and tensile forces, respectively. The inset presents data close to the contact of the probe with the micropatterned adhesive film. Arrows indicate the path during approach and retraction. (b) Pull-off forces in terms of net preloads for various applied voltages. Dashed lines highlight data for constant indentations. (c) Pull-off force (solid squares) and pull-off stress (open circles) as function of the applied voltage. The solid and the dashed lines illustrate quadratic and linear functions, respectively. (d) Net preload as function of the applied voltage. Numbers present the indentation into the micropatterned adhesive. 56

Figure 36 Models for the electric field-dependence of the air conductivity (see eq. 3. 5). Solid lines vary the slope sL for threshold value $Ec = 3$ MV/m, dashed lines vary Ec for $sL = 1$ $\mu\text{m}/\text{V}$. The dash-dotted red line was found to match experimental results with $Ec = 14.4$ MV/m and $sL =$

5 $\mu\text{m}/\text{V}$. Blue symbols are extracted from measurements of Carlon for moist air (RH = 66 %) [130].
 60

Figure 37 Schematic illustration of the computational model. (a) Cross-section ($y = 0$ plane) of the glass lens (purple, curvature radius rL) placed above oppositely charged electrodes (red and blue stripes) located on a ceramic substrate (grey). The electrode array is covered with a thin elastomer layer with thickness he . The patterned surface is approximated by a thin homogenous effective medium layer with thickness hp . (b) In the simulations, a cuboidal quarter of the experimental setup is considered, with a symmetry plane at $y = 0$ and an antisymmetry plane at $x = 0$ 62

Figure 38 Distribution of electroadhesion: Logarithmic Maxwell stress map on the surface of the lens located 1 μm above the micropatterned electro-adhesive device. The white lines indicate the shape and location of the electrode array. 64

Figure 39 Numerical results of electroadhesion force as function of applied voltage: The variable air conductivity was calculated according to eq. 3. 5 with threshold value Ec and slope sL (compare Figure 36). Black circles represent experimental results. The dashed black line assumes constant air conductivity. The dash-dotted black line corresponds to the electrostatic model. 65

Figure 40 Comparison of numerical models, effect of air conductivity and of electric parameters on electroadhesive force Fes . (a) Comparison of the surface and bulk conductivity models: Fes in terms of the field-independent surface (σs , blue crosses) or bulk (σ , red circles) conductivity of the lens. Solid blue and red dashed lines are fits based on the logistic function, compare eq. 3. 9. In the bulk conductivity model, the fitted function crosses zero force for a lens conductivity equal to that of air (dashed grey line). (b) Electroadhesive force as a function of air conductivity (σ_{air} , red circles) and elastomer conductivity (σe , blue squares). (c) Electroadhesive force as a function of lens permittivity (ϵL , brown squares) and elastomer permittivity (ϵe , violet circles). (d,e) Electroadhesive force in terms of (d) the size of the electrode array wa and (e) the thickness of the elastomer film he for linearly varying air conductivity (red stars, $Ec = 3 \text{ MV}/\text{m}$ and $sL = 1 \mu\text{m}/\text{V}$), field-independent air conductivity (orange pluses) and in the electrostatic model (blue circles). The lines in (e) represent exponential fits to the three thickest films of each data set. As a reference, the green diamonds in (b-e) represent the parameter values stated in Table 1. 67

Figure 41 DEA design and working principle: (a) Top view of the linear actuator. Top and bottom electrodes are shown in green and blue sections. Red dot marks the micropillar with mushroom tip. (b) Cross-section view of an unbiased DEA-micropillar assembly. (c) $V1$ is biased causing the green sections II, IV and VI to compress in the thickness direction. Net movement to the left as shown by the direction of the arrow. (d) Biasing the electrode $V2$ and $V1$ ($V2 = V1$) results in compression of the blue sections I, III and V and net displacement occurs towards the right. 73

Figure 42 Schematic of the experimental setup for studying the detachment mechanism. Cross-section view depicts a section of the DEA with the micropillar attached to the central movable bar. Glass substrate connected to a linear stage is brought in contact with micropillar and a preload is applied. The substrate is retracted to the touch point, followed by switching on the DEA (biasing the green electrodes). In this image, the fibril gets sheared to the left resulting in a peel front at top right edge. 75

Figure 43: Control experiments (a) Characterisation of the DEA with the microstructure (red curve) showing the voltage dependent in-plane displacement. (b) Pull off force is independent of the applied preload. 76

Figure 44 Optical images of the side view showing the pillar bending under shear induced torque (a) The micropillar is in contact with the target glass substrate. (b) Target attached to the linear drive is retracted to the point of zero compressive force. (c) A bias of 1.1 kV is applied, and the DEA displaces to the left as shown by the arrow. The backing layer and the stalk displaces while the tip is still in contact with the glass surface. (d) Target substrate is retracted after the bias was applied for 1 s. 78

Figure 45 Adhesion measurements on an unbiased (a,b) and biased (c-f) DEA-microstructure assembly. Green bands represent the compressive regime, blue bands indicate the tensile region and grey bands in the force time curves illustrate the hold time duration for which the electrical bias was applied (a) Force displacement curve at 0V. A preload of 3 mN was applied for 1s and the measured pull of force is 12 mN. (b) Force-time curve at 0V. (c) Force displacement curve with 1.1 kV applied for 5s. Pull off force is 7 mN. (d) Force time curve showing the green region during which the crack is growing however at the end of 5s, target is retracted and the residual adhesion of 7 mN is measured marked by the blue band. (e) Force displacement shows complete loss of adhesion when the bias is applied for 12s. Arrows mark the approach and retraction phases in the measurement. (f) Force- time curve shows that during the time period of 12 s when the bias was turned on, the crack fully peels from one edge to the other and the force drops to zero. Absence of blue band show that adhesion was lost solely by the shear-force due to DEA..... 80

Figure 46 Effect of varying bias on Peel time (a) Decay in pull-off stress was measured at bias of 1 kV, 1,1 kV and 1.2 kV with increasing time duration of applied bias and the time taken for the contact to fully peel off was measured. (b) Work of separation also shows similar trends as the pull-off stress for the corresponding bias. 82

Figure 47 Effect of hold time on crack growth (a) Force time curve showing the crack propagation at a bias of 1.1 kV, applied for 15s. (b-e) Optical images show the top view of the contact.(b) High contrast shows that the tip is in contact with the glass surface.(c,d) Crack initiates at the edge opposite to the direction of the applied shear force as shown by the direction of the arrow.(e) Complete loss of contrast shows the contact has completely peeled off. Dotted lines in yellow mark the edge of the displaced backing layer in the background when the bias was switched on. 83

Figure 48 Crack growth in a fibril with a prescribed center crack (a) Top view shows a fibril in contact with the target substrate (dark circle). The bright spot in the center arises from a center crack where contact to the substrate is lost. Dotted white lines mark the edge of the backing layer. (b-e) Backing layer corner displaces out of the view of the image when the bias is on. An additional crack originates at the edge and the center crack fuses with the propagating edge crack. Loss of contrast in (h) shows that the crack has peeled completely..... 86

Figure 49 Force time curves for axially elongated pillars when subjected to bias at elongations of (a) 15 μm (b) 30 μm and (c) 140 μm . The detachment time was found to be reduced due to high tensile stresses acting along the fibril. 87

Figure 50 Schematic showing an elongated fibril bending due to shear-induced torque (a) Schematic showing the micropillar integrated with the dielectric elastomeric actuator on the movable bar. It is in contact with the glass substrate (b) Zoomed in view depicting the micropillar with the backing layer and the movable bar. (c) Zoomed in view showing micropillar under deformation once the DEA is biased. Arrows mark the direction of lateral displacement. The figures are not drawn to scale and present only a simplified view of the fibril with the backing layer displaced due to the action of dielectric actuator. (d) With time, the peel front at the interface starts to grow..... 88

Figure 51 Dependence of the electroadhesion force on the a/b ratio for $\delta = 1 \mu\text{m}$ and $V_0 = 2 \text{ kV}$. Blue points are for $E_c = 3 \text{ MV/m}$ and $sL = 1 \mu\text{m/V}$ 95

Figure 52 Illustration of the periodic numerical model geometry. (a) Realistic representation of the hexagonal pillar array. (b) Pillar array layer represented by an effective medium approximation. (c) Model with no pillar array or effective medium..... 96

Figure 53 Comparison of the non-dimensional electroadhesion stress $\sigma_{ad}\sigma_0$ (a) as a function of the permittivity ratio $\epsilon_c\epsilon_w$ of the cover and the wall, respectively, for three values of ab and (b) as a function of ab for three values of δb . Blue symbols represent our results, solid lines those of [47]... 97

Figure 54 Comparison of the non-dimensional electroadhesion stress $\sigma_{ad}\sigma_0$ (a) as a function of the permittivity ratio $\epsilon_c\epsilon_w$ of the cover and the wall, respectively, for three values of ab and (b) as a function of ab for three values of δb . Blue symbols represent our results, solid lines those of Cao et al., 2016..... 98

Figure 55 (a) Average electroadhesive pressure considering realistic pillar array geometry (dashed orange lines) and an effective medium approximation (solid blue lines) as a function of air gap thickness δ . Both lines overlap and converge to an exponential function (grey dotted line). (b) Ratio of the two extracted pressures as a function of δ . At $\delta = 1 \mu\text{m}$ the effective medium approximation underestimates the pressure by around 2%..... 98

Figure 56 Logarithmic pseudocolor maps of the electroadhesion pressure for different electrode array shapes represented by the faint white lines, when $\delta = 1 \mu\text{m}$ and $V_0 = 2 \text{ kV}$. (a) Realistic electrode geometry including horizontal electrode segments. (b) Assuming a symmetry plane at $y = 0$ and an antisymmetry plane at $x = 0$ (dashed white lines). (c) Infinite array, derived from the periodic unit cell model..... 100

Figure 57 Simplified schematic of the pillar deformation during shearing and pulling: Scenario 1 (a) Schematic showing the fibril at its original position with no compressive or tensile force. (b) DEA is switched on resulting in lateral displacement of the fibril and beginning of an edge crack due to peeling at the interface under the influence of a shear-induced torque. Scenario 2 (c) Before switching on the DEA, a tensile load is applied to the fibril. A simplified sketch illustrates the pillar as divided in two symmetric truncated cones (d) DEA is switched on. The pillar, backing layer and DEA as a whole deform (elongate) more in comparison to scenario 1. The pillar deformation is highly simplified, and the Poisson contraction is exaggerated..... 102

Figure 58 Schematic representing the scenario when a tensile load is applied to the fibril. All the components comprising the fibril, the backing layer and the DEA membrane undergo deformation.

The angle of deformation is exaggerated for the purpose of understanding and the figure is not drawn to scale. 103

Figure 59 (a) Schematic showing one of the sections of the DEA with the movable bar. Sections A1 and A2 represent the stack of electrodes. Sections A3-A8 are the regions with the dielectric silicone. For the simplicity of the calculations, these areas have not been considered (b) Side view represents the elongation of the DEA under the tensile load. l_0 represents the membrane width of the region A₁. The sketch is not drawn to scale. 105

Figure 60 (a) A simple representation of the pillar under an applied tensile load. The pillar is assumed to be deformed into two symmetrical geometrical sections (b) Schematic shows the zoomed in version of the top section in contact with glass. The peel angle is analysed when the pillar has been elongated. 109

Figure 61 (a) Schematic represents the elongated pillar under an applied tensile load (b) Schematic depicting an elongated pillar which starts to peel once the DEA is switched on , due to the torque that acts at the interface resulting in the pillar to bend. Under a tensile load, the contact peels within few ms as compared to no tensile load. 111

References

- [1] Aristotle, *Historia Animalium*, trans. Thompson, D. A. W. (1918) (Clarendon, Oxford), http://classics.mit.edu/Aristotle/history_anim.html.
- [2] E.Arzt, S.Gorb, and R. Spolenak, "From micro to nano contacts in biological attachment devices," *Proc. Natl. Acad. Sci.* 100(19), 10603-10606., 2003.
- [3] Gao, Huajian, Xiang Wang, Haimin Yao, Stanislav Gorb, and Eduard Arzt. "Mechanics of hierarchical adhesion structures of geckos." *Mechanics of Materials* 37, no. 2-3 (2005): 275-285.
- [4] Bartlett, Michael D., Andrew B. Croll, Daniel R. King, Beth M. Paret, Duncan J. Irschick, and Alfred J. Crosby. "Looking beyond fibrillar features to scale gecko-like adhesion." *Advanced Materials* 24, no. 8 (2012): 1078-1083.
- [5] Bartlett, Michael D., and Alfred J. Crosby. "High capacity, easy release adhesives from renewable materials." *Advanced materials* 26, no. 21 (2014): 3405-3409.
- [6] E. Arzt, "Biological and artificial attachment devices : Lessons for materials scientists from flies and geckos," *Mater. Sci. Eng. C*, 26(8), 1245-1250, vol. 26, pp. 1245–1250, 2006, doi: 10.1016/j.msec.2005.08.033.
- [7] C. Kittel, *Introduction to Solid State Physics*, Eighth edition.
- [8] G. Monkman, "An analysis of astrictive prehension.," *Int. J. Robot. Res.* 16(1), 1-10., 1997.
- [9] Guo, Jianglong, Mitul Tailor, Thomas Bamber, Matthew Chamberlain, Laura Justham, and Michael Jackson. "Investigation of relationship between interfacial electroadhesive force and surface texture." *Journal of Physics D: Applied Physics* 49, no. 3 (2015): 035303.
- [10] Drotlef, Dirk-Michael, Peter Blümler, and Aránzazu del Campo. "Magnetically actuated

- patterns for bioinspired reversible adhesion (dry and wet)." *Advanced Materials* 26, no. 5 (2014): 775-779.
- [11] Kizilkan, Emre, Jan Strueben, Anne Staubitz, and Stanislav N. Gorb. "Bioinspired photocontrollable microstructured transport device." *Sci. Robot* 2, no. 2 (2017).
- [12] B. A. Zhenyi, M., Scheinbeim, J. I., Lee, J. W., & Newman, "High field electrostrictive response of polymers.," *J. Polym. Sci. Part B Polym. Physics*, 32(16), 2721-2731., pp. 2721–2731, 1994.
- [13] A. F. Devonshire, "Theory of ferroelectrics," *Adv. physics*, 3(10), 85-130., vol. 8732, 1954.
- [14] V. Alizadehyazdi, M. Modabberifar, S. M. J. Mahmoudzadeh, and M. Spenko, "Electrostatic self-cleaning gecko-like adhesives," *J. R. Soc. Interface*, 15(141), 20170714., 2018.
- [15] J. R. Napier, "The prehensile movements of the human hand," *J. Bone Joint Surg. Br.*, vol. 38-B, no. No. 4, 1956.
- [16] L. Kniese, "Europäische patentanmeldung 04.10.2000," 2000.
- [17] W. Crooks, "Fin ray ® effect inspired soft robotic gripper : From the robosoft grand challenge toward Optimization," *Front. Robot. AI* 3 70., vol. 3, no. November, pp. 1–9, 2016
- [18] H. Peisker, J. Michels, and S. N. Gorb, "Evidence for a material gradient in the adhesive tarsal setae of the ladybird beetle *Coccinella septempunctata*," *Nat. Commun.* 4(1), 1-7., 2013.
- [19] W. Federle, W. J. P. Barnes, W. Baumgartner, P. Drechsler, and J. M. Smith, "Wet but not slippery : boundary friction in tree frog adhesive toe pads," *J. R. Soc. Interface*, 3(10), 689-697., vol. 3, no. May, 2006.
- [20] Autumn, Kellar, Metin Sitti, Yiching A. Liang, Anne M. Peattie, Wendy R. Hansen, Simon Sponberg, Thomas W. Kenny, Ronald Fearing, Jacob N. Israelachvili, and Robert

- J. Full. "Evidence for van der Waals adhesion in gecko setae." *Proceedings of the National Academy of Sciences* 99, no. 19 (2002): 12252-12256.
- [21] Autumn, Kellar, Yiching A. Liang, S. Tonia Hsieh, Wolfgang Zesch, Wai Pang Chan, Thomas W. Kenny, Ronald Fearing, and Robert J. Full. "Adhesive force of a single gecko foot-hair." *Nature* 405, no. 6787 (2000): 681-685.
- [22] Huber, Gerrit, Hubert Mantz, Ralph Spolenak, Klaus Mecke, Karin Jacobs, Stanislav N. Gorb, and Eduard Arzt. "Evidence for capillarity contributions to gecko adhesion from single spatula nanomechanical measurements." *Proceedings of the National Academy of Sciences* 102, no. 45 (2005): 16293-16296.
- [23] Autumn, K., A. Dittmore, D. Santos, M. Spenko, and M. Cutkosky. "Frictional adhesion: a new angle on gecko attachment." *Journal of Experimental Biology* 209, no. 18 (2006): 3569-3579.
- [24] Autumn, K., S. T. Hsieh, D. M. Dudek, J. Chen, C. Chitaphan, and R. J. Full. "Dynamics of geckos running vertically." *Journal of experimental biology* 209, no. 2 (2006): 260-272.
- [25] S. Y. U. Shapoval, "Microfabricated adhesive mimicking gecko foot-hair," *Nat. Mater.* 2(7), 461-463., 2003.
- [26] Y. Wang, V. Kang, E. Arzt, W. Federle, and R. Hensel, "Strong Wet and Dry Adhesion by Cupped Microstructures," *ACS Appl. Mater. interfaces*, 11(29), 26483-26490., 2019.
- [27] Graule, M. A., P. Chirarattananon, S. B. Fuller, N. T. Jafferis, K. Y. Ma, Matthew Spenko, Roy Kornbluh, and R. J. Wood. "Perching and takeoff of a robotic insect on overhangs using switchable electrostatic adhesion." *Science* 352, no. 6288 (2016): 978-982.
- [28] Ji, Xiaobin, Xinchang Liu, Vito Cacucciolo, Matthias Imboden, Yoan Civet, Alae El Haitami, Sophie Cantin, Yves Perriard, and Herbert Shea. "An autonomous untethered fast soft robotic insect driven by low-voltage dielectric elastomer actuators." *Science Robotics* 4, no. 37 (2019).

- [29] [www. and Festo.com/group/en/cms/12745.htm](http://www.festo.com/group/en/cms/12745.htm), “Festo Co. Ltd., OctopusGripper | Festo Corporate,” 2017.
- [30] C. Greiner and E. Arzt, “Contact Shape Controls Adhesion of Bioinspired Fibrillar Surfaces,” *Langmuir*, 23(20), 10235-10243., vol. 4, no. 25, pp. 10235–10243, 2007.
- [31] Balijepalli, R. G., M. R. Begley, N. A. Fleck, R. M. McMeeking, and E. Arzt. "Numerical simulation of the edge stress singularity and the adhesion strength for compliant mushroom fibrils adhered to rigid substrates." *International Journal of Solids and Structures* 85 (2016): 160-171.
- [32] S. C. L. Fischer, E. Arzt, and R. Hensel, “Composite Pillars with a Tunable Interface for Adhesion to Rough Substrates,” *ACS Appl. Mater. interfaces*, 9(1), 1036-1044., 2017.
- [33] Bacca, Mattia, Jamie A. Booth, Kimberly L. Turner, and Robert M. McMeeking. "Load sharing in bioinspired fibrillar adhesives with backing layer interactions and interfacial misalignment." *Journal of the Mechanics and Physics of Solids* 96 (2016): 428-444.
- [34] J. A. Booth, M. Bacca, R. M. McMeeking, and K. L. Foster, “Benefit of Backing-Layer Compliance in Fibrillar Adhesive Patches — Resistance to Peel Propagation in the Presence of Interfacial Misalignment,” *Adv. Mater. Interfaces*, 5(15), 1800272., 2018.
- [35] M. Mengüç, Y., Röhrig, M., Abusomwan, U., Hölscher, H., & Sitti, “Staying sticky : contact self-cleaning of gecko-inspired adhesives,” *J. R. Soc. Interface* 11, no. 94 20131205, 2014.
- [36] J. N. Israelachvili, *Intermolecular and Surface Forces*. 2009.
- [37] A. Coulomb, “Histoire de l’Académie [royale] des sciences avec les mémoires de mathématiques et de physique, partie ‘Mémoires’ [1785] , 1788,” *A Source B. Physics*, 408-413, 1935.
- [38] Lennard-Jones, John Edward, and John Anthony Pople. "The molecular orbital theory of chemical valency. IV. The significance of equivalent orbitals." *Proceedings of the Royal Society of London. Series A. Mathematical and Physical Sciences* 202, no. 1069 (1950): 166-180.

- [39] Johnsen, Alfred, and Knud Rahbek. "A physical phenomenon and its applications to telegraphy, telephony, etc." *Journal of the Institution of Electrical Engineers* 61, no. 320 (1923): 713-725.
- [40] G. A. Wardly, "Electrostatic Wafer Chuck for Electron Beam Microfabrication Electrostatic Wafer Chuck for Electron Beam Microfabrication," *Rev. Sci. Instruments*, 44(10), 1506-1509., 1973.
- [41] K. Asano, F. Hatakeyama, and K. Yatsuzuka, "Fundamental study of an electrostatic chuck for silicon wafer handling," *IEEE Trans. Ind. Appl.*, vol. 38, no. 3, pp. 840–845, 2002.
- [42] Van Elp, J., P. T. M. Giesen, and A. M. M. De Groof. "Low-thermal expansion electrostatic chuck materials and clamp mechanisms in vacuum and air." *Microelectronic engineering* 73 (2004): 941-947.
- [43] Persson, Bo NJ, and Jianglong Guo. "Electroadhesion for soft adhesive pads and robotics: theory and numerical results." *Soft matter* 15, no. 40 (2019): 8032-8039.
- [44] Yatsuzuka, Kyoko, Fumikazu Hatakeyama, Kazutoshi Asano, and Shinichiro Aonuma. "Fundamental characteristics of electrostatic wafer chuck with insulating sealant." *IEEE Transactions on Industry Applications* 36, no. 2 (2000): 510-516.
- [45] Krahn, Jeffrey, and Carlo Menon. "Electro-dry-adhesion." *Langmuir* 28, no. 12 (2012): 5438-5443.
- [46] Germann, Jürg, Bryan Schubert, and Dario Floreano. "Stretchable electroadhesion for soft robots." In *2014 IEEE/RSJ International Conference on Intelligent Robots and Systems*, pp. 3933-3938. Ieee, 2014.
- [47] Persson, B. N. J. "The dependency of adhesion and friction on electrostatic attraction." *The Journal of chemical physics* 148, no. 14 (2018): 144701.
- [48] Cao, Changyong, Xiaoyu Sun, Yuhui Fang, Qing-Hua Qin, Aibing Yu, and Xi-Qiao Feng. "Theoretical model and design of electroadhesive pad with interdigitated electrodes." *Materials & Design* 89 (2016): 485-491.

- [49] Guo, Jianglong, Thomas Bamber, Matthew Chamberlain, Laura Justham, and Michael Jackson. "Optimization and experimental verification of coplanar interdigital electroadhesives." *Journal of Physics D: Applied Physics* 49, no. 41 (2016): 415304.
- [50] McMeeking, Robert M., and Chad M. Landis. "Electrostatic forces and stored energy for deformable dielectric materials." (2005): 581-590.
- [51] Pohl, H. A., K. Pollock, and J. S. Crane. "Dielectrophoretic force: A comparison of theory and experiment." *Journal of Biological Physics* 6, no. 3-4 (1978): 133-160.
- [52] Endo, I., T. Nagamune, S. Katoh, and T. Yonemoto. "Separation of Dead Cells from Culture Broth by Using Dielectrophoresis." *Bioseparation Engineering* (2000): 53.
- [53] Gascoyne, Peter RC, and Jody Vykoukal. "Particle separation by dielectrophoresis." *Electrophoresis* 23, no. 13 (2002): 1973.
- [54] Endo, Isao, T. Nagamune, S. Katoh, and T. Yonemoto, eds. *Bioseparation engineering*. Elsevier, 2000.
- [55] Prahlad, Harsha, Ron Pelrine, Scott Stanford, John Marlow, and Roy Kornbluh. "Electroadhesive robots—wall climbing robots enabled by a novel, robust, and electrically controllable adhesion technology." In *2008 IEEE international conference on robotics and automation*, pp. 3028-3033. IEEE, 2008.
- [56] D. Ruffatto, J. Shah, and M. Spenko, "Increasing the adhesion force of electrostatic adhesives using optimized electrode geometry and a novel manufacturing process," *J. Electrostat.* 72(2), 147-155, vol. 72, pp. 147–155, 2014.
- [57] Ruffatto, Donald, Jainam Shah, and Matthew Spenko. "Optimization and experimental validation of electrostatic adhesive geometry." In *2013 IEEE Aerospace Conference*, pp. 1-8. IEEE, 2013.
- [58] Prahlad, Harsha, Ron Pelrine, Scott Stanford, John Marlow, and Roy Kornbluh. "Electroadhesive robots—wall climbing robots enabled by a novel, robust, and electrically controllable adhesion technology." In *2008 IEEE international conference on robotics and automation*, pp. 3028-3033. IEEE, 2008.

- [59] Shintake, Jun, Samuel Rosset, Bryan Schubert, Dario Floreano, and Herbert Shea. "Versatile soft grippers with intrinsic electroadhesion based on multifunctional polymer actuators." *Advanced Materials* 28, no. 2 (2016): 231-238.
- [60] Akherat, SM Javid Mahmoudzadeh, Mohammad Amin Karimi, Vahid Alizadehyazdi, Shokoufeh Asalzadeh, and Matthew Spenko. "A tunable dielectric to improve electrostatic adhesion in electrostatic/microstructured adhesives." *Journal of Electrostatics* 97 (2019): 58-70.
- [61] Ruffatto III, Donald, Aaron Parness, and Matthew Spenko. "Improving controllable adhesion on both rough and smooth surfaces with a hybrid electrostatic/gecko-like adhesive." *Journal of The Royal Society Interface* 11, no. 93 (2014): 20131089.
- [62] Parness, Aaron, Daniel Soto, Noé Esparza, Nick Gravish, Matt Wilkinson, Kellar Autumn, and Mark Cutkosky. "A microfabricated wedge-shaped adhesive array displaying gecko-like dynamic adhesion, directionality and long lifetime." *Journal of the Royal Society Interface* 6, no. 41 (2009): 1223-1232.
- [63] Shintake, Jun, Vito Cacucciolo, Dario Floreano, and Herbert Shea. "Soft robotic grippers." *Advanced Materials* 30, no. 29 (2018): 1707035.
- [64] Frensemeier, Mareike, Jessica S. Kaiser, Carl P. Frick, Andreas S. Schneider, Eduard Arzt, Ray S. Fertig III, and Elmar Kroner. "Temperature-Induced Switchable Adhesion using Nickel–Titanium–Polydimethylsiloxane Hybrid Surfaces." *Advanced Functional Materials* 25, no. 20 (2015): 3013-3021.
- [65] Drotlef, Dirk-Michael, Peter Blümler, and Aránzazu del Campo. "Magnetically actuated patterns for bioinspired reversible adhesion (dry and wet)." *Advanced Materials* 26, no. 5 (2014): 775-779.
- [66] Song, Sukho, Dirk-M. Drotlef, Jamie Paik, Carmel Majidi, and Metin Sitti. "Mechanics of a pressure-controlled adhesive membrane for soft robotic gripping on curved surfaces." *Extreme Mechanics Letters* 30 (2019): 100485.
- [67] Song, Sukho, and Metin Sitti. "Soft grippers using micro-fibrillar adhesives for transfer

- printing." *Advanced Materials* 26, no. 28 (2014): 4901-4906.
- [68] Song, Sukho, Dirk-Michael Drotlef, Carmel Majidi, and Metin Sitti. "Controllable load sharing for soft adhesive interfaces on three-dimensional surfaces." *Proceedings of the National Academy of Sciences* 114, no. 22 (2017): E4344-E4353.
- [69] Paretkar, Dadhichi, Marleen Kamperman, David Martina, Jiahua Zhao, Costantino Creton, Anke Lindner, Anand Jagota, Robert McMeeking, and Eduard Arzt. "Preload-responsive adhesion: effects of aspect ratio, tip shape and alignment." *Journal of the Royal Society Interface* 10, no. 83 (2013): 20130171.
- [70] Chiang Foo, Choon, Shengqiang Cai, Soo Jin Adrian Koh, Siegfried Bauer, and Zhigang Suo. "Model of dissipative dielectric elastomers." *Journal of Applied Physics* 111, no. 3 (2012): 034102.
- [71] Pelrine, Ron, Roy Kornbluh, Qibing Pei, and Jose Joseph. "High-speed electrically actuated elastomers with strain greater than 100%." *Science* 287, no. 5454 (2000): 836-839.
- [72] Pelrine, Ronald E., Roy D. Kornbluh, and Jose P. Joseph. "Electrostriction of polymer dielectrics with compliant electrodes as a means of actuation." *Sensors and Actuators A: Physical* 64, no. 1 (1998): 77-85.
- [73] Zhao, Xuanhe, and Zhigang Suo. "Electrostriction in elastic dielectrics undergoing large deformation." *Journal of Applied Physics* 104, no. 12 (2008): 123530.
- [74] Kornbluh, Roy D., Ron Pelrine, Jose Joseph, Richard Heydt, Qibing Pei, and Seiki Chiba. "High-field electrostriction of elastomeric polymer dielectrics for actuation." In *Smart Structures and Materials 1999: Electroactive Polymer Actuators and Devices*, vol. 3669, pp. 149-161. International Society for Optics and Photonics, 1999.
- [75] Shian, Samuel, Katia Bertoldi, and David R. Clarke. "Dielectric elastomer based "grippers" for soft robotics." *Advanced Materials* 27, no. 43 (2015): 6814-6819.
- [76] Henke, E-F. Markus, Samuel Schlatter, and Iain A. Anderson. "Soft dielectric elastomer oscillators driving bioinspired robots." *Soft robotics* 4, no. 4 (2017): 353-366.

- [77] Araromi, Oluwaseun A., Samuel Rosset, and Herbert R. Shea. "High-resolution, large-area fabrication of compliant electrodes via laser ablation for robust, stretchable dielectric elastomer actuators and sensors." *ACS applied materials & interfaces* 7, no. 32 (2015): 18046-18053.
- [78] Rosset, Samuel, and Herbert R. Shea. "Flexible and stretchable electrodes for dielectric elastomer actuators." *Applied Physics A* 110, no. 2 (2013): 281-307.
- [79] Rwei, S-P., F-H. Ku, and K-C. Cheng. "Dispersion of carbon black in a continuous phase: Electrical, rheological, and morphological studies." *Colloid and Polymer Science* 280, no. 12 (2002): 1110-1115.
- [80] Verplancke, Rik, Frederick Bossuyt, Dieter Cuypers, and Jan Vanfleteren. "Thin-film stretchable electronics technology based on meandering interconnections: fabrication and mechanical performance." *Journal of Micromechanics and Microengineering* 22, no. 1 (2011): 015002.
- [81] Bowden, Ned, Scott Brittain, Anthony G. Evans, John W. Hutchinson, and George M. Whitesides. "Spontaneous formation of ordered structures in thin films of metals supported on an elastomeric polymer." *Nature* 393, no. 6681 (1998): 146-149.
- [82] Benslimane, Mohamed, Hans-Erik Kiil, and Michael J. Tryson. "Electromechanical properties of novel large strain PolyPower film and laminate components for DEAP actuator and sensor applications." In *Electroactive Polymer Actuators and Devices (EAPAD) 2010*, vol. 7642, p. 764231. International Society for Optics and Photonics, 2010.
- [83] Michel, Silvain, Xuequn Q. Zhang, Michael Wissler, Christiane Löwe, and Gabor Kovacs. "A comparison between silicone and acrylic elastomers as dielectric materials in electroactive polymer actuators." *Polymer international* 59, no. 3 (2010): 391-399.
- [84] Madsen, Frederikke B., Anders E. Daugaard, Søren Hvilsted, and Anne L. Skov. "The current state of silicone-based dielectric elastomer transducers." *Macromolecular rapid communications* 37, no. 5 (2016): 378-413.

- [85] Hoffstadt, T., A. Koellnberger, and J. Maas. "Characterization of Enhanced Silicone Materials for Dielectric Elastomer Transducers." In *ACTUATOR 2018; 16th International Conference on New Actuators*, pp. 1-4. VDE, 2018.
- [86] Dünki, Simon J., Yee Song Ko, Frank A. Nüesch, and Dorina M. Opris. "Self-Repairable, High Permittivity Dielectric Elastomers with Large Actuation Strains at Low Electric Fields." *Advanced Functional Materials* 25, no. 16 (2015): 2467-2475.
- [87] Li, Bo, Hualing Chen, Junhua Qiang, Shulin Hu, Zicai Zhu, and Yongquan Wang. "Effect of mechanical pre-stretch on the stabilization of dielectric elastomer actuation." *Journal of Physics D: Applied Physics* 44, no. 15 (2011): 155301.
- [88] Kovacs, G., L. Düring, S. Michel, and G. Terrasi. "Stacked dielectric elastomer actuator for tensile force transmission." *Sensors and actuators A: Physical* 155, no. 2 (2009): 299-307.
- [89] Anderson, Iain A., Todd A. Gisby, Thomas G. McKay, Benjamin M. O'Brien, and Emilio P. Calius. "Multi-functional dielectric elastomer artificial muscles for soft and smart machines." *Journal of applied physics* 112, no. 4 (2012): 041101.
- [90] Kovacs, Gabor, and Lukas Düring. "Contractive tension force stack actuator based on soft dielectric EAP." In *Electroactive Polymer Actuators and Devices (EAPAD) 2009*, vol. 7287, p. 72870A. International Society for Optics and Photonics, 2009.
- [91] Grotepaß, T., J. Butz, F. Förster-Zügel, and H. F. Schlaak. "Switchable adhesion for wafer-handling based on dielectric elastomer stack transducers." In *Electroactive Polymer Actuators and Devices (EAPAD) 2016*, vol. 9798, p. 97983B. International Society for Optics and Photonics, 2016.
- [92] Hau, Steffen, Daniel Bruch, Gianluca Rizzello, Paul Motzki, and Stefan Seelecke. "Silicone based dielectric elastomer strip actuators coupled with nonlinear biasing elements for large actuation strains." *Smart Materials and Structures* 27, no. 7 (2018): 074003.
- [93] Hau, Steffen, Alexander York, Gianluca Rizzello, and Stefan Seelecke. "Performance

- prediction and scaling laws of circular dielectric elastomer membrane actuators." *Journal of Mechanical Design* 140, no. 11 (2018).
- [94] Grewe, Benjamin F., Fabian F. Voigt, Marcel van't Hoff, and Fritjof Helmchen. "Fast two-layer two-photon imaging of neuronal cell populations using an electrically tunable lens." *Biomedical optics express* 2, no. 7 (2011): 2035-2046.
- [95] Poulin, Alexandre, Cansaran Saygili Demir, Samuel Rosset, Tatiana V. Petrova, and Herbert Shea. "Dielectric elastomer actuator for mechanical loading of 2D cell cultures." *Lab on a Chip* 16, no. 19 (2016): 3788-3794.
- [96] Heydt, Richard, Roy Kornbluh, Joseph Eckerle, and Ron Pelrine. "Sound radiation properties of dielectric elastomer electroactive polymer loudspeakers." In *Smart structures and materials 2006: Electroactive polymer actuators and devices (eapad)*, vol. 6168, p. 61681M. International Society for Optics and Photonics, 2006.
- [97] Lotz, Peter, Marc Matysek, and Helmut F. Schlaak. "Fabrication and application of miniaturized dielectric elastomer stack actuators." *IEEE/ASME Transactions on mechatronics* 16, no. 1 (2010): 58-66.
- [98] Gao, Xing, Chongjing Cao, Jianglong Guo, and Andrew Conn. "Elastic electroadhesion with rapid release by integrated resonant vibration." *Advanced Materials Technologies* 4, no. 1 (2019): 1800378.
- [99] Poulin, Alexandre, Samuel Rosset, and Herbert R. Shea. "Printing low-voltage dielectric elastomer actuators." *Applied Physics Letters* 107, no. 24 (2015): 244104.
- [100] Töpfer, Tino, Bekim Osmani, Samuel Lörcher, and Bert Müller. "Leakage current, self-clearing and actuation efficiency of nanometer-thin, low-voltage dielectric elastomer transducers tailored by thermal evaporation." In *Electroactive Polymer Actuators and Devices (EAPAD) 2017*, vol. 10163, p. 101631F. International Society for Optics and Photonics, 2017.
- [101] Kim, Sanha, Yijie Jiang, Kiera L. Thompson Towell, Michael SH Boutilier, Nigamaa Nayakanti, Changhong Cao, Chunxu Chen et al. "Soft nanocomposite electroadhesives

- for digital micro-and nanotransfer printing." *Science advances* 5, no. 10 (2019): eaax4790.
- [102] Monkman, Gareth J. "Robot grippers for use with fibrous materials." *The International journal of robotics research* 14, no. 2 (1995): 144-151.
- [103] Prahlad, Harsha E., Ronald E. Pelrine, Philip A. Von Guggenberg, Roy D. Kornbluh, and Joseph S. Eckerle. "High voltage converters for electrostatic applications." U.S. Patent Application 13/356,300, filed July 25, 2013.
- [104] Grotepaß, T., J. Butz, F. Förster-Zügel, and H. F. Schlaak. "Switchable adhesion for wafer-handling based on dielectric elastomer stack transducers." In *Electroactive Polymer Actuators and Devices (EAPAD) 2016*, vol. 9798, p. 97983B. International Society for Optics and Photonics, 2016.
- [105] Hollis, R. L., J. Gowdy, and A. A. Rizzi. "Design and development of a tabletop precision assembly system." *Mechatronics and Robotics, (MechRob'04) Aachen, Germany* (2004): 1619-1623.
- [106] Zhou, Ming, Yu Tian, Dan Sameoto, Xiangjun Zhang, Yonggang Meng, and Shizhu Wen. "Controllable interfacial adhesion applied to transfer light and fragile objects by using gecko inspired mushroom-shaped pillar surface." *ACS applied materials & interfaces* 5, no. 20 (2013): 10137-10144.
- [107] Jeong, Hoon Eui, Jin-Kwan Lee, Hong Nam Kim, Sang Heup Moon, and Kahp Y. Suh. "A nontransferring dry adhesive with hierarchical polymer nanohairs." *Proceedings of the National Academy of Sciences* 106, no. 14 (2009): 5639-5644.
- [108] Purto, Julia, Mareike Frensemeier, and Elmar Kroner. "Switchable adhesion in vacuum using bio-inspired dry adhesives." *ACS applied materials & interfaces* 7, no. 43 (2015): 24127-24135.
- [109] Song, Sukho, Dirk-Michael Drotlef, Carmel Majidi, and Metin Sitti. "Controllable load sharing for soft adhesive interfaces on three-dimensional surfaces." *Proceedings of the National Academy of Sciences* 114, no. 22 (2017): E4344-E4353.

- [110] Hensel, René, Karsten Moh, and Eduard Arzt. "Engineering micropatterned dry adhesives: from contact theory to handling applications." *Advanced Functional Materials* 28, no. 28 (2018): 1800865.
- [111] Booth, Jamie A., Verena Tinnemann, René Hensel, Eduard Arzt, Robert M. McMeeking, and Kimberly L. Foster. "Statistical properties of defect-dependent detachment strength in bioinspired dry adhesives." *Journal of the Royal Society Interface* 16, no. 156 (2019): 20190239.
- [112] Tinnemann, Verena, Luissé Hernández, Sarah CL Fischer, Eduard Arzt, Roland Bennewitz, and René Hensel. "In situ observation reveals local detachment mechanisms and suction effects in micropatterned adhesives." *Advanced Functional Materials* 29, no. 14 (2019): 1807713.
- [113] Paretkar, Dadhichi, Marleen Kamperman, Andreas S. Schneider, David Martina, Costantino Creton, and Eduard Arzt. "Bioinspired pressure actuated adhesive system." *Materials Science and Engineering: C* 31, no. 6 (2011): 1152-1159.
- [114] Tinnemann, Verena, Eduard Arzt, and René Hensel. "Switchable double-sided micropatterned adhesives for selective fixation and detachment." *Journal of the Mechanics and Physics of Solids* 123 (2019): 20-27.
- [115] Frensemeier, Mareike, Jessica S. Kaiser, Carl P. Frick, Andreas S. Schneider, Eduard Arzt, Ray S. Fertig III, and Elmar Kroner. "Temperature-Induced Switchable Adhesion using Nickel–Titanium–Polydimethylsiloxane Hybrid Surfaces." *Advanced Functional Materials* 25, no. 20 (2015): 3013-3021.
- [116] Reddy, Shravanthi, Eduard Arzt, and Aranzazu del Campo. "Bioinspired surfaces with switchable adhesion." *Advanced materials* 19, no. 22 (2007): 3833-3837.
- [117] Krahn, Jeffrey, Enrico Bovero, and Carlo Menon. "Magnetic field switchable dry adhesives." *ACS applied materials & interfaces* 7, no. 4 (2015): 2214-2222.
- [118] Drotlef, Dirk-Michael, Peter Blümler, and Aranzazu del Campo. "Magnetically actuated patterns for bioinspired reversible adhesion (dry and wet)." *Advanced Materials* 26, no.

- 5 (2014): 775-779.
- [119] Nadermann, Nichole, Jing Ning, Anand Jagota, and C-Y. Hui. "Active switching of adhesion in a film-terminated fibrillar structure." *Langmuir* 26, no. 19 (2010): 15464-15471.
- [120] Shintake, Jun, Samuel Rosset, Bryan Schubert, Dario Floreano, and Herbert Shea. "Versatile soft grippers with intrinsic electroadhesion based on multifunctional polymer actuators." *Advanced Materials* 28, no. 2 (2016): 231-238.
- [121] Guo, Jianglong, Thomas Bamber, Matthew Chamberlain, Laura Justham, and Michael Jackson. "Optimization and experimental verification of coplanar interdigital electroadhesives." *Journal of Physics D: Applied Physics* 49, no. 41 (2016): 415304.
- [122] Persson, Bo NJ, and Jianglong Guo. "Electroadhesion for soft adhesive pads and robotics: theory and numerical results." *Soft matter* 15, no. 40 (2019): 8032-8039.
- [123] Asano, Kazutoshi, Fumikazu Hatakeyama, and Kyoko Yatsuzuka. "Fundamental study of an electrostatic chuck for silicon wafer handling." *IEEE Transactions on Industry Applications* 38, no. 3 (2002): 840-845.
- [124] Monkman, Gareth. "Electroadhesive microgrippers." *Industrial Robot: An International Journal* (2003).
- [125] Cao, Changyong, Xiaoyu Sun, Yuhui Fang, Qing-Hua Qin, Aibing Yu, and Xi-Qiao Feng. "Theoretical model and design of electroadhesive pad with interdigitated electrodes." *Materials & Design* 89 (2016): 485-491.
- [126] Shintake, Jun, Vito Cacucciolo, Dario Floreano, and Herbert Shea. "Soft robotic grippers." *Advanced Materials* 30, no. 29 (2018): 1707035.
- [127] Ruffatto III, Donald, Aaron Parness, and Matthew Spenko. "Improving controllable adhesion on both rough and smooth surfaces with a hybrid electrostatic/gecko-like adhesive." *Journal of The Royal Society Interface* 11, no. 93 (2014): 20131089.
- [128] Schargott, M., V. L. Popov, and S. Gorb. "Spring model of biological attachment

- pads." *Journal of theoretical biology* 243, no. 1 (2006): 48-53.
- [129] Zambakas, J. D., D. A. Retalis, and D. Ch Mavrakis. "A simultaneous interpretation, by wind speed and direction, of ambient air polar conductivities in Athens, Greece." *Archives for meteorology, geophysics, and bioclimatology, Series A* 33, no. 4 (1985): 381-388.
- [130] Smith, L. G., and G. F. Schilling. "The variation of electrical conductivity of air within sealed rooms." *Journal of Atmospheric and Terrestrial Physics* 4, no. 6 (1954): 314-321.
- [131] J. Mark, *Polymer Data Handbook*, 2nd ed. New York, New York, USA: Oxford University Press, 2009.
- [132] G. W. Morey, "The Property of Glass," *Am. Chem. Soc., Monogr. Ser. Reinhold, Publ. Corp.*, 1954.
- [133] Warburg, Emil, and T. Ihmori. "Ueber das Gewicht und die Ursache der Wasserhaut bei Glas und anderen Körpern." *Annalen der Physik* 263, no. 4 (1886): 481-507.
- [134] Awakuni, Y., and J. H. Calderwood. "Water vapour adsorption and surface conductivity in solids." *Journal of Physics D: Applied Physics* 5, no. 5 (1972): 1038.
- [135] Skinner, Brian, M. S. Loth, and B. I. Shklovskii. "Ionic conductivity on a wetting surface." *Physical Review E* 80, no. 4 (2009): 041925.
- [136] H. L. Curtis, "Insulating properties of solid dielectrics," *Bull. Bur. Stand.*, vol. 11, no. 3, p. 359, 1915
- [137] H. H. Woodson and J. R. Melcher, *Electromechanical dynamics*. Wiley, 1968.
- [138] Arnoldus, Henk F. "Conservation of charge at an interface." *Optics communications* 265, no. 1 (2006): 52-59.
- [139] Castellanos, A., and A. Gonzalez. "Nonlinear electrohydrodynamics of free surfaces." *IEEE Transactions on Dielectrics and Electrical Insulation* 5, no. 3 (1998): 334-343.

- [140] Carlon, Hugh R. *Electrical properties of atmospheric moist air: A systematic, experimental study*. No. CRDEC-TR-88059. CHEMICAL RESEARCH DEVELOPMENT AND ENGINEERING CENTER ABERDEEN PROVING GROUND MD, 1988.
- [141] Cobb, William E., and Howard J. Wells. "The electrical conductivity of oceanic air and its correlation to global atmospheric pollution." *Journal of the Atmospheric Sciences* 27, no. 5 (1970): 814-819.
- [142] Sampath, S., V. Sasi Kumar, and S. Murali Das. "Airborne measurements of atmospheric electrical conductivities." *pure and applied geophysics* 143, no. 4 (1994): 713-727.
- [143] A. Van Hippel, "Tables of Dielectric Materials.," MIT Cambridge, Laboratory for Insulation Research, 1944.
- [144] Deyhimi, F., and J-L. Munoz. "Surface resistivity of different silylated glasses." *Journal of applied electrochemistry* 14, no. 6 (1984): 803-806.
- [145] Paiva, Victor TC, Leandra P. Santos, Douglas S. da Silva, Thiago AL Burgo, and Fernando Galembeck. "Conduction and Excess Charge in Silicate Glass/Air Interfaces." *Langmuir* 35, no. 24 (2019): 7703-7712.
- [146] J. Mark, "Polymer Data Handbook, 2nd ed. Polymer Data Handbook, 2nd ed .," *J. Am. Chem. Soc.*, vol. 131, no. 44, pp. 16330–16330, 2009
- [147] Moulson, Anthony J., and John M. Herbert. *Electroceramics: materials, properties, applications*. John Wiley & Sons, 2003.
- [148] J. F. Shackelford, Y.-H. Han, S. Kim, and S.-H. Kwon, *CRC Materials Science and Engineering Handbook*. 2016.
- [149] D. Marcuse, "Electrostatic Field of Coplanar Lines Computed with the Point Matching Method," *IEEE J. quantum Electron.* 25(5), 939-947., 1989
- [150] Xu, Liang, Hao Wu, Guo Yao, Libo Chen, Xiaodan Yang, Baodong Chen, Xin Huang

- et al. "Giant voltage enhancement via triboelectric charge supplement channel for self-powered electroadhesion." *ACS nano* 12, no. 10 (2018): 10262-10271.
- [151] Guo, Jianglong, Mitul Tailor, Thomas Bamber, Matthew Chamberlain, Laura Justham, and Michael Jackson. "Investigation of relationship between interfacial electroadhesive force and surface texture." *Journal of Physics D: Applied Physics* 49, no. 3 (2015): 035303.
- [152] R. P. Krape, "Applications study of electroadhesive devices," National Aeronautics and Space Administration, NASA Contractor Report, CR-1211, 1968.
- [153] Kroner, Elmar, Roya Maboudian, and Eduard Arzt. "Adhesion characteristics of PDMS surfaces during repeated pull-off force measurements." *Advanced Engineering Materials* 12, no. 5 (2010): 398-404.
- [154] Micciché, Maurizio, Eduard Arzt, and Elmar Kroner. "Single macroscopic pillars as model system for bioinspired adhesives: influence of tip dimension, aspect ratio, and tilt angle." *ACS applied materials & interfaces* 6, no. 10 (2014): 7076-7083.
- [155] Fischer, Sarah CL, Katja Groß, Oscar Torrents Abad, Michael M. Becker, Euiyoung Park, René Hensel, and Eduard Arzt. "Funnel-Shaped Microstructures for Strong Reversible Adhesion." *Advanced Materials Interfaces* 4, no. 20 (2017): 1700292.
- [156] Song, Sukho, Dirk-Michael Drotlef, Carmel Majidi, and Metin Sitti. "Controllable load sharing for soft adhesive interfaces on three-dimensional surfaces." *Proceedings of the National Academy of Sciences* 114, no. 22 (2017): E4344-E4353.
- [157] Hossfeld, Craig K., Andreas S. Schneider, Eduard Arzt, and Carl P. Frick. "Detachment behavior of mushroom-shaped fibrillar adhesive surfaces in peel testing." *Langmuir* 29, no. 49 (2013): 15394-15404.
- [158] Tinnemann, Verena, Luissé Hernández, Sarah CL Fischer, Eduard Arzt, Roland Bennowitz, and René Hensel. "In situ observation reveals local detachment mechanisms and suction effects in micropatterned adhesives." *Advanced Functional Materials* 29, no. 14 (2019): 1807713.

- [159] Huang, Jiangshui, Tongqing Lu, Jian Zhu, David R. Clarke, and Zhigang Suo. "Large, uni-directional actuation in dielectric elastomers achieved by fiber stiffening." *Applied physics letters* 100, no. 21 (2012): 211901.
- [160] Shian, Samuel, Katia Bertoldi, and David R. Clarke. "Dielectric elastomer based "grippers" for soft robotics." *Advanced Materials* 27, no. 43 (2015): 6814-6819.
- [161] Biggs, S. James, and Roger N. Hitchcock. "Artificial muscle actuators for haptic displays: system design to match the dynamics and tactile sensitivity of the human fingerpad." In *Electroactive Polymer Actuators and Devices (EAPAD) 2010*, vol. 7642, p. 76420I. International Society for Optics and Photonics, 2010.
- [162] Johnson, Kenneth Langstreth, Kevin Kendall, and AD Roberts. "Surface energy and the contact of elastic solids." *Proceedings of the royal society of London. A. mathematical and physical sciences* 324, no. 1558 (1971): 301-313.
- [163] Tabor, D. "Surface forces and surface interactions." In *Plenary and invited lectures*, pp. 3-14. Academic Press, 1977.
- [164] D. Maugis, *Contact, adhesion and rupture of elastic solids. In Solid state science.* p-234, Springer US, 1999.
- [165] Hui, C-Y., N. J. Glassmaker, and A. Jagota. "How compliance compensates for surface roughness in fibrillar adhesion." *The Journal of Adhesion* 81, no. 7-8 (2005): 699-721.
- [166] Dorogin, Leonid, A. Tiwari, C. Rotella, P. Mangiagalli, and B. N. J. Persson. "Role of preload in adhesion of rough surfaces." *Physical review letters* 118, no. 23 (2017): 238001.
- [167] Bacca, Mattia, Jamie A. Booth, Kimberly L. Turner, and Robert M. McMeeking. "Load sharing in bioinspired fibrillar adhesives with backing layer interactions and interfacial misalignment." *Journal of the Mechanics and Physics of Solids* 96 (2016): 428-444.
- [168] Khaderi, S. N., N. A. Fleck, E. Arzt, and R. M. McMeeking. "Detachment of an adhered micropillar from a dissimilar substrate." *Journal of the Mechanics and Physics of Solids* 75 (2015): 159-183.

- [169] Balijepalli, R. G., M. R. Begley, N. A. Fleck, R. M. McMeeking, and E. Arzt. "Numerical simulation of the edge stress singularity and the adhesion strength for compliant mushroom fibrils adhered to rigid substrates." *International Journal of Solids and Structures* 85 (2016): 160-171.
- [170] Lorenz, B., B. A. Krick, N. Mulakaluri, M. Smolyakova, S. Dieluweit, W. G. Sawyer, and B. N. J. Persson. "Adhesion: role of bulk viscoelasticity and surface roughness." *Journal of Physics: Condensed Matter* 25, no. 22 (2013): 225004.
- [171] Tiwari, A., L. Dorogin, A. I. Bennett, K. D. Schulze, W. G. Sawyer, M. Tahir, G. Heinrich, and B. N. J. Persson. "The effect of surface roughness and viscoelasticity on rubber adhesion." *Soft matter* 13, no. 19 (2017): 3602-3621.
- [172] Loew, Philipp, Gianluca Rizzello, Filomena Simone, and Stefan Seelecke. "Finite element simulation of plane strain dielectric elastomer membranes actuated by discretized electrodes." In *Electroactive Polymer Actuators and Devices (EAPAD) XXI*, vol. 10966, p. 109660W. International Society for Optics and Photonics, 2019.
- [173] Tran, Danh Quang, Jin Li, Fuzhen Xuan, and Ting Xiao. "Viscoelastic effects on the actuation performance of a dielectric elastomer actuator under different equal, un-equal biaxial pre-stretches." *Materials Research Express* 5, no. 6 (2018): 065303.
- [174] Paretkar, Dadhichi, Marleen Kamperman, David Martina, Jiahua Zhao, Costantino Creton, Anke Lindner, Anand Jagota, Robert McMeeking, and Eduard Arzt. "Preload-responsive adhesion: effects of aspect ratio, tip shape and alignment." *Journal of the Royal Society Interface* 10, no. 83 (2013): 20130171.
- [175] Kim, Seok, Metin Sitti, Chung-Yuen Hui, Rong Long, and Anand Jagota. "Effect of backing layer thickness on adhesion of single-level elastomer fiber arrays." *Applied Physics Letters* 91, no. 16 (2007): 161905.
- [176] Fischer, Sarah CL, Eduard Arzt, and René Hensel. "Composite pillars with a tunable interface for adhesion to rough substrates." *ACS applied materials & interfaces* 9, no. 1 (2017): 1036-1044.

- [177] "Bioinspirierte Haftstrukturen für Robotik und Industrie 4.0.," 2019.
- [178] Yu, Dan, Dirk Beckelmann, Michael Opsölder, Bruno Schäfer, Karsten Moh, René Hensel, Peter William De Oliveira, and Eduard Arzt. "Roll-to-roll manufacturing of micropatterned adhesives by template compression." *Materials* 12, no. 1 (2019): 97.
- [179] Araromi, Oluwaseun A., Samuel Rosset, and Herbert R. Shea. "High-resolution, large-area fabrication of compliant electrodes via laser ablation for robust, stretchable dielectric elastomer actuators and sensors." *ACS applied materials & interfaces* 7, no. 32 (2015): 18046-18053.
- [180] Biggs, S. James, and Roger N. Hitchcock. "Artificial muscle actuators for haptic displays: system design to match the dynamics and tactile sensitivity of the human fingerpad." In *Electroactive Polymer Actuators and Devices (EAPAD) 2010*, vol. 7642, p. 76420I. International Society for Optics and Photonics, 2010.
- [181] Alizadehyazdi, Vahid, Aiva Simaite, and Matthew Spenko. "Evaluation of Material Properties for Practical Microstructured Adhesives: Low Dust Adhesion and High Shear Strength." *ACS applied materials & interfaces* 11, no. 8 (2019): 8654-8666.

Curriculum Vitae

Vaishali Chopra

Weinbrennerstrasse 7, Saarbrücken, 66123, Germany

Vaishalic51@gmail.com, 0049-17669592236

Education

Amity University- Uttar Pradesh, India

(2007- 2013)

Integrated Master of Technology, M. Tech in Nanotechnology

- **GPA** 9.3/10
- **Relevant coursework:** Basics of VLSI Processing, Chemistry and Characterization of Surface and Thin films
- **Master Thesis:** Band gap tailored covellite CuS for blue emission at the **Materials Research Centre (MRC), Indian Institute of Science, India**

Academic Experiences

Functional Microstructures Group

INM, Leibniz Institute for New Materials, Saarbrücken, Germany

Marie Curie Early Stage Researcher (**ITN BiosmartTrainee**) **(May 2016- July 2020)**

- Attachment and detachment processes are critical to the pick and place applications for microhandling applications in Industry. Thesis aims at studying the synergistic effect of electrostatic forces in modulating the adhesion in bio-inspired micropatterned adhesives. Concepts of **Electroadhesion** and **Dielectric elastomeric actuators** were explored. **2-photon lithography** was used to fabricate microstructures with the Nanoscribe GmbH GT1 system.
- **Thesis title:** Adhesion Modulation in Bio-inspired Micropatterned Adhesives by Electrical fields.

Electrochemical Laboratory

Interuniversity Microelectronics Centre (Imec), Kapeldreef, Belgium

Post graduate Researcher

(July 2014-September 2015)

- Explored Sn electrochemistry for 3D stacking of Integrated circuits. Deposition parameters were optimized by characterizing the film morphology of galvanostatically deposited Sn films using Scanning Electron microscopy (SEM).

Optics, Nanostructures and Quantum Fluids Laboratory

Centre for Nano Science and Engineering (CeNSE), Indian Institute of Science

IISc, Bangalore, India

Project associate

(July 2013- April 2014)

- Micro and Nanoscale magnetic structures fabricated using Glancing angle deposition system were studied in homogenous magnetic fields. Independent positioning of these nano-propellers was demonstrated, and the results were published in peer-reviewed journal.

Materials Research Centre

Indian Institute of Science (IISc), Bangalore, India

Project associate

(Aug 2012- June 2013)

- Stoichiometric ratios of precursors Cu and S were tailored in a solvothermal wet bench process to tune the band gap of Copper Sulphide particles. Photoluminescence measurements were carried out to characterize the band gap of the particles. SEM and XRD measurements were used for characterising the topography and crystal structure.

Internships and Fellowships

Facebook Reality Labs, FRL, Ireland

Facebook

Research Intern**(Sept 2018- Nov 2018)**

- Planning and delivery of 3 high impact projects utilizing but not limited to 2-photon lithography. Coordinated between teams in US and Ireland. Feasibility studies kickstarted new pilot projects and positively demonstrated key role of this technique in the main production line.

Department of Applied Physics**TU Eindhoven, Netherlands****Research Intern****(Feb 2018)**

- Research focused on designing micropatterned surfaces using 2-photon lithography technique and studying the dewetting behaviour on these micropatterned surfaces. Results have been published in a peer-review journal.

Semiconductor Laser Section**Raja Ramanna Centre for Advanced Technology, Indore, India****Young Scientist Research Fellow****(May 2011- July 2011)**

- High resolution X-ray diffraction (HRXRD) was used for comparative analysis of prefabricated GaN/sapphire epitaxial layers deposited via HVPE and MOVPE techniques. Dislocation density validated MOVPE grown layers better candidates for device improvement.
- Thesis title: HRXRD Characterization of Nitride Epitaxial Layers

Department of Physics and Astrophysics**Delhi University, Delhi, India****Research Intern****(June 2010- Aug 2010)**

- Zinc Oxide (ZnO) films have biosensing properties. Project involved deposition of ZnO thin films using RF Magnetron system. Cyclic voltammetry studies on these films were carried out for glucose bio sensing applications.

- Thesis title: Studies on sputtered ZnO thin films for biosensing applications.

Electronics Materials Division

National Physical Laboratory (NPL), Delhi, India

Research Intern

(June 2010- Aug 2010)

- Gained hands-on-experience on the Plasma Enhanced Chemical vapor deposition system (**PECVD**) for deposition of silica films on silicon wafers for optical applications. Thesis summarized significant aspects of material processing and vacuum technology.
- Thesis title: Studies on Material Processing

Academic achievements and Scholarships

- Awarded the **Best Poster award** at the 15th European Conference on Organised films (**ECOF**), Dresden, Germany by Langmuir for the poster titled Electrically tuned bioinspired adhesion. July 2017
- Awarded **Marie Curie Fellowship** in the EU Horizon 2020 Biosmart Trainee network and hosted at the Leibniz, Institute for New Materials (INM), Saarbrücken as an Early Stage Researcher. May 2016-September 2019
- Awarded **Silver medal** for ranking in the top 4 % of the batch in Integrated M.Tech in Nanotechnology at AINT, Amity University India, Batch 2007-2013
- Awarded Merit scholarship for the academic session (2007-08 and 2011-12) at AINT
- Selected as the Young Scientist Researcher at the Raja Ramanna Center for Advanced Studies (RRCAT) Indore, India (Department of Atomic Energy, Govt. Of India) 2011

English Proficiency tests

- **Toefl iBT (2012) – 107/120** – (Reading-24, Listening-27, Speaking-28 and Writing-28)
- **GRE (2012)- 312/340-** (Quantitative Reasoning- 162/170, Verbal reasoning- 150/170 and Analytical writing analysis AWA- 3.5/6)

Software skills

- Autodesk CAD, Inventor, Solidworks
- Matlab and Origin

Languages

- Hindi (Native), English (Fluent), Punjabi (Beginners) and German (A2)

Publications

1. Chudak, Maciej, Vaishali Chopra, René Hensel, and Anton A. Darhuber. **"Elastohydrodynamic Dewetting of Thin Liquid Films: Elucidating Underwater Adhesion of Topographically Patterned Surfaces."** *Langmuir* 36, no. 40 (2020): 11929-11937.
2. Chopra, Vaishali, Maciej Chudak, René Hensel, Anton A. Darhuber, and Eduard Arzt. "Enhancing dry adhesion of polymeric micropatterns by electric fields." *ACS Applied Materials & Interfaces* (2020).
3. Mandal, Pranay, Vaishali Chopra, and Ambarish Ghosh. "Independent positioning of magnetic nanomotors." *ACS nano* 9, no. 5 (2015): 4717-4725.

Hobbies

Reading Science fiction and Junior Classical Vocal Music

